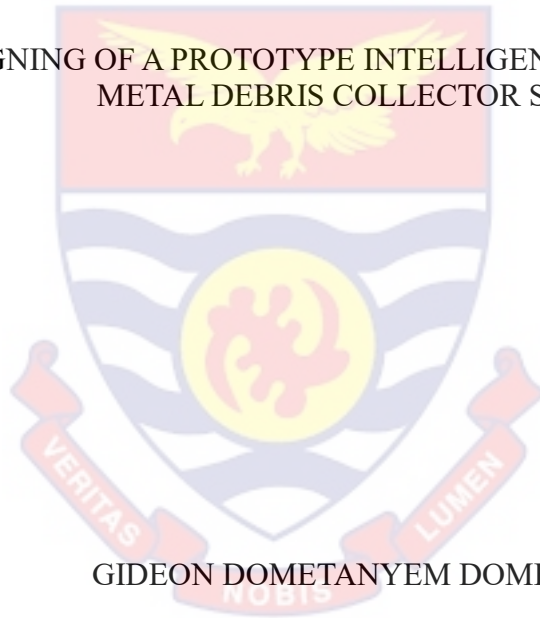


UNIVERSITY OF CAPE COAST

DESIGNING OF A PROTOTYPE INTELLIGENT ARDUINO-BASED
METAL DEBRIS COLLECTOR SYSTEM



GIDEON DOMETANYEM DOMEGBEER

2024



© Gideon Dometanyem Domegbebr
University of Cape Coast

UNIVERSITY OF CAPE COAST

DESIGNING OF A PROTOTYPE INTELLIGENT ARDUINO-BASED METAL
DEBRIS COLLECTOR SYSTEM

BY

GIDEON DOMETANYEM DOMEGBEBR

Thesis submitted to the Department of Physics of the School of Physical Sciences,
College of Agriculture and Natural Sciences, University of Cape Coast, in partial
fulfilment of the requirements for the award of Master of Philosophy degree in
Physics

APRIL 2024

DECLARATION

Candidate's Declaration

I hereby declare that this thesis is the result of my own original research and that no part of it has been presented for another degree in this university or elsewhere.

Candidate's Signature Date:

Name: Gideon Domegbebr Dometanyem

Supervisor's Declaration

I hereby declare that the preparation and presentation of the thesis were supervised in accordance with the guidelines on supervision of thesis laid down by the University of Cape Coast.

Supervisor's Signature Date:

Name: Prof. Kwadwo Anokye Dompseh

ABSTRACT

This thesis presents a proof-of-concept of the designing of a prototype of an Intelligent Arduino-Based Metal Debris Collector System (InAMDeCS). The InAMDeCS is made up of the following: a metal detector system, a microcontroller and an electromagnet, as well as an audio system. The prototype employs the principle of Noncontact Active Debris Removal Techniques (NADRT) which encompasses real-time detection of metal debris (MD) using the pulse induction metal detection principle and electromagnetic attraction. A microcontroller coordinates the activities of the metal detection and a subsequent actuation of the electromagnet to remove the MD. The simulations of the metal detection system and the electromagnet's specifications were performed in a laboratory setting. A change in inductance as a result of MD acting as core for an air-cored coil was observed as a change in tone of the audio system and read as a voltage change in an Arduino Integrated Development Environment. The data obtained was used in training the controller. The electromagnet could attract a six-inch nail at an average distance of 5 cm when a direct current voltage of 6 V to 12 V flows through it. It works by broadcasting a pulsating magnetic field, receiving a returned field and analysing it to ascertain the presence of MD by determining a change in the time constant of an inductor-capacitor oscillator. It can be used as attachment to vehicles used in cleaning roads or it can be developed into an automobile for road maintenance services. The results confirmed the applicability of the prototype in detecting and removing MD from roads and other work site.

KEY WORDS

Accidents

Arduino

Debris

Detectors

Electromagnet

Inductance

ACKNOWLEDGEMENT

I would like to express my sincere gratitude to my supervisor, Prof. Kwadwo Anokye Dompoh, for his invaluable guidance, support, and encouragement throughout the entire research process. His expertise and insights greatly contributed to the success of this thesis. I extend my appreciation to the faculty and staff of the University of Cape Coast for creating a conducive academic environment. The resources and facilities provided were essential to the successful completion of this thesis.

I extend my appreciation to all the lecturers and staff of the Department of Physics, especially, Prof. Moses Jojo Eghan, Emeritus Prof. Paul Kingsley Buah-Bassuah, Prof. George Amoako, Prof. Raymond Edziah, Prof. Benjamin Anderson, Prof. Frederick Sam, Mr. Patrick Mensah-Amoah, and the remaining lecturers whose expertise and encouragement have been instrumental in shaping this work.

I am also thankful to my colleagues and friends who provided assistance and shared their knowledge, making this journey a collaborative and enriching experience. Special thanks to my family for their unwavering support and understanding during the ups and downs of the research journey. Your love and your encouragement were my driving force.

DEDICATION

To my parents and my siblings

TABLE OF CONTENTS

	Page
DECLARATION	ii
ABSTRACT	iii
KEY WORDS	iv
ACKNOWLEDGEMENT	v
DEDICATION	vi
LIST OF TABLES	xi
LIST OF FIGURES	xii
LIST OF ABBREVIATIONS	xvii
CHAPTER ONE: INTRODUCTION	
Background to the Study	1
Statement of the Problem	4
Aim and Objectives of the Study	5
Research Questions	6
Significance of the Study	6
Delimitation	7
Limitations	8
The Organisation of the Study	9
CHAPTER TWO: LITERATURE REVIEW	
Introduction	10
Road Traffic Accidents	10
Causes of RTA: The Tyre and Debris as Factors	10

Road Debris Identification and Removal	13
Metal Detection Systems	23
Chapter Summary	25
CHAPTER THREE: METHODOLOGY	
Introduction	26
Research Design	26
Metal Detector Design Methodology	28
Electromagnet Design Methodology	35
The Design Methodology of the Microcontroller	40
Prototyping of InAMDeCS parts.	42
Chapter Summary	44
CHAPTER FOUR: RESULTS AND DISCUSSION	
Introduction	45
Results of the Experimental Verification of the Inductance Equation	46
Results of the Analysis of the Variation of Inductance with Number of Turns (N) and Radius of Coil (R)	46
Results of the Design and Functional Testing and Validation of the Metal Detection System	50
Results of the Design and Functional Testing and Validation of the Electromagnet (Experiment 3)	51
Results and Discussion on the Functional Prototyped InAMDeCS	54
Chapter Summary	56

CHAPTER FIVE: SUMMARY, CONCLUSIONS AND
RECOMMENDATIONS

Overview	57
Summary	57
Conclusions	58
Recommendations	59
REFERENCES	61
APPENDICES	
APPENDIX A: GENERAL THEORETICAL FORMULATION OF ELECTROMAGNETICS	88
APPENDIX B: MAGNETIC FIELD OF CURRENT ELEMENTS	100
APPENDIX C: MAGNETIC FIELDS OF COILS	103
APPENDIX D: MAGNETIC FIELDS OF SOLENOIDS	106
APPENDIX E: EXPERIMENT 1	108
APPENDIX F: ANALYSIS OF THE VARIATION OF INDUCTANCE WITH NUMBER OF TURNS AND RADIUS OF COIL IN MATLAB	114
APPENDIX G: MAGNETIC SPECIFICATIONS OF S1 AND S2	116
APPENDIX H: EXPERIMENT 3	118
APPENDIX I: MDet CODE	122
APPENDIX J: PROCEDURE FOR BURNING THE BOOTLOADER ON THE MICROCONTROLLER	123
APPENDIX K: DESCRIPTION OF COMPONENTS	127

APPENDIX L: WIRE SPECIFICATIONS FOR ELECTROMAGNETIC TECHNOLOGY	137
APPENDIX M: EXPENDITURE ON THE COMPONENTS	138

LIST OF TABLES

		Page
1	Mechanical Fault Constituting RTAs	12
2	The Design Parameters of the Solenoids S_1 and S_2	40
3	Optoelectronic Components used in Constructing the Arduino Board	41
4	Power Line Mapping for InAMDeCS Power System	44
5	Summary of the Relay Connections Mapping	44
6	Parameters of the Coils used for the Analysis of the Variation of Inductance with Radius and Number of Turns	47
7	Distances at which the 81 g Mass was Attracted by the Electromagnets	52
8	Distances at which the 87 g Mass was Attracted by the Electromagnets	52

LIST OF FIGURES

		Page
1	Pictures of Manual Methods of Street Cleaning Mostly Used in the LMIC	15
2	Pictures of Some Sweeper Tricycle with Mechanical Broom	16
3	Pictures of Some State-Of-The-Art Road/Street Sweeping Machines	17
4	Picture of the Eriez Magnetic Sweeper	19
5	Picture of the FALCON MS Magnetic Sweeper	20
6	Design Block Diagram of the PI Metal Detector System	28
7	PI Metal Detector Working Principle	29
8	RLC Circuit for Demonstrating Magnetic Oscillation	32
9	Pulse Induction Metal Detector Drive Circuit	34
10	Picture of the Experimental Setup used to Test the Functionality of the Designed MDet	34
11	Picture of the Assembled Arduino Component on a Breadboard as a Guide for Building an Arduino Board	40
12	Flow Charts of the Conceptuality of the Function of InAMDeCS	42
13	Graphs of Inductance (L) Against Radius of Coil (R)	47
14	Graphs of Inductance (L) Against Number of Turns of Coil (N)	48
15	Three-dimensional graphs of inductance (L) against radius of coil (R) and number of turns of coil (N)	49

16	Pictures Showing the Positions of Masses M1 and M2 for the Open and Close Magnetic Circuits	51
17	A Graph of Attraction Distance for Electromagnets S1 and S2 Against MMF	53
18	A Picture Showing the Functional Parts of the Prototyped InAMDeCS	54

LIST OF PHYSICAL CONSTANTS

NAME OF QUANTITY	SYMBOL	VALUE
Electric permittivity of free space	ϵ_0	$8.85 \times 10^{-12} \frac{C}{Nm^2}$
Magnetic permeability of free space	μ_0	$4\pi \times 10^{-7} H / m$
Pi	π	$\frac{22}{7}$
Speed of light in vacuum	c	$3 \times 10^8 m / s$

LIST OF SYMBOLS

\vec{H}	Magnetic Field Intensity
\vec{B}	Magnetic Flux Density (Magnetic Induction)
Φ_B	Magnetic Flux (Wb)
μ	Magnetic Permeability of a Material
μ_r	Relative Magnetic Permeability of a Material
\vec{F}_L	Lorentz Force
\vec{M}	Magnetisation
$\vec{\nabla} \times$	Curl (vector differential operator)
∇	Divergence (scalar differential operator)
I	Electric Current (A)
L	Inductance (H)
N	Number or turns of wire (Coil)
R	Resistance (Ω)
FF	Fill Factor
\vec{F}_{lift}	Lifting Force (N)
\vec{F}_{MMF}	Magnetomotive force
A_{total}	Total Cross-Sectional Area (m^2)
$A_{magnetic}$	Magnetic area (m^2)
A_{eff}	Effective Cross-Sectional Area (m^2)

I_{eddy}	Eddy current
Φ_B^{eddy}	Magnetic flux of eddy current
V_L	Induced voltage
μ_0	Magnetic permeability of free space
c	Speed of light in free space
ϵ_0	Electric permittivity of free space
\vec{D}	Electric flux density (C/m ²)
\vec{J}	Displacement current
\vec{E}	Electric field intensity
ρ	Electric charge density
Q_{enc}	Electric charge enclosed
\vec{v}	Velocity of moving charge(s)
q	Electric charge
$\Phi_B^{solenoid}$	Magnetic flux of solenoid
Φ_B^{coil}	Magnetic flux of circular coil
L_{coil}	Inductance of circular coil
$L_{solenoid}$	Inductance of solenoid
R_{coil}	Radius of circular coil

LIST OF ABBREVIATIONS

InAMDeCS	Intelligent Arduino-Based Metal Debris Collector System
RTA	Road Traffic Accidents
MTTD	Motor Traffic and Transport Department
LMIC	Low- and Middle-Income Countries
MD	Metal Debris
RMS	Road Maintenance Systems
CSM	Conventional Sweeping Methods
MDDS	Metal Debris Detection System
EPS	Electromagnetic Pickup System
MI	Magnetic Induction
MS	Microcontroller System
MDet	Metal Detector
DIY	Do-It-Yourself
WHO	World Health Organisation
UN	United Nations
GNRSA	Ghana National Road Safety Authority
EMI	Electromagnetic Induction
ADR	Active Debris Removal
GPS	Global Positioning System
NADR	Noncontact Active Debris Removal
BO	Beat Oscillation
BFO	Beat Frequency Oscillation

OR	Off-Resonance
IB	Induction Balance
PI	Pulse Induction
EMF	Electromotive Force
BC	Balance Coil
TERD	True Experimental Research Design
DE	Drive Electronics
VLF	Very Low Frequency
LC	Inductor-Capacitor
LF	Lifting Force
MMF	Magnetomotive Force
FF	Fill Factor
VCC	Voltage Common Collector
GND	Ground
PCB	Printed Circuit Board
ISP	In-System Programming
ICSP	In-Circuit Serial Programming
LDE	Light Emitting Diode
AWG	American Wire Gauge
TE	Transmit Electronics
AS	Actuator System
HIC	The High-Income Countries

CHAPTER ONE

INTRODUCTION

This chapter is an introduction to the design of an Intelligent Solar Powered Arduino based Metal Debris collector System (InAMDeCS) for detecting and collecting debris on roads. The exploration of the design, functionality, and potential impact of InAMDeCS on road transport as well as in industries is described. The scope and limitations of InAMDeCS are also presented.

Background to the Study

Road Traffic Accidents (RTA) are a global tragedy with a rising trend (Deme, 2019; Owusu, 2018). In Ghana, RTAs have been a major cause for concern due to the large number of fatalities and injuries they cause (Gyimah, 2023). It is estimated that RTAs claim the lives of 1909 people on average in Ghana each year, making it the second most common cause of death after malaria (Oppong, 2012) and eight times more common than HIV/AIDS and tuberculosis (Deme, 2019).

Statistics from the Ghana Police Service's Motor Traffic and Transport Department (MTTD) highlight that 14960 traffic crashes occurred in 2022, resulting in 2,373 fatalities and 15,690 injuries (Arthur, 2024). Between January and July of 2023, 13862 cars were involved in 8137 traffic crashes, which resulted in 1272 fatalities (Wunizoya, 2023); nevertheless, 2,276 fatalities and 15,409 injuries were recorded for 2023 in approximately 14,135 traffic crashes (Arthur, 2024; Arthur, 2023). The following was also highlighted by an analysis of Street Sense Organization's yearly traffic fatality figures for the years 2018–

2020: Each year, between 22,000 and 23000 cars and 4,000 to 6,000 motorbikes were engaged in RTAs, which resulted in between 2000 and 2500 deaths and between 8,000 and 16,000 injuries (Street Sense Org, n.d.).

According to literature, there are 1.3 million deaths from RTA globally each year (Deme, 2019), and 20 to 50 million catastrophic injuries occur – the majority of which necessitate long-term care (Goniewicz, K., Goniewicz, & Pawlowski, 2016; Olajuyigbe, Ogan, Adegbyega, & Fabiyi, 2014; Singh, Sahni, Bilquees, Khan, & Haq, 2016). The World Health Organization (WHO), ranked RTA as the 11th cause of death in 2002 (Ameratunga, S., Hajar, M., & Norton, R., 2006), eighth in 2018 and a projection of it to rise to the fifth rank by 2030 (Oppong, Mate-Kole, Nyarko, & Asumeng, 2022). According to WHO figures between 2009 and 2018, the low- and middle-income countries (LAMIC) generally recorded over 90 % of RTAs despite having less than 60 % of the world's vehicle population (Naeem, Shamim, Shahzad, & Khan, 2017).

Besides the human death toll, RTAs has significant economic, social, and environmental impacts. Families are shattered, individuals sustain life-altering injuries, and communities bear the economic burden of medical costs and property damage. According to WHO, RTA places a significant economic burden on countries, consuming 1 % to 3 % of the gross national product per year (Chand, Jayesh, & Bhasi, 2021; Gyimah, 2023). It is estimated that “US\$ 518 billion is spent globally on RTA with US\$ 65 billion spent in the LMIC” (Coleman, 2014). The RTA fatalities are therefore recognized as a major challenge to national sustainable development under the United Nations (UN) Agenda 2030, with various social effects such as death, injuries, property damage, business loss, and unforeseen expenses (Blankson & Lartey, 2020).

Road crashes can be attributed to several intertwined causes. Morgan (1984) categorised the causes of RTAs into human-related factors (Deme, 2019), mechanical failure, mechanical faults, poor road handling and lack of vehicular control (Boadu, 2022) due to tyre malfunctioning. According to Boadu, tyre bursts as a result of underinflating or instant cuts from foreign objects and debris on the road cause sudden loss of control (Suyabodha, 2017) and can result in collision with other vehicles and structures on the road. Research findings by Owusu (2018) highlight that mechanical fault and environmental factors account for 2.4% and 4% respectively, human error accounting for 57% and vehicular defects including tyre burst, break failure, and broken parts, were categorised as other factors and account for 24% of the factors causing RTA.

Metal debris on roads poses a specific risk to road safety (Gibson, 2021), particularly concerning tyre damages and vehicular accidents. Running over metal fragments scattered on road surfaces can puncture tyres, damage wheel rims, and impair vehicle stability, leading to potentially catastrophic accidents (Morgan, 1984), especially at high speeds. Metal debris substantially influences tyre malfunctioning, causing crystalline defects like cracks and pores. Tyre blowouts, gradual wear, pressure loss, and associated casualties are damages caused by MD. Malfunctioning tyres may lead to reduced or loss of control and rollovers (Mousavi, Hosseinzadeh, & Golzary, 2023). Metal debris may also be propelled onto windshields, cyclists, pedestrians, and bystanders, all of which can result in accidents.

Summing up, it is evident that metal debris significantly influences road crashes, posing serious risks to road users and infrastructure integrity. The

presence of metal debris on roadways increases the likelihood of accidents, injuries, and vehicle damage. However, the role of metal in society is inevitable and the growing dependence on metal for various construction purposes increase the volume of MD production. Therefore, effective removal and management of metal debris are essential to enhance road safety and prevent potential hazards. It is imperative for road maintenance authorities and policymakers to prioritise strategies that mitigate metal debris accumulation, ensuring safer road conditions for all. The UN General Assembly in its Resolution 74/299 emphasises that road safety should not be sacrificed or traded to meet other social needs; hence, advocates for stakeholders to adopt a strategy that prioritises and implements an integrated "Safe System" approach that firmly establishes road safety as a major factor in sustainable development (Blankson & Lartey, 2020; Gyimah, 2023).

Statement of the Problem

Metal debris is a significant contributing factor of RTA. However, metals are irreplaceable resources in society. Therefore, road sweeping mechanisms should inculcate metal detection and removal. However, existing Road Maintenance Systems (RMS) in the LMIC often fall short in that regards. The Conventional Sweeping Methods (CSM) may either prove insufficient and ineffective in detection and removal of MD or not sustainable in the LMIC. Moreover, the lack of standardized protocols (Abubakar *et al.*, 2022) for metal debris management contributes to inconsistencies in mitigation efforts across different jurisdictions, undermining cohesive safety initiatives.

To safeguard road users and enhance overall road safety, concerted efforts are required to confront the persistent problem of metal debris on roads. This necessitates the development of comprehensive strategies encompassing targeted sweeping techniques, enhanced monitoring systems, and public awareness campaigns. Additionally, collaboration among relevant stakeholders (David, John, & Hussain, 2020) including government agencies, road maintenance authorities, automotive industries, and research institutions is imperative to devise innovative solutions and enact policy reforms that prioritise the removal and prevention of metal debris accumulation on roads.

Aim and Objectives of the Study

The aim of the study is to design and prototype an intelligent system capable of detecting metal debris on roads by utilising an electromagnet to effectively pick up and remove the detected debris, thereby enhancing road safety and reducing the risk of vehicular accidents caused by metal debris.

The following step-by-step objectives are to ensure that the main objective is realised:

1. Design and implement an electromagnet-based pickup system capable of effectively lifting and removing metal debris from road surfaces.
2. Design and integrate a metal debris detection system with the electromagnet pickup system for automated operation purposes.
3. Design and develop customised control algorithms to coordinate detection, identification, and pickup actions, enabling seamless functionality of the integrated system.

Research Questions

Road debris and its associated contaminants pose a significant challenge but yet under-researched. This thesis aims to address the following key questions:

1. Are the current roads sweeping practices in the LMIC effective efficient, and sustainable for removing metal debris?
2. Can the development of solar-powered magnetic road sweepers be sustainable, efficient, and effective in reducing MD accumulation on roads?

Significance of the Study

The significance of this research lies in its potential to address a critical road safety issue while promoting environmental sustainability, foster technological innovation and enhance practical applications, inform decision making, and improve the well-being of individuals and communities.

First and foremost, developing an effective system to detect and remove MD is paramount for enhancing road safety. Such a system offers a sustainable and environmentally friendly solution for debris detection and removal. By reducing reliance on non-renewable energy sources and minimizing carbon emissions, it contributes to broader environmental conservation efforts. Moreover, this approach positively impacts public health, mobility, and societal resilience.

Secondly, the integration of sensor technologies, electromagnet actuators, and microcontroller systems in a solar-powered platform represents an innovative approach to addressing road safety challenges. Advancements in

these technologies have the potential to drive further innovation in transportation infrastructure and intelligent transportation systems. The findings of the study also have practical application in real-world settings, such as on highways, urban roads, and industrial areas prone to metal debris accumulation.

Lastly, the research outcomes may inform the development of policies and regulations related to road maintenance standards, safety protocols, and environmental sustainability initiatives. Insights gained from the research can guide decision-makers in formulating evidence-based strategies to address road safety challenges associated with metal debris.

In conclusion, the implementation of the system holds the potential to significantly improve road maintenance practices and enhance transportation networks. By mitigating the impact of metal debris, it can reduce economic burdens, promote sustainable economic development, and enhance the overall well-being and quality of life of communities.

Delimitation

The project focuses on proof-of-concept demonstrations, including the design and prototyping of key components such as the Metal Debris Detection System (MDDS), Electromagnet Pickup System (EPS), and control algorithm. The MDDS explores sensor technologies like magnetic induction metal (MI) detectors to identify metal fragments on surfaces. The EPS will be designed to attract detected metal debris using control algorithms for precise operation. A Microcontroller System (MS) based on the ATmega328P architecture will control and coordinate the detection and pickup systems. Testing and validation

of these components were conducted in simulated controlled laboratory conditions to assess their functionality, reliability, and performance.

The prototype system was designed for proof-of-concept demonstration and may not fully replicate the performance of a commercial-grade solution. Due to time and resource constraints, the prototype system may be limited in terms of scalability and robustness compared to production-ready implementations. Field testing of the prototype on actual roads will be limited to controlled environments and simulated conditions and may not encompass diverse geographical or environmental factors the prototype will be designed for modest speeds for efficiency.

The prototype system may not address all potential challenges associated with real-world deployment, such as maintenance requirements, environmental resilience, or regulatory compliance. Prototyping activities will focus on selected sensor technologies, electromagnet configurations, and control strategies, and may not explore alternative approaches or components extensively. The electromagnet pickup mechanism will be designed for small-scale debris removal and may not be suitable for handling large or heavy metal objects.

Limitations

The limitations of this work are.

1. Optimisation was not considered in the design of the coil and solenoid; hence the power rating is not known. Attempt to increase the magnetic field strength of the electromagnet could result in higher power

consumption, leading to resistive heating which may affect its performance.

2. Simulations were done under laboratory conditions which may not reflect the challenges faced in practical applications.
3. The trade-off between detection sensitivity and detection distance of the MDet is inherent in the physics of electromagnetic induction and can be challenging to overcome.
4. Metals that are not magnetic would not be able to be attracted since the removal system uses only electromagnetic attraction.

In brief, achieving optimal performance of sensor technologies, electromagnet actuators, or control algorithms within the prototype's design constraints can be challenging and can impact their effectiveness.

The Organisation of the Study

This thesis is organised into five chapters. With Chapter One covering the introduction to the study, the remaining work is structured as follows: Chapter Two provides a review of the study-related literature. The principles and theories of electromagnetism, microcontrollers, embedded systems, and photovoltaics are all covered in the evaluated literature. The methodology is presented in Chapter Three. It includes the theoretical formulation and the construction of the following parts: electromagnets, MDet, and the DIY Arduino board. The experimental analysis of some principles and the development of the firmware for controlling InAMDeCS have all been presented. In Chapter Four, the model's output is assessed and discussed, and in Chapter Five, the summary of results, conclusion, and some suggestions for further research are provided.

CHAPTER TWO

LITERATURE REVIEW

Introduction

This chapter reviews scientific literature relevant to the design and prototyping of an InAMDeCS. The system aims to improve road safety by collecting metal debris, including those embedded within road surfaces. The review explores the challenges of metal debris on roads, the limitations of current maintenance strategies, and the role of electromagnets in metal debris removal.

Road Traffic Accidents

Road traffic accidents pose a significant challenge to road safety and socio-economic development globally. It is often synonymous with traffic collisions, road crashes or road accidents and encompasses a wide range of incidents, including collisions between two or more vehicles, single-vehicle accidents, pedestrian crashes (Amoako-Sakyi, 2013), and collisions involving cyclists or motorcyclists (Goniewicz *et al.*, 2016) resulting in significant loss of life, injuries, property damage, and economic losses. (Enu, 2014).

Causes of RTA: The Tyre and Debris as Factors

Numerous factors, including mechanical failure, road conditions, human error, environmental factors (Olajuyigbe *et al.*, 2014), and vehicle design, affect the incidence and severity of accidents (Morgan, 1984). Research by the American Automobile Association Foundation for Traffic Safety in 2004, as

cited by Tefft (2016), indicates that vehicle-related road debris causes about 25,000 accidents and over 100 fatalities annually with interstate routes experiencing debris-related crashes about four times more frequently than those without debris (Chen & Yeh, 2018; Chukwu, Anoliefo, & Ikhajiagbe, 2019).

The tyre factor

Tyres play a critical role in vehicle safety (Chukwugozi, 2016; Edunyah, 2016) and performance, serving as the primary interface between the vehicle and the road surface. Improper tyre functioning can exacerbate the risk of tyre-related incidents, underscoring the importance of tyre management in road safety initiatives. Malfunctioning tyres make road handling difficult. For instance, driving on reduced pressure may lead to skidding as there is reduced traction. Tyre-related issues, including tyre blowouts (Gyimah, 2023), tread wear, and punctures, contribute significantly to RTA (Edunyah, 2016; Bendak, 2008).

Studies have revealed that tyre damage is one of the major causes (Boadu, 2022) of RTA and crashes which could be classified as both human error and mechanical failure. Naeem *et al.* (2017) found that tyre-related RTA remains a concern in the LMIC. According to a report by the Ghana National Road Safety Authority in 2013, as cited by (Edunyah, 2016) malfunctioning tyres significantly contribute to RTA. Research by Naeem *et al.* (2017) reveals that tyre bursts constitute over 50% of RTA categorised as mechanical faults, making tyre blowouts the primary mechanical cause of road accidents. The statistics are presented in Table 1 on page 12.

Table 1: Mechanical Faults Constituting RTA in Various Vehicle Types as Adopted from Naeem *et al.* (2017)

Vehicle Type	Tie Rod (%)	Tyre Burst (%)	Not Known (%)	Wheel (%)	Brake (%)	Other (%)	Number of vehicles
Daihatsu	22.22	77.78					9
Datsun		100					3
Honda	4.44	42.24	42.22	4.44	6.68		45
Hyundai	14.28	50.00	14.29	7.14	14.29		14
Mitsubishi		57.14	14.29	14.29	14.28	14.29	7
SUZUKI	4.53	59.76	4.54	4.53	6.10	4.54	82
Toyota	14.37	62.50	11.25	3.13	5.00	3.75	160
Total	11.25	59.06	14.69	4.69	5.31	5.00	320

Source: Naeem *et al.*, 2017

The metal debris a factor

Road safety discussions often focus on issues such as speeding, intoxicated driving, and careless driving, all of which pose significant risks. However, road debris remains an often-overlooked hazard that can lead to serious accidents. "Road debris" refers to a wide range of items, materials, and substances not typically found in a roadway environment (Strong & Vasques, 2014). A punctured tyre resulting from sharp objects like nails, shattered glass, or metal particles can cause a sudden loss of air pressure, making it challenging for drivers to maintain control of their vehicles (Mousavi *et al.*, 2023). This loss of control may result in rollovers, spinning out, or swerving, increasing the risk of accidents (Borens & Boyd, 2023). Borens and Boyd (2023) assert that even tiny objects can swiftly lead to accidents, potentially resulting in severe injuries such as spinal cord trauma.

As we grapple with the persistent challenge of RTA, it becomes imperative to embrace emerging technologies that promise safer transportation. Going forward, to reduce the frequency and severity of accidents, everyone must commit to this task, ensuring that our journeys are marked by safety, resilience, and a shared responsibility for one another's well-being.

Road Debris Identification and Removal

Identifying possible risk in the debris stream and reducing the management systems' potential environmental effects are necessary for sustainable debris management (Jalloul, Choi, Yesiller, Manheim, & Derrible, 2022). Highway debris poses serious risks to both traffic and worker safety (Strong & Vasques, 2014; Bolanio & Busuyi, 2015). Thus, early detection of road debris is crucial (Huang *et al.*, 2023) for their removal and ensuring road safety (Choe, Wu, Lin, Kwon, & Park, 2023).

Debris identification

Debris identification, which encompasses debris detection and classification, is key for choosing a method to remove the different types of debris (Aleem, Tehsin, Kausar, & Jameel, 2022). According to Balchandani *et al.*, (2017), conventional litter detection on streets is not automated and requires human intervention. They argued that this manual process is not scalable and requires a significant investment in equipment, time, and human resources to monitor and clean every area. To address this issue, remote sensing technology has been developed to effectively identify road waste by Yang, Kim, H., Kim, J., Kim (2020).

Systems like video cameras, ultrasonic sensors, radars and electromagnetic induction (EMI) sensors are normally employed for object detection. It is difficult to detect with an imaging sensor while driving (Yamada, Shibao, & Kajiwra, 2021). There are two main challenges to building a road debris detector: first, data collection; second, the broad variability of road debris, ranging from a very small brick to a large fallen tree (Choe *et al.*, 2023). Various traditional machine learning and deep learning-based techniques give competitive results in debris detection (Aleem *et al.*, 2022).

Classification allows discrimination between potential threats and no-threat objects (Nelson, 2004). Classification of road debris can be based on various factors including size-based classification using image-based detection techniques (Huang, Zhuo, & Yao, 2023), materials-based, and hazard-based. Debris classified based on its material composition emphasises organic debris (such as leaves and branches), inorganic debris (such as rocks and metal objects), and mixed debris (a combination of organic and inorganic materials). Debris can be classified based on its potential hazard to road users. (Balchandani *et al.*, 2017) highlighted that litter detection and classification can be automated using Deep learning for optimisation.

Debris removal

Two broad methods, manual and machine removal, are normally employed in debris removal. Manual removal involves agency workers removing roadway debris by hand. For smaller debris, sweeping staff who use hand-held brooms and parkers (Adedeji & Adebesein, 2020) are normally

employed in cities and residential areas (Brunelli *et al.*, 2023; Pearson, Chen, & Beeso, 2018), as shown in Figure 1.



Figure 1: Pictures of the manual method of street cleaning mostly used in the LMIC (Zoomlion Ghana Limited 2024; Zoomlion Ghana Limited, 2020)

Though this may be good for areas inaccessible to machines, the procedure normally employs eye-spotting as the detection technique (Balchandani *et al.*, 2017), which is inefficient for wide-ranged debris detection. Moreover, street dust, through inhalation, ingestion, and dermal contact absorption, can cause hazards to human health (Dehghani, Moore, Keshavarzi, & Hale, 2017) since heavy metals are poisonous even in small quantities (Ali *et al.*, 2021). Furthermore, it puts agency employees' safety at risk (Bolanio & Busuyi, 2015), particularly on busy or fast-moving roads. (Strong & Vasques, 2014). While the mechanical method of debris removal performs better in specific applications (Mukesh, Manda, Chaitanya, & Mechanical, 2016), limited resources, technologies, and low socio-economic standards compel stakeholders to rely on the manual human effort (Gebremedhn & Raman, 2020).

Meanwhile, innovations and equipment changes have been made so that agency workers can remove rubbish from highways without being in the path of oncoming traffic (Strong & Vasques, 2014). Machine cleaning has the potential to deliver easy and time-efficient cleaning of roads by reducing human effort (Patil & Kambel, 2017; Adedeji & Adebessin, 2020). In the light of these; a sweeping tricycle equipped with brushes, as in Figure 2, is a cost-effective approach to improve the traditional sweeping (Gyasi, 2022; Tetteh, 2020). Although it is inefficient in removing smaller debris, especially in dust; it reduces the workload of the cleaning labour force.



Figure 2: Pictures of some sweeper tricycles with mechanical brooms

(a) Clean Ghana sweeper tricycle (Tetteh, 2020) and (b) Darko's cost-effective sweeper tricycle (Gyasi, 2022)

The mechanisation of road sweeping activities has advanced significantly through the integration of mechanical, electrical, and electronic technologies (Khan, Bhapkar, Bhat, Chougule, & Sangale, 2021). Various technologies, such as mechanical broom sweepers, pressurised water sweepers (flushing machines), vacuum sweepers (Jamil, Muktar, Ali, Qaiser, & Ahmed, 2022), regenerative air sweepers (Brunelli *et al.*, 2023) and magnetic broom sweepers are now being used for debris removal from roadways (Figure 3).

These state-of-the-art sweeping machines, commonly referred to as street sweepers, feature specialised systems that simultaneously sweep and collect debris, improving efficiency and reducing the workload on street cleaning staff (Khan *et al.*, 2021).



Figure 3: Pictures of some state-of-the-art road/street sweeping machines

(a) Gasoline and diesel-powered sweepers and (b) electric sweepers (EVIE street sweeper, n.d.; M3EV electric 100% plug-in, n.d.; D.zero² electric sweeper, n.d.; Electromagnetic sweepers, 2015)

Road sweepers consist of motorized chassis mounted with brushes (Jamil *et al.*, 2022) conveyors, vacuum or suction pumps, and storage bins or flushing machines. Mechanical broom sweepers use rotating brushes to sweep (Khan, Pannase, Sharmagat, & Gohane, 2017) debris into a collection bin, while vacuum sweepers use suction to remove debris. Pressurised water sweepers essentially have water tanks mounted on motorized chassis fitted with pumps and nozzles to provide pressure and a direct stream of water against litter (Brunelli *et al.*, 2023).

The general setback of these mechanised sweepers lies in their robustness, making them very expensive to acquire. Their operations use combustible fuel, which requires ongoing finance and releases greenhouse gases. Additionally, most sweepers require skilled personnel to operate and are not affordable to individuals who intend to use them. However, each method has its setbacks, particularly in the removal of metal debris. Mechanical broom sweepers may struggle to effectively collect small or heavy metal debris from road surfaces. They may not be able to access narrow or hard-to-reach areas where metal debris can accumulate. They can also produce dust and pollute the air (Mukesh *et al.*, 2016) when they are being operated. While flushing machine water can remove some metal debris, it may not be effective for larger or embedded pieces. Moreover, it may disseminate metals that become contaminants for water and the soil, leading to heavy metal pollution (Chukwu *et al.*, 2019). These heavy metals bio-accumulate and pose a long-term harm (Aguirre & Ibikunle, 2014). They affect soil and plant quality (Pikuła & Stępień, 2021) and are also assimilated into the food chain (Alghanmi, Al Sulam, El-Zayat, Alhogbi, & Salam, 2015).

Pressurized water sweepers are more suitable for cleaning surfaces like sidewalks and pavements, rather than roads with heavy metal debris. Moreover, the use of pressurized water sweepers can lead to water wastage and potential contamination of runoff water (Mistry *et al.*, 2023; Mor, 2019). Vacuum sweepers have a limited capacity for storing debris, requiring frequent emptying during operations. Vacuum sweepers may struggle to pick up large or heavy metal debris from road surfaces. Vacuum systems require regular maintenance to ensure optimal performance, which can increase operational costs.

According to Village (2023), a fast, practical, secure, and time-saving method for cleaning factory aisles, roadways, building sites, pathways, loading docks, parking lots, playgrounds, and other surfaces is to use magnetic sweepers, also called magnetic broom. While electromagnets may have higher initial costs than permanent magnets, the use of electromagnets in magnetic broom sweepers offers greater flexibility, efficiency, and control, making them a preferred choice for applications requiring selective and efficient collection of metal debris. The Eriez magnetic sweeper has been designed to remove numerous safety risks MD, cut down on equipment downtime, and avoid expensive tyre damage in a single swift sweep (Eriez magnetic sweeper, n.d.). With an eye on affordability and simplicity, SOLLAU created the MS FALCON magnetic sweepers (ACCG Air Consulting [ACCGAC], n.d.), which are more straightforward and reasonably priced. However, the setback of these magnetic sweepers lies in their robustness, making them very expensive to acquire.



Figure 4: Picture of the Eriez magnetic sweepers (Eriez magnetic sweepers, n.d.)



Figure 5: Picture of the FALCON MS magnetic sweepers (ACCGAC, n.d.)

However, these road sweepers powered by diesel engines (Eriez, n.d.; ACCGAC, n.d.) lead to the release of chemicals like CO₂ and particulate matter, which contaminate the air (Yim & Kim, 2021). For instance, a 4.8kW diesel generator is installed independently on the towing angle to provide the necessary current to generate the powerful Electromagnetic (EM) field (Eriez, n.d.). It also requires ongoing financing which has been a difficult task for the LMICs. Meanwhile, the sun is an inexhaustible reservoir of renewable, clean (Maka, Salem, & Mehmood, 2021) and environmentally friendly energy with a life expectancy of 4.5 billion years (Asumadu-Sarkodie & Owusu, 2016). Solar energy is thus emerging as a possible alternative energy source (Lupangu & Bansal, 2018) to traditional fuels, (Attachie & Amuzuvi, 2013) since vehicles can be powered by electricity (Egner & Trosvik, 2018). Hence, the shift to solar vehicles is crucial at the moment considering the volatile nature of oil prices (Aguirre & Ibikunle, 2014) and the pollution caused by burning fossil fuels (Egner & Trosvik, 2018).

Solar energy technology faces challenges due to daily fluctuations in radiant energy and advert weather conditions (Lupangu & Bansal, 2018; Hayat,

Ali, Monyake, Alagha, & Ahmed, 2019). However, storage facilities like solar cells (Sharma, S., Jain, & Sharma, 2015) can help in harvesting and storing energy during difficult times. According to Gunes & Sariciftci (2008) silicon solar cells have high efficiency but are very expensive while Attachie and Amuzuvi (2013) argue that, despite the initial high expenditure on the harvesting and storage equipment, the overall cost is still lower than other energy sources.

Summing up, MD left uncollected, can be unsightly and disruptive to a facility's operations, posing risks and hazards. While mechanized broom sweepers, pressurized water sweepers, and vacuum sweepers are effective for large-scale road cleaning, they require ongoing financing, which is challenging for low- and middle-income countries. According to Jeong & Ra, (2022), cleaning with brooms or vacuum sweepers sometimes disseminates environmental contaminants because road dust is highly laden with heavy metals. Also, they are inefficient in removing all sizes of metal debris. They recommend that the most efficient technique is to create a magnetic system with a road sweeper.

Active debris removal techniques

Active Debris Removal (ADR) is a method used to remove space debris employing such techniques as: capture and removal, active propulsion, tethers and electrodynamic tethers, and laser ablation (Liu, Zhang, Li, & Yang, 2013). Patel and Aslanov (2020) developed a device to catch and accelerate/decelerate electrically conductive trash in space, the fundamental tenet of which is a theory consistent with Lenz's law and Faraday's law of induction and the Lorentz force.

Their method involved using a fictitious toroidal coil that was supposed to produce a strong enough magnetic field when an electrical current was provided, which is realised on the moving debris that is electrically conductive. Several creative technological ideas, conceptual designs, and demonstration tests for debris removal systems report on two approaches – contact and non-contact (Patel & Aslanov, 2020). The contact approach requires the detection and subsequently location of the debris with great precision. This thus, requires data and telecommunication network for Global Positioning System (GPS) service or the use of cameras and algorithms for calculation the position of the object (Lupangu & Bansal, 2018). It utilises a contact medium such as a robotic arm to attach to the target object which is rather complicated when it comes to effectiveness, efficiency and time of the operation (Patel & Aslanov, 2020).

The Noncontact Active Debris Removal (NADR) method makes use of eddy current effects and the use of drag and magnetic force. A useful technique for contactless debris removal requires a look into the fundamental laws that govern the characteristics of magnetic interaction of the debris (Patel & Aslanov, 2020). However, designing an effective magnetic field system, debris identification, and tracking remain significant challenges and according to Liu, Zhang, Li, and Yang (2014) and Patel and Aslanov (2020), experimental studies, numerical simulations, and prototype testing are still in the developmental stage to validate the effectiveness and scalability of NADR for practical debris removal mission.

By harnessing the power of electromagnetism, this technology, NADR, offers an effective proactive approach to managing MD on roads, ensuring smoother and safer journeys for road users.

Metal Detection Systems

The commonly used metal detection technologies are the radar system and the EMI sensor systems. Radar uses two factors to identify metals: the material's specific sound speed and a metal's reflection coefficient to electromagnetic radiation (Nelson, 2004) while the EMI sensor utilises disparity between transmitted and returned magnetic fields. (Alauddin, Islam, & Zaman, 2016).

EMI metal detectors are inductors that transmit magnetic fields and analyse the returned field to detect metal targets (Alauddin *et al.*, 2016; Candy, n.d.; Bryakin, Bochkarrev, Khramshin, & Khramshina, 2021). These detectors induce magnetism or eddy currents in metal targets, making them eddy current devices (Bruschini, 2002). Metal detectors measure the effects of a metal object on a magnetic field, which can involve monitoring a coil's inductance change due to a changing magnetic field, where inductance is directly dependent on magnetic permeability, which can vary in the presence of ferrous or non-ferrous materials (Bryakin, *et al.*, 2021; Maurek, 2017; Liu, 2014).

Metal detectors work on the beat oscillation (BO) principle, with methods like beat frequency oscillation (BFO), off-resonance (OR), induction balance (IB), and pulse induction (PI) being used (Bryakin, *et al.*, 2021, 2021; Boxall, Purvis, Madge, & Banerjee, 2005). PI metal detectors use pulse induction technology, transmitting a magnetic field and analysing the return signal from the target and environment in the form of back EMF (Bryakin, *et al.*, 2021, 2021). When metal passes through this field, it causes changes in the magnetic flux lines, generating detectable electrical signals (Bryakin, *et al.*, 2021, 2021). PI systems may use a single coil for both transmission and reception or separate

coils (Bryakin, *et al.*, 2021; Boxall, 2005; Nelson, 2004). Overall, PI metal detectors have a simpler design compared to other types (Bryakin, *et al.*, 2021) and are also immune to ground mineralisation, which short coming of the other EMI MDet principles (Citak, 2020).

The detector head (Search Coil)

The detector head is a critical component of a metal detector (MDet) system, responsible for detecting metallic targets. Most MDets fall into two categories based on their detector heads: those with a 'balance coil' (BC) and those with a 'ferrous-in-foil' detector head. The former can detect all metal types, while the latter is limited to ferrous metals. The BC detector head consists of 'transmit' and 'receive' coils. As a metal target passes through the transmit coil's alternating magnetic field, a secondary electromagnetic field is generated (Yousif, 2021), which is detected by the receive coil. The size of the coil is determined by the smallest detectable object size and the required detection depth. Typically, the smallest detectable object is about 5% of the coil's diameter, and the maximum detection depth is around five times the coil's diameter. The magnetic field lines of a flat inductance coil usually extend up to the coil's diameter. Search coils are air cored, so the permittivity of free space is sufficient for their inductance formula (Bies, n.d.).

The return signals

The signal induced in the receive coil is made up of two simultaneous components: the reactive signal 'X' and the resistive signal 'R'; (Alauddin *et al.*, 2016; Candy, n.d.), both of which vary depending on the distance of the target from the coil (Alauddin *et al.*, 2016). Most MDets have discriminator controls

that let users pick the type of metal they are looking for based on two categories: ferrous/non-ferrous (+/- X) and conductivity (time constant). Ferrous metals have high inductance due to their magnetic properties (Candy, n.d.), which makes them easier to detect despite usually having poor electrical conductivity. Eddy current flow measurements help metal detectors differentiate non-ferrous objects based on a target's "time constant" (Citak, 2020) or "conductivity", determined by target inductance and target conductivity. Inductance is the length of the eddy current channel, while conductivity is how easily eddy currents flow. High conductivity results in easy eddy current flow, while low conductivity causes excessive eddy current friction. The greater the time constant, the better the target conducts electricity and the larger the inductance. The time constants differ significantly between targets (Candy, n.d.).

Chapter Summary

The contribution of MD to RTA is significant and impact societies negatively. Collective measures; such as regular road maintenance and prompt removal of MD using magnetic system has been revealed to be an effective method for MD management. However, for efficient power management, creating smart systems for devices together with NADR replica for road debris removal is considered a better alternative for MD management. Moreover, solar energy offers a low cost and environmentally benign energy source for road cleaning machines.

CHAPTER THREE

METHODOLOGY

Introduction

In the current chapter, the methodology and the materials used in executing the research objectives are presented. It comprises the modelling of the ideas and concepts from theories and phenomena into the physical hardware components by the creation of a prototype.

Research Design

The study makes use of a true experimental research design (TERD). The TERD is essential for promoting scientifically supported efforts such as product rebranding (Osei-Kyei & Chan, 2017) and fostering innovation (Bhat, n.d.; Taherdoost, 2022). One of the simplest research methodologies that gives researchers a great deal of control and yields particular results is the TERD, which is primarily utilised in the physical sciences (Gaille, 2017). Additionally, it enables replication, making it simple to recreate a natural situation.

While internal validity in experimental research design ensures accurate measurement of the relationship between variables, it often occurs in controlled environments that may not reflect real-world situations. As a result, findings may not generalize to broader populations or settings. When settings have high internal validity but low external validity, results may be distorted (Cuncic, 2024; Gaille, 2017). This trade-off is common in experimental research, where maintaining accuracy (high internal validity) can limit the applicability of findings to real-world contexts (low external validity). They may not always be

feasible or ethical in certain situations; however, alternative research designs such as quasi-experimental or correlational designs may be used instead since experimental research can be combined with other research methods (Gaille, 2017).

Correlational designs identify relationships between variables but cannot control for confounding variables or determine causality direction. Longitudinal designs are useful for studying developmental changes over time but may suffer from issues like attrition and practice effects. Case studies offer detailed insights but lack generalisability and researcher bias (Taherdoost, 2022). Experimental designs allow manipulation of variables, characterised by random assignment of participants to different conditions, to minimise bias and ensure observed effects can be attributed to the manipulated variables. Researchers aim to control or minimise the influence of extraneous variables through methods like random assignment, matching, or statistical control. Quasi-experiment designs lack random assignment to groups and manipulation of variables, but they can be useful when random assignment is not feasible or ethical.

True experimental designs involve multiple replications to assess reliability and generalisability, including a control group that does not receive the intervention. Valid and reliable measurement instruments are essential for accurate data. Random assignment minimises selection bias (Taherdoost, 2022) and ensures differences in outcome variables between groups can be attributed to the experimental manipulation.

Metal Detector Design Methodology

The key considerations for designing MDet are the detection principle, the inductance of the search head, and the Drive (or controller) Electronics (DE).

Metal detection principle

The Pulse Induction (PI) metal detection principle is primarily adopted for this work because PI MDets have superior performance in highly mineralized soil (Rerkratn, Petchmaneelumka, Kongkauroptom, Kraisoda, & Kaewpoonsuk, 2011) and a deeper detecting depth for metal than the VLF MDets (Bernzweig, 2023), although the VLF MDets have exceptional abilities to distinguish between ferrous and non-ferrous objects (Firdaus, *et al.*, 2012). Moreover, the same search coil can serve the purpose of the TC and the RC (Boxal, *et al.*, 2005) in the PI MDets. The design block diagram for the PI detection system is shown in Figure 6 depicting the various activities.

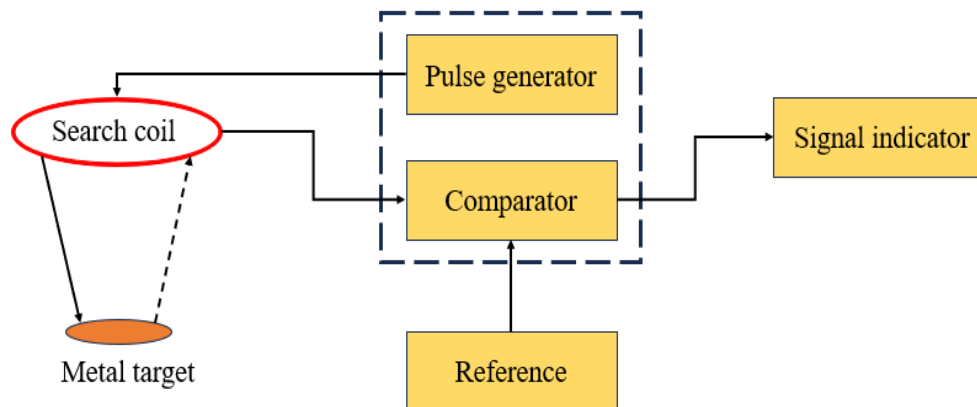


Figure 6: Design block diagram of the PI metal detector system

In Figure 7, on page 30, a pulsating current (I) is applied to a coil, resulting in the creation of a magnetic flux (Φ_B). As this field moves across a

metal, it induces eddy currents (I_{eddy}) in the metal. These eddy currents produce their magnetic flux (Φ_B^{eddy}).

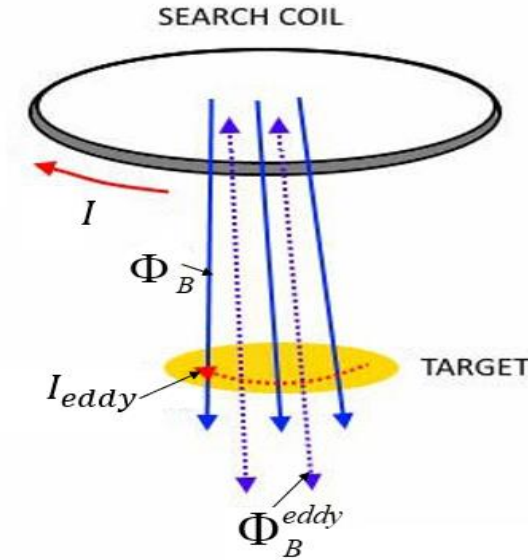


Figure 7: PI metal detector working principle as adapted from (FoxyPI, 2019)

The theoretical formulation of the search coil

The fundamental physics principle of MDets is Faraday's law" (Cross, 2008; Pine, King, Morrison, Morrison, & Mcneil, 2004) The most important physical EM parameter of metal detectors is the induced voltage (V_L), which depends on the inductance of the coil (L), which in turn depends on the magnetic flux (Φ_B) (Paul, 2010) as

$$V_L = -\frac{d\Phi_B}{dt} = -L \frac{dI}{dt} \quad (1)$$

The inductance of a planar circular coil of N turns of wire with coil radius R is given by equation (2) below.

$$L_{coil} = \mu_0 \frac{N^2 R_{coil}}{2} \quad (2)$$

where L_{coil} , N and R_{coil} are the inductance, the number of turns and the radius of the coil respectively and μ_0 is the magnetic permeability of free space.

(See Appendix C).

The preferred inductance for low-current, high-frequency switching devices (Abusara & Sharkh, 2013) ranges from $300\mu H$ to $500\mu H$ (Liffran, 2008).

The number of turns of the coil of radius R_{coil} and inductance L_{coil} can be calculated by

$$N = \sqrt{\frac{2L_{coil}}{\mu_0 R_{coil}}} \quad (3)$$

The search coil design

Experimental verification of the inductance equation

A flat circular coil of radius 10 cm and 600 turns was constructed from a standard insulated copper wire. The inductance was calculated using equation (2) and subsequently determined using the Cobra3 Experiment and the two results compared in Experiment 1.

(See Appendix B for Experiment 1).

Fabrication of the search coil

Equation (3) was used to calculate the number of turns of the coil and the other design parameters of the coils were analysed in MATLAB to ascertain how manipulating some of the N and R could affect the inductance.

(See Appendix C for the simulation).

The drive electronic circuit formulation

The LC Oscillator

The DE works like the principle of an LC Oscillator (Meaney, n.d.; Yousif, 2021). The heart of the LC oscillator is the LC tank circuit (Aslam, 2005; Garinto, Syahriar, & Budiyanto, 2020), which consists of an inductor (L) and a capacitor (C) connected in parallel or series (Sarker, 2023). The tank circuit stores energy in the form of an electric field (Klangmuang *et al.*, 2023) (in the capacitor) and a magnetic field (in the inductor). The energy stored in the capacitor and inductor oscillates back and forth (Kumar & Khalkho, 2016) between the electric and magnetic fields, resulting in a periodic exchange of energy between the two components.

The energy stored in the electric field and magnetic field are given by equations (4) and (5) respectively (Paul, 2010).

$$W_E = \frac{1}{2} \iiint \vec{D} \cdot \vec{E} dv = \frac{1}{2} \epsilon \int \vec{E}^2 dv = \frac{1}{2} CV^2 \quad (4)$$

$$W_B = \frac{1}{2} \iiint \vec{B} \cdot \vec{H} dv = \frac{1}{2} \mu \int \vec{H}^2 dv = \frac{1}{2} LI^2 \quad (5)$$

This continuous exchange of energy leads to oscillations at a specific resonant frequency f determined by the values of the inductance (L) and capacitance (C) in the circuit. The LC oscillator's frequency is the parameter that determines the time constant (τ) of the metal detector. It relates to the time constant as: $f \propto \tau^{-1}$. This continuous exchange of energy leads to oscillations at a specific resonant frequency f determined by the values of the inductance (L) and capacitance (C) in the circuit. The LC oscillator's frequency is the parameter that determines the time constant of the metal detector. It relates to the time constant as: $f \propto \tau^{-1}$.

Consider the LC tank circuit (Teja, 2024) in Figure 8 below. If the applied signal frequency is constant, the reactance or impedance between terminals "a" and "c" relies on the values of L and C. Reactance changes in response to changes in the inductance value or the capacitance.

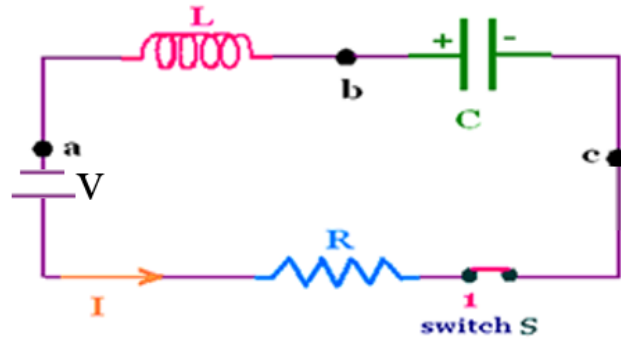


Figure 8: RLC circuit for demonstrating magnetic oscillation (Raja, 2015)

If the capacitance is fixed, then the change reactance dependence on the change in inductance (Raja, 2015). The resonance frequency of an LC vibration is determined when the reactance of the capacitor and the inductor are the same, that is, $X_L = X_C$ (Aslam, 2005). The reactance of the capacitor and the inductor

at frequency f are respectively given as $X_C = \frac{1}{2\pi fC}$ and $X_L = 2\pi fL$. The

frequency of oscillation of an LC oscillator is thus expressed as

$$f = \frac{1}{2\pi\sqrt{LC}} \quad (6)$$

The frequency changes if either the capacitance or inductance changes (Garinto *et al.*, 2020). If an LC oscillator is designed with a fixed capacitor, the oscillator's frequency depends on a change in the inductance of the inductor.

The oscillator frequency then relates to the inductance as

$$f = \frac{K}{\sqrt{L}} \quad (7)$$

Where $K = \frac{1}{2\pi\sqrt{C}}$. The oscillator frequency is inversely related to the inductance. Thus, a decrease in frequency implies an increase in inductance.

The drive electronics circuit design

The DE components were assembled following the circuit diagram shown in Figure 9. The components used included:

- 1) 555 timer IC (1): A key component used to generate timing signals or pulses.
- 2) 2.2 μF capacitor (2) and 10 μF capacitor (1): These capacitors store and release electrical energy, each with a specific value for different roles in the circuit.
- 3) 47 $\text{k}\Omega$ resistor (1): This resistor limits the current flow, with the 47 $\text{k}\Omega$ value chosen to fit the circuit's design needs.
- 4) 9 V energizer batteries (2): These power the circuit, either providing a total of 18 V or being used for separate components.
- 5) Breadboard (1): A tool for assembling the circuit without soldering, allowing easy placement and connection of parts.
- 6) Jumper wires (10): Used to connect the components on the breadboard.
- 7) Buzzer (8 Ω) (1): Produces a sound when the circuit is activated, likely used to signal the detection of metal.
- 8) Switch (1): Turns the circuit on and off.
- 9) Search coil (1) with 120 turns and a 7 cm diameter: This coil generates a magnetic field to detect metal objects.
- 10) Metal objects (6): These are test objects used to check the circuit's functionality.

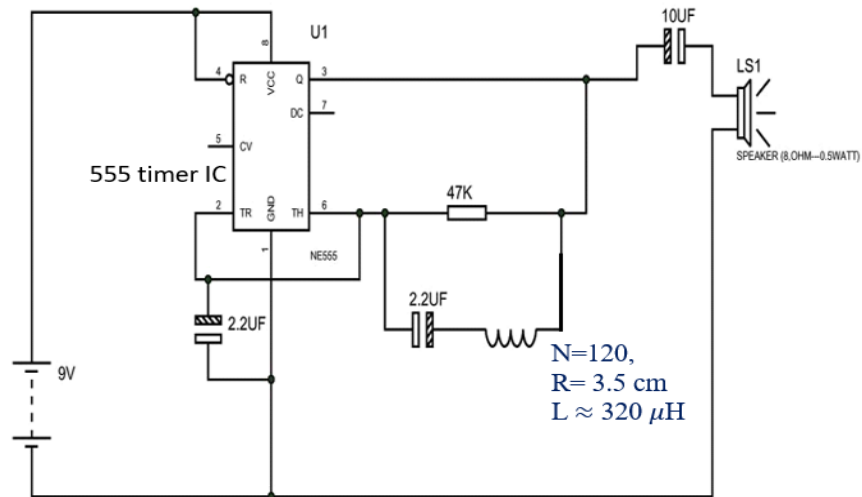


Figure 9: Pulse induction metal detector drive circuit (Shahjahan, 2022)

Experimental testing of metal detector drive circuit

Experiment 2 was performed to validate the conformance of the MDS design. The circuit in Figure 9 was assembled on a breadboard as shown in Figure 10 (a), and tested by sweeping the metals shown in Figure 10 (b) across the search coil and the change in tone of the buzzer was observed for each metal.

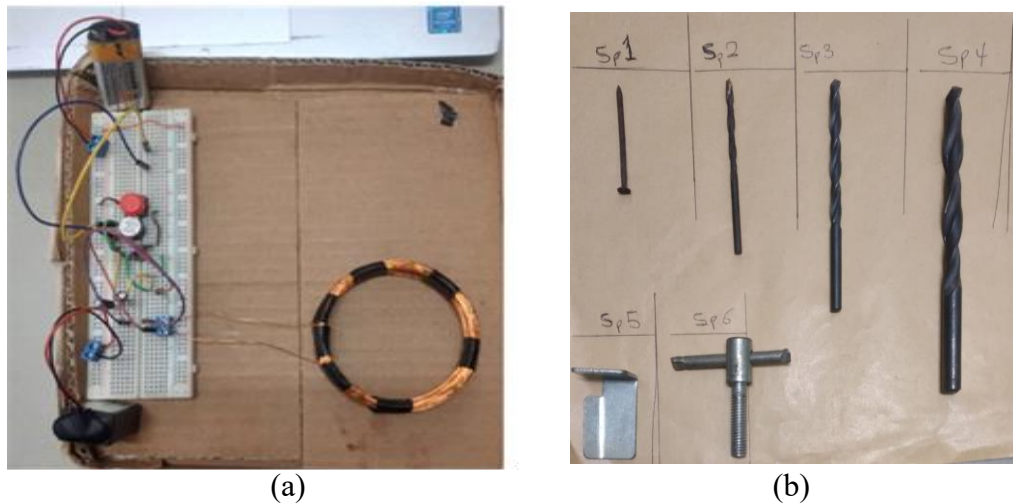


Figure 10: Pictures of the experimental setup used to test the functionality of the designed MDet (a) assemble MDet circuit components and (b) metals swept across the MD's search coil

Electromagnet Design Methodology

Magnetic attraction and removal rely on the interaction between magnetic fields and ferromagnetic materials (Coey, 2010). The electromagnet consists of a magnetic circuit in which a solenoid is connected in series to a switch and a voltage source. From an electromagnetism point of view, the current following through such a circuit would produce a magnetic field around the solenoid (Coey, 2010; Jiles, 1991).

Magnetic circuit

An electromagnet designs are aimed at obtaining the maximum energy stored with minimum power loss. The key magnetic specifications, though may vary, are the magnetic circuit providing the Magnetomotive Force (MMF), and the Lifting Force (LF). However, MMF and LF are embedded in other factors such as the magnetic field strength, the inductance. The magnetic specifications are discussed in below.

$$(1) \quad \textit{The magnetic field strength } (\vec{B})$$

The \vec{B} represents the intensity of the magnetic field produced by the electromagnet, measured in tesla (T) or gauss (G). It is expressed as

$$\vec{B} = \frac{\mu_0 \cdot N \cdot I}{l} \quad (8)$$

But from Ohm's law,

$$I = \frac{V}{R} \quad (9)$$

Hence,

$$\vec{B} = \frac{\mu_0 \cdot N}{l} \cdot \frac{V}{R} \quad (10)$$

where V is the voltage and R is the electrical resistance of the wire, expressed in terms of resistivity ρ , length l , and area of cross-section of wire

$A_{\text{cross-section}}^{\text{wire}}$ as

$$R = \frac{\rho l}{A_{\text{cross-section}}^{\text{wire}}} \quad (11)$$

(2) *The magnetomotive force*

The MMF is a measure of the magnetic potential difference across the magnetic circuit. It is directly proportional to the product of I and N as

$$F_{\text{MMF}} = N.I \quad (12)$$

Where F_{MMF} is the MMF measured in ampere-turns (A-t).

(3) *The inductance*

The inductance, the electromagnet's ability to store energy in the form of magnetic field when current flows, is measured in henry (H). The inductance of an electromagnet winding (Underhill, 2016) is best determined using

$$L_{\text{solenoid}} = \mu_r \mu_0 \frac{N^2 A}{l} \quad (13)$$

where the parameters have their usual meaning.

(See Appendix D).

(4) *The lifting capacity*

The LF (also known as holding force or lifting capacity) is the maximum force exerted by the electromagnet to attract and hold ferromagnetic objects, measured in newtons (N). In practice, the actual LF may be influenced by factors like the geometry of the object being lifted, the distance between the electromagnet and the object, and the efficiency of the electromagnet design.

Assuming a uniform body for the object being attracted, the basic estimation of the lifting capacity of an electromagnet in an ideal environment is given by

$$F_{lift} = \mu_r \bar{B} \cdot A_{cross-sectional} \quad (14)$$

where \bar{B} is the magnetic field strength (in tesla, T), $A_{cross-sectional}$ is the cross-sectional area of the solenoid (in square metres, m^2), and μ_r is the relative permeability of the material being lifted (in tesla meter per ampere, T.m/A).

$$F_{lift} = \mu_r \cdot \frac{\mu_0 \cdot N \cdot I}{l} \cdot A_{cross-sectional} \quad (15)$$

The parameters in equation (15) have their usual meanings.

It can be seen from equation (15) that the LF is directly proportional to the turn density $n = \frac{N}{l}$. Therefore, multiple layers of winding can give an optimised lifting capacity. However, when there are multiple layers of wire wound around the core, it affects the effective cross-sectional area of the solenoid. The effective cross-sectional area is the area perpendicular to the axis of the coil that contributes to the overall magnetic field. Repeated winding introduces a new factor known as the Fill Factor (FF) or “packing factor.” The FF is the ratio of the cross-sectional area filled with wire to the total cross-sectional area of the solenoid. It accounts for the fact that, as you add more layers of winding, the space between the wires and layers increases, reducing the effective contribution of the additional turns to the magnetic field. The formula for the FF is given by:

$$FF = \frac{A_{magnetic}}{A_{total}} \quad (16)$$

The effective cross-sectional area can then be calculated by equation (17) below.

$$A_{eff} = FF.A_{total} \quad (17)$$

where A_{eff} is the effective cross-sectional area and A_{total} is the total cross-sectional area.

As the number of winding layers increase, the FF decreases due to the increased space between the wires and layers. This reduction in the FF ultimately impacts the effective cross-sectional area and can affect the overall magnetic field strength. In practical terms, optimising the winding density and layering in a solenoid is a trade-off. While increasing the number of turns (layers) can increase the magnetic field strength, the diminishing FF may lead to diminishing returns. Achieving the right balance is essential for designing an electromagnet with the desired performance characteristics for a specific application. The optimised lifting capacity then becomes:

$$\begin{aligned} F_{lift} &= \mu_r \frac{\mu_0 \cdot N \cdot I}{l} \cdot A_{eff} \\ &= \mu_r \mu_0 \frac{A_{eff}}{l} \cdot F_{MMF} \end{aligned} \quad (18)$$

Thus, the lifting capacity of the electromagnet depends directly on the MMF.

(5) *The power rating*

The temperature rating which indicates the maximum temperature at which the electromagnet can operate safely and reliably without degradation of performance or damage. It depends on the resistance of the coil which affects the amount of current required to generate the required magnetic field strength and the operating voltage or the current that specifies the electrical requirements

for powering the electromagnet. Since $I \propto V$ according to Ohm's law, the power dissipated is represented mathematically by equations (19) and (20) below.

$$\begin{aligned} P &= IV \\ &= I^2 R \\ &= \frac{V^2}{R} \end{aligned} \quad (19)$$

$$P = \frac{\rho l}{A_{\text{cross-section}}^{\text{wire}}} I^2 \quad (20)$$

Where P is the power dissipated in the form of heat as a result of current flowing through the solenoid (Akash, 2016).

This power dissipated, known as joule heating, affect the performance of the electromagnet. As the temperature increases, the resistance increases and the magnetic field increases as well as drift velocity decreases. Equation (20) depicts that lower gauge wire can carry more current without heating. Lower gauge wires have less resistance since: (1) the length of wire required for a given effective area is less than wire with high gauge value and (2) it has bigger cross-sectional area, which relates to resistance inversely. This means that using a low gauge wire for a given voltage results in less heat being generated than a high gauge wire. Low gauge wires produce stronger magnetic fields in electromagnets due to their larger diameters, lower resistance per unit length allowing for more current flow.

Construction and testing of the electromagnets

A magnetic functionality set consists of the magnetic circuit and the weight(s) to be attracted by the magnet. Two solenoids were wound on cylindrical iron cores. Table 2, on page 40, shows the specifications of the wires used for the solenoid.

Table 2: The design parameters of the solenoids S₁ and S₂

Solenoid	Wire diameter /mm	Magnetic length /cm	Number of turns	Diameter of core d _c /cm	Diameter of solenoid d _s /cm
S1	1.11	2.0	160	1	2.7
S2	2.21	3.5	60	1	2.5

Source: Researcher, 2024

(See Appendix G for the simulation of the design parameters).

Experiment 3 was then performed to determine the following:

- (1) how MMF affects the lifting capacity (LF), and
- (2) how the separation between solenoid and weights ($r = d$) being lifted are related.

(See Appendix H for details of Experiment 3).

The Design Methodology of the Microcontroller

The Arduino microcontroller was designed by first wiring the ATmega328P microcontroller using Figure 11 as a guide and then burning a bootloader onto the Arduino board.

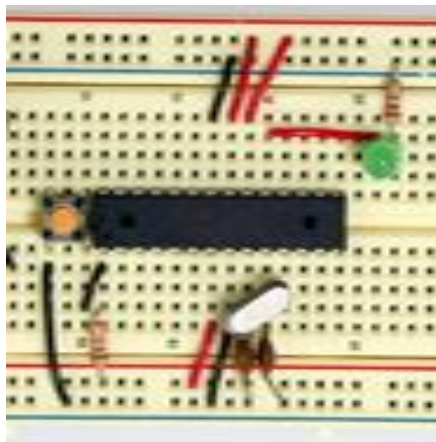


Figure 11: Picture of the assembled Arduino component on a breadboard as a guide for building an Arduino board (Mellis, 2008)

Table 3: Optoelectronic Components Used in Constructing the Arduino

Board	
Component	Quantity
General-purpose circuit board	1
ATmega328P microcontroller	1
7805 Voltage regulators	1
10 μ F capacitor	2
22 pF capacitor	2
220 Ω resistor	1
10 k Ω resistor	1
LEDs	2

Source: Researcher, 2024

Other components and apparatus used include: a digital multimeter (270 B BK Precision tool kit), cutter, three pairs of pliers, soldering iron, solder, and Arduino UNO board.

Wiring up the ATmega328P microcontroller

The microcontroller was inserted into the breadboard. The crystal oscillator was connected between pins 9 and 10 of the microcontroller. Two 22 pF capacitors were connected between each crystal pin and the ground rail. For the power connection, pins 7 and 8 were connected to the positive and the ground rails on the breadboard respectively. Also, pins 20 and 21 to VCC and pin 22 to GND. The 5V power supply and the “+ terminal” were connected to the positive rail and the “– terminal” to and the ground rail on the breadboard. A push-button switch was then connected between pin 1 of the microcontroller and the positive rail for manual reset the microcontroller.

Burning of the Arduino bootloader onto the DIY Arduino.

The ATmega328P was programmed after being installed on the PCB in a procedure known as In-System Programming (ISP) (Fitzgerald, 2023). An Arduino board as an ISP was used to burn the bootloader onto the ATmega 328P. (See Appendix J for details).

Prototyping of InAMDeCS parts.

The prototyped InAMDeCS consists of four main parts: the metal detection system, the controller, the actuator system and the power system. The following subsections gives the construction or assembling procedure. Figure 12 shows a flow chart of the concept of the prototype.

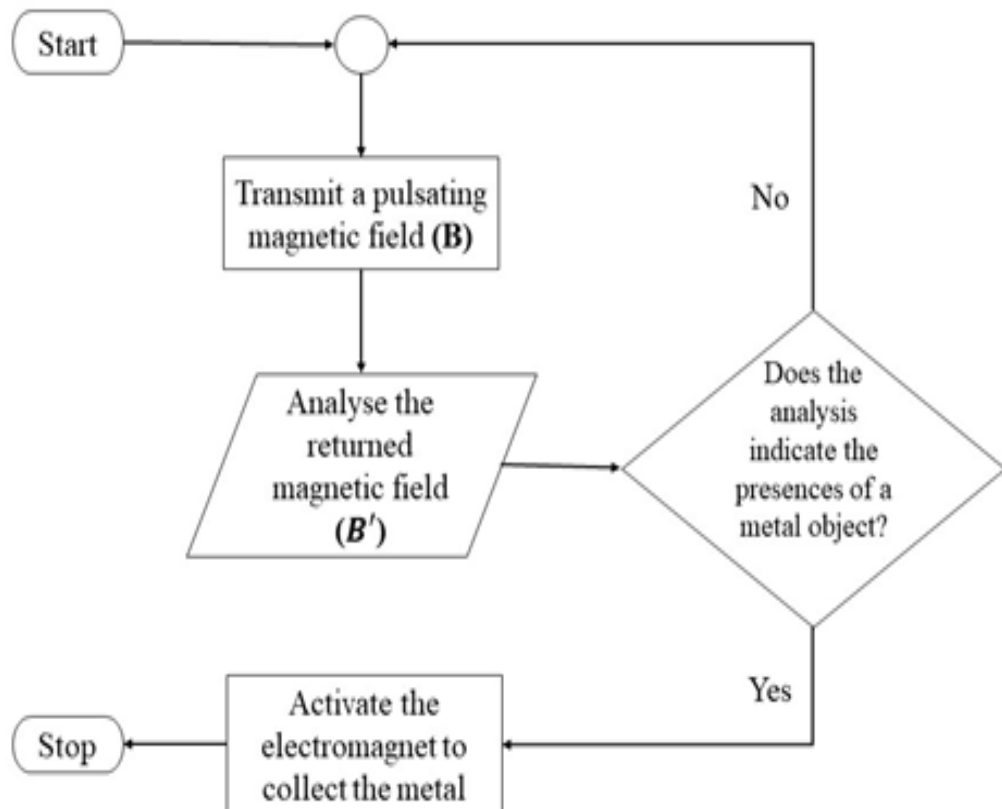


Figure 12: Flowchart of the conceptual framework of InAMDeCS

Construction of the metal detector system

The MDet system was soldered on a general-purpose printed circuit board. The components, materials, and principles used in subsection 3.2. were adopted for this part. Two LEDs were added: one for power indication and the other for visual indication of metal detection. A potentiometer was added to vary the transmit field.

Construction of the controller

The controller system was constructed based on the designed in subsection 3.4. A general-purpose PCB was used instead of a breadboard. A push-button switch was connected between pin 1 (RESET) and the positive rail to be used to reset the microcontroller. The Arduino microcontroller was then uploaded with the firmware for coordination. Signals from the MDet system are sent to the microcontroller via wired communication lines.

(See Appendix G for the code).

The power system assembly

The power system was designed to use a 12 V battery that is being charged by a solar panel. In addition, a voltage regulator was added to the controller to allow connection to the 12 V. The power line connection is outlined in Table 4 on page 44. A 0.1 μF capacitor was placed between V_{in} and V_{out} and another between V_{out} of the voltage regulator GND to stabilize the power supply.

Table 4: Power line mapping for InAMDeCS power system

Voltage Regulator Pin	External Power Supply Terminal	Trail on PCB
V_{in}	+	
GND	-	GND
V_{out}		VCC

Source: Researcher, 2024

The actuator system assembly

The prototyped actuator system consists of a relay for powering the electromagnet based on instructions from the microcontroller unit. The relay connections are summarised in Table 5 below.

Table 5: Summary of the relay connections mapping

Controller Pins	Relay Pins/Contacts	Battery Terminals	Solenoid Ends
GND	GND		
5 V	VCC		
12	Signal (SIG)		
	Common (COM)	-	1
	Normal close (NC)	+	
	Normal open (NO)		2

Source: Researcher, 2024

Chapter Summary

In this chapter, the relevant theories and principles guiding EM induction and magnetic attraction have been outlined. The theoretical formulation made use of magnetic field theories to derive expressions for the inductance of the MDet and the lifting capacity of the electromagnet. The materials and components, design specifications and methodology for the metal detector, the electromagnet and the microcontroller have been presented as well.

CHAPTER FOUR

RESULTS AND DISCUSSION

Introduction

This chapter presents the results obtained from the physical analysis performed on the prototype parts (under laboratory conditions) and a discussion of the results. The MDet successfully detected the presence of metal objects in the form of a change in the frequency of the sound produced by the buzzer. The electromagnet could attract metal objects of about 0.5 kg at a mean distance of 3 cm. The attraction was better when voltages were increased to 7 V and above.

The wire selection was based on conductivity-to-weight ratio, ductility and cost. A round-shaped wire was considered; though the square shape allows more densely packed turns, twists introduced during winding may result in highly irregular geometry. The choice of the wire size, determined by American Wire Gauge (AWG) was informed by the frequency of waves generated by the tank circuit. According to Mistri, Asheer, Kumari, Toppo, and Singh (2017), LC oscillators are widely used to generate frequencies ranging from 10 kHz to 100 MHz.

The challenge with MDet, however, lies in balancing the detection range with the minimum detectable metal object size. On the other hand, for the electromagnet (S2) the power source was shut off automatically when the voltage was increased to 8 V and above. This is likely due to joule's heating, indicating that the current drawn exceeded safe operating limits. This triggered the power system's a safety mechanism to prevent hazards or damage.

These observations suggest that optimal coil design and improved electronics and discriminating algorithm are areas for improvement for the MDet while optimal design that effectively considers resistance, current flow, magnetic field strength, heat dissipation and safety mechanisms in electrical circuits should be considered.

Results of the Experimental Verification of the Inductance Equation

The inductance determined by equation (2) - 0.022619 H and experiment (0.024275 H) were almost the same. The difference (0.0011656 H) can be attributed for errors in the experimental procedure and irregularities in the winding of the search coil. With control experiment, the inductance indicated on the coil was 15 mH as against the experimental result of 14.05946, with a difference of 0.94054 mH. Thus, the inductance equation is appropriate for determining the winding specifications the search coil.

Results of the Analysis of the Variation of Inductance with Number of Turns (N) and Radius of Coil (R)

Table 6, on page 47, gives the parameters of the five coils of different specifications of radii and the number of turns used for the analysis. Coils C2 and C3 had the same radius ($R = 4$ cm) but different number of turns. The inductance of C3 ($N = 130$) was observed to be higher than C2 ($N = 75$). Coils C3 and C4 had the same number of turns ($N = 130$) and different radii: C3 ($R = 4$ cm) and C4 ($R = 7$ cm). Coil C4 had higher inductance ($L = 0.7433$ mH) than coil C3 ($L = 0.4247$ mH).

Table 6: Parameters of the coils used for the analysis of the variation of inductance with radius and number of turns of coil

Coil	Radius / cm	Number of turns	Inductance $\times 10^{-3}$ /H
C1	3.25	80	0.1307
C2	4.00	75	0.1414
C3	4.00	130	0.4247
C4	7.00	130	0.7433
C5	12.00	45	0.1527

Source: Researcher, 2024

The graph in Figure 13 below shows the relationship between L and R for the five different coils. It can be seen that L increases as R increases. From Figure 13 (b), the line falls between 0.07 m and 0.12 m. This is as a result of the difference in the number of turns of the coils.

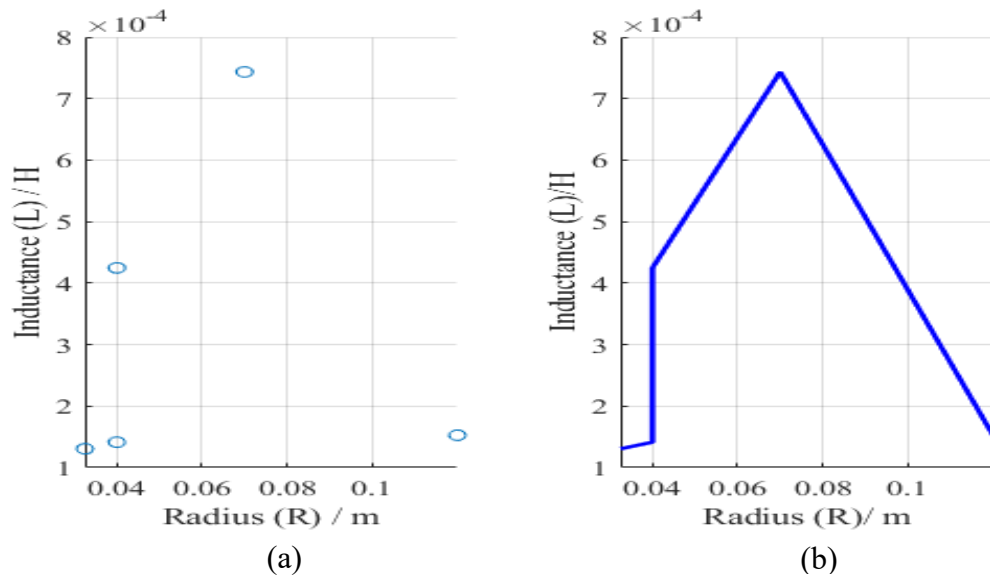


Figure 13: Graphs of inductance (L) against the radius of the coil (R) for

(a) discrete data points showing relationships and (b) continuous data showing trends

The graphs in Figure 14 shows the variation of inductance with varying number of turns of the coil. It shows that that the inductance increases with increasing the number of turns of the coil.

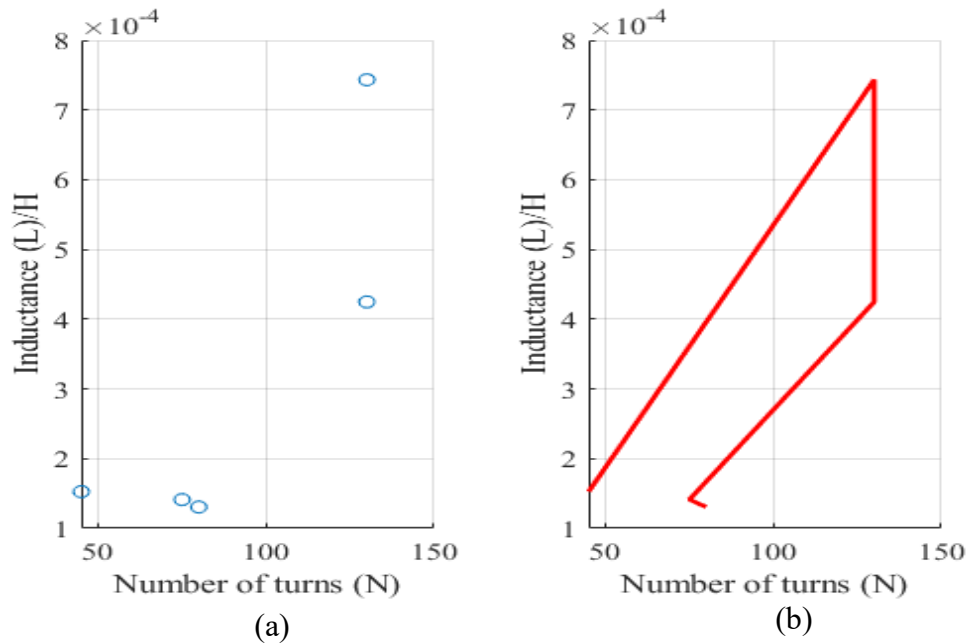


Figure 14: Graphs of inductance (L) against number of turns of coil (N) for
 (a) discrete data points showing relationships and (b) continuous data showing trends

Figure 15 is a graph that shows the variation of the inductance of a coil with both the number of turns and radii. The results indicate a positive relationship between inductance (L) and both radius (R) and number of turns (N), with the L-R curve exhibiting a gentler slope and the L-N curve showing a steeper slope. This can be attributed to the fact that the magnetic field generated by each turn (N) accumulates, producing a stronger overall field and consequently higher inductance. In contrast, an increase in radius results in a weaker magnetic field. However, the larger coil circumference still contributes to an increase in inductance. Thus, while increasing the radius raises the

inductance, its effect is less pronounced compared to the impact of increasing the number of turns.

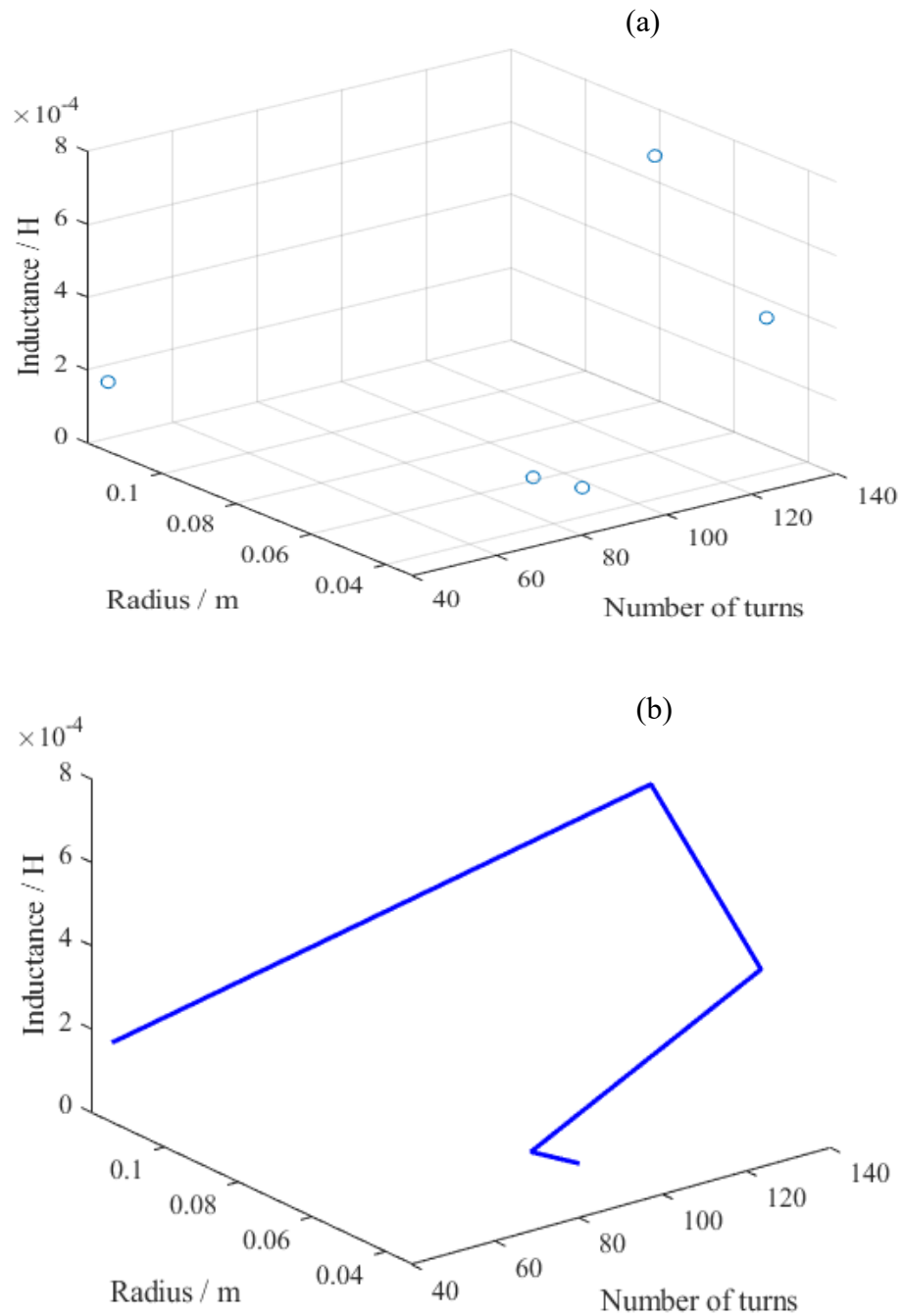


Figure 15: Three-dimensional graphs of inductance (L) against the radius of the coil (R) and number of turns of coil (N) for (a) discrete data points showing relationships and (b) continuous data showing trends

Results of the Design and Functional Testing and Validation of the Metal Detection System

The 555 IC timers, used as the pulse generator (Boxal, *et al.*, 2005), are configured as a square wave generator, creating audible pulses with the help of a capacitor between pin 2 and pin 1. The circuit includes an RLC configuration with a 47K resistor, a 2.2 μF capacitor, and the inductor, forming the metal detection component. The TE circuit pulses the coil (58 μs width, 1 kHz), waits for the magnetic field to fade, and then uses the same coil to listen for signals returning from the target environment. The coil's magnetic field is made to diminish more quickly by a 470-ohm resistor.

Electric current pulses are passed through the coiled wire which in turn broadcast a pulsating magnetic field. When the current is turned off, the magnetic field collapses, inducing a brief electrical current in nearby conducting materials. The decay time of the induced current is then analysed to determine the presence of metal objects. As the coil is air-cored, the presence of any conducting material changes the permeability of the surrounding medium. The circuit detects changes in the fundamental magnetic flux reflection, LC inductance, and occasionally the pulse induction or back emf generated in the sensing coil. The difference signal is then isolated and analysed, and if there is a difference, the alert indicator circuit will be activated.

The PI MDet employs a transient source current waveform and following termination of current in the transmit coil at time t_0 , measures the amplitude of the decaying secondary signal voltage in the receiver coil. Basic physical insight into metal detector response and related dependence on material EM properties can be obtained by investigating the response of an equivalent

lumped element circuit, including a series combination of resistance and inductance (Cross, 2008).

Results of the Design and Functional Testing and Validation of the Electromagnet (Experiment 3)

On the test of the electromagnets, both magnets pulled the weights to themselves when the voltage source was switched on. They were able to attract the different weights (as shown in Figure 16) at different distances which trend was increasing with increasing voltage. Figure 16 shows the state of the metal objects before and after the voltage was supplied to the magnet.

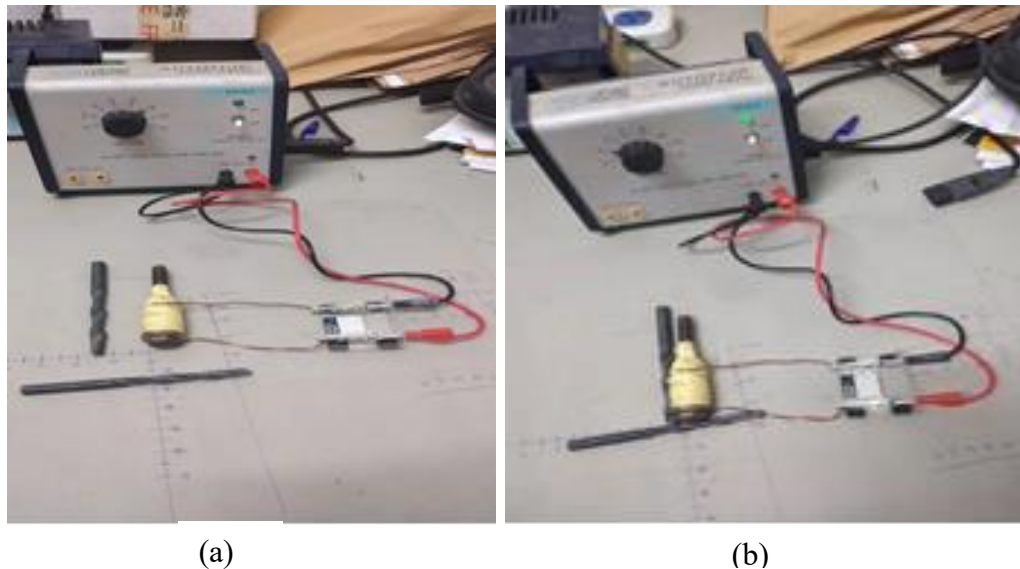


Figure 16: Pictures showing the locations of the metal objects for

(a) open circuit and (b) closed circuit

As the distance between the electromagnet and the object increases, the attraction force decreases rapidly. Therefore, a stronger magnetic field produced by higher voltage results in a greater attraction force and, consequently, a longer attraction distance. The various attraction distances with voltage increments are presented in tables 7 and 8 respectively for the 81 g and 87 g metal objects.

Table 7: Distances at which m was attracted by the electromagnet

Voltage V/V	Attraction distance for S1	Attraction distance for S2
	d11 / cm	d21 / cm
2.0	1.75	2.00
4.0	2.25	3.50
6.0	3.25	4.50
8.0	3.25	
10.0	3.25	
12.0	3.75	

Source: Researcher, 2024

Table 8: Distances at which M was attracted by the electromagnet

Voltage, V/V	Attraction distance for	Attraction distance for
	S1, d12 / cm	S2, d22 / cm
2.0	0.50	1.50
4.0	1.00	2.50
6.0	2.00	3.50
8.0	2.00	
10.0	3.00	

Source: Researcher, 2024

Figure 17 is the graphical representation of the result where distances of attraction of the electromagnets were a function of the MMF. S2 attracted at greater distances than S1 when the voltage was in the range of 2 V to 4 V. For the 81 kg mass (M1), the distances of attraction for S1 and S2 were almost the same but S2 were over two times larger than S1 for the 87 kg mass (M2). However, S1 used approximately three times the voltage supplied to S2 to attract the weight at the same distance. This implies that with a lower gauge of wire of few turns and passing a low voltage through, one can produce

approximately the same magnetising force as using a wire of higher gauge and numerous turns by passing a high voltage through it.

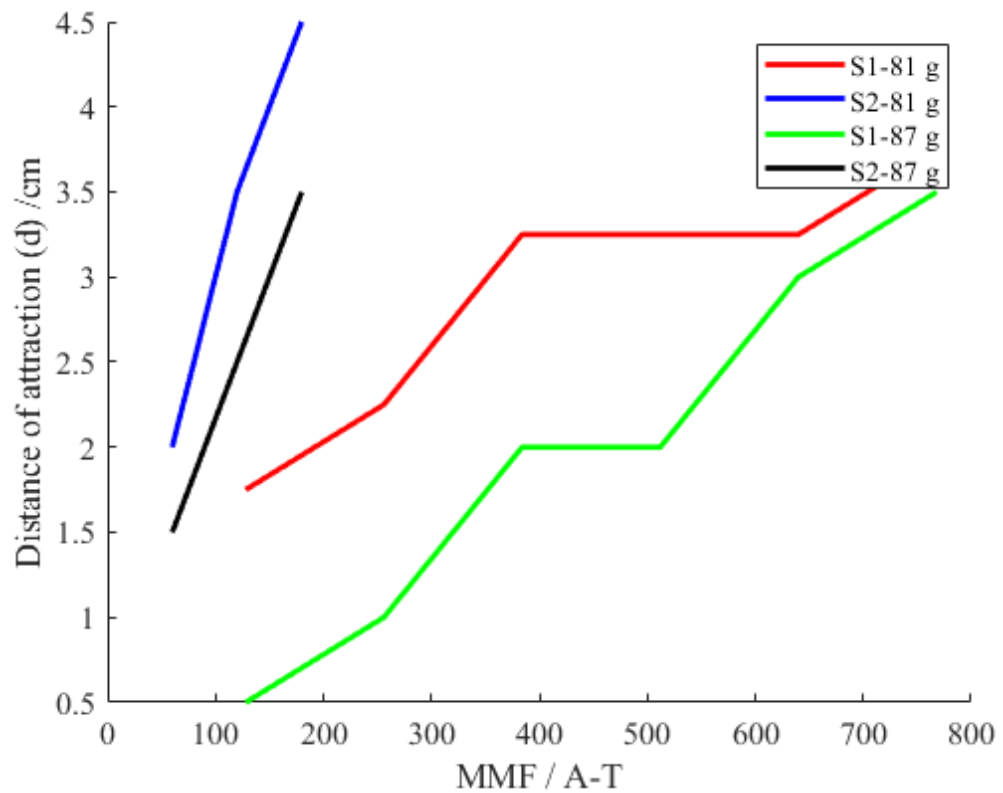


Figure 17: A graph of attraction distances for electromagnets S1 and S2 against MMF

Increasing the voltage increases the current, since the resistance is fairly constant, resulting in a stronger magnetic field and greater attraction distance. The attraction force exerted by an electromagnet on a ferromagnetic object is directly related to the strength of the magnetic field and inversely related to the distance between the magnet and the object.

It was also observed that S2 was not functioning as the voltage exceeded 4 V while S1 was still functional when the voltage was 12 V. At higher voltages and currents, the magnetic material of the core may reach saturation, where further increases in current do not significantly increase the magnetic field strength. Beyond this point, increasing the voltage may not have a substantial effect on the attraction distance but may affect the resistance of the coil and the

power dissipation. Higher voltages can lead to increased current flow, which in turn increases the power dissipated as heat in the coil.

The results generally show that designing an electromagnet involves a careful balance between the physical dimensions of the magnet, the material used, the number of turns in the coil, and the current supplied to it. It is essential to optimize the voltage to achieve the desired lifting capacity while considering factors such as power consumption, heat dissipation, and material saturation. In conclusion, variations in voltage within the saturation limits increase the magnetic field strength and, consequently, the attraction distance of electromagnets.

Results and Discussion on the Functional Prototyped InAMDeCS

Figure 18 shows the main parts of the prototyped InAMDeCS. These parts include the metal detector system, as discussed in section 4.3, the controller, and the actuator system and the power system.

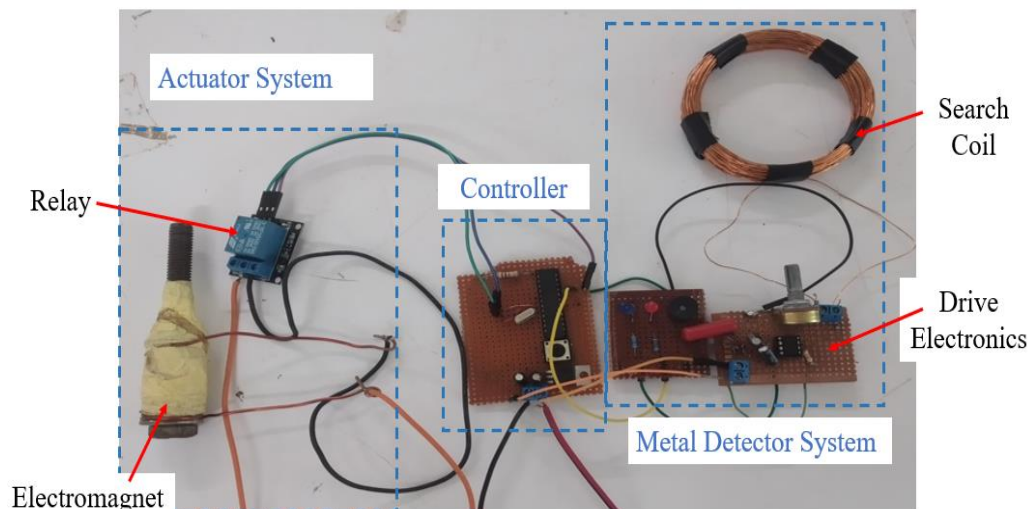


Figure 18: A picture showing the functional parts of the prototyped InAMDeCS

Discussion of the designed Controller

Most Arduino boards operate at 5 volts. However, they can often accept a range of input voltages, typically 7-12 volts, which are regulated down to 5 volts using a voltage regulator. This allows flexibility in powering the board from the solar batteries or any suitable external power supplies. The voltage regulator (LM7805) ensures that the microcontroller operates within its specified voltage range of 3.5 – 5 V. The voltage regulator also ensures that the input voltage does not exceed the maximum input voltage supported by the regulator (usually around 7-12V). Decoupling capacitors placed near the power pins (pins 7 and 8) of the microcontroller filter out noise and provide additional stability to the power supply. They help to mitigate voltage spikes and dips caused by rapid changes in current demand, ensuring smooth operation. If one plans to use the UART (serial communication), pull-up resistors (e.g., 10k Ω) may be added to the TX and RX pins (pins 2 and 3).

Discussion of the designed actuator system

The actuator system consists of a relay used to control the flow of electricity, acting as in circuit breaker and power switch. It provides electrical isolation between the control circuit and the magnetic circuit, protecting sensitive components of the microcontroller from voltage spikes and noise. The microcontroller can supply a maximum voltage of 5 V, which might not be sufficient to produce the required magnetising force. The relay, thus, supplements the circuit with a power supply from the battery directly.

Chapter Summary

Summing up, the coil configurations greatly influence the sensitivity of the MDet. On one hand, coils of smaller radii detect smaller objects better than coils of bigger radii while on the other hand, coils of bigger radii detect at longer distances than coils of smaller radii. The 555 timer IC is capable of producing a pulsating current required for the operation of the MDet. The LF of electromagnets also depends on the MMF which depends on the solenoid turns and the current flowing through the circuit. However, consideration must be given to resistive heating to obtain optimal performance.

CHAPTER FIVE

SUMMARY, CONCLUSIONS AND RECOMMENDATIONS

Overview

This study aimed to design and prototype an intelligent, solar-powered metal-debris collector capable of efficiently gathering metal waste from streets, construction sites, and other locations using metal detection technology. The model was tested in a laboratory setting, with particular emphasis on demonstrating proof-of-concept for its primary functional components: the metal detection system and the electromagnet-based pickup mechanism. The metal detector was evaluated with metals of various sizes to assess their impact on its inductance and sensitivity. Additionally, two electromagnets were tested with masses of 81 kg and 87 kg at varying distances to determine their magnetic field strength and range. Finally, the integrated control of the detection and pickup systems, managed by a custom algorithm, was successfully validated through model testing.

Summary

The prototyped MDet successfully detected metal objects that were in close proximity to the detector's search coil. Hence, the specific objective 1 was achieved. The inductance of the air-cored search coil changed when a metallic object was encountered and manifested in the form of frequency change in the LC oscillator which changes the output audio of a speaker. It was also realised in the form of voltage which was read in the Arduino IDE. It has a maximum detection range of 7 cm.

The designed electromagnet was able to attract ferrous metals in a field that extends to about 5 cm, which was also the second specific objective of the study. Though the metal detector could detect both ferrous and non-ferrous metals, only the ferrous metals could be picked by the electromagnet. This is a result of the magnetic domain of the non-ferrous not being influenced by the external magnetic field.

An Arduino board constructed from an ATmega328P microcontroller and some other electronic components was programmed with firmware which could read the change in inductance of the MDet and instruct an electromagnet to attract ferrous metals based on an indication of the presence of MD. This was specific objective three set to ensure the success of the study.

The magnet could attract metal object of mass of 87 g when it was operated with DC voltage ranging from 2 V to 12 V while the Arduino boards operates on a DC voltage ranging from 3 V to 7 V. The two components, operated on DC voltage of less than or equal to 12 V and hence can be powered by a 12 V to 19 V solar cell.

However, the major limitations lie in the coil sensitivity and range and the balance between magnetic saturation and the LF of the electromagnet.

Conclusions

In conclusion, the objectives of this work were successfully achieved through the development of an intelligent Arduino-based metal debris collector system. The prototype effectively demonstrated the detection and removal of metal debris using a controller firmware embedded with precise instructions. Key findings include:

1. The system's ability to detect and remove metal debris from roads can significantly enhance road safety, reducing the risk of accidents caused by debris, while also contributing to the socio-economic well-being of communities.
2. The prototype parts are all direct current driven. Thus, it can be powered by solar, which is relatively cheap and eco-friendly compared to traditional magnetic sweeping machines that use combustible fuel.
3. Its Arduino-based algorithm, which is an open-source programming environment, makes it highly accessible and easy to program and modify.
4. The intelligent features make it energy efficient and also it does not require skilled operators.

Although the prototype was developed under laboratory conditions, it provided valuable insights and proof-of-concept results. Its limited ability to replicate real-world conditions may restrict its immediate practical application. However, with further development, real-world training, and minor adjustments to the firmware, this system has great potential for broad implementation.

Recommendations

I recommend that stakeholders implement the findings of this research in practical ways, such as cleaning up roads, compounds, streets, and workshops. Additionally, I suggest that policymakers in the roads and transportation sectors, including organizations like the Road Safety Authority (RSA), Urban Roads Departments (URD), and the Ministry of Roads (MoR),

consider integrating these findings into existing road maintenance vehicles or investing in the development of specialised magnetic road sweeping systems.

In general, for the design of a novel MD collector like InAMDeCS, very careful coil design and high precision in the production of a search head are needed for practical application. Future focus would be on the following:

- i. Developing machine learning algorithm to characterise the contribution of ground mineralisation and other environmental factors to optimise the MDet in practical extent.
- ii. Optimisation studies for design of the MDet search coil, the electromagnet solenoid and the magnetic core of the electromagnet. PCB search coils can have a better value of certain parameters (such as thickness and inductance against area, turns and diameter) than the parameters of hand-wound search coils (Ulvr, 2018). Additionally, shaping the core to concentrate the magnetic field can further enhance its strength.
- iii. Embedding features that could be used to collect non-ferrous metals as they are being detected.

REFERENCES

- Abubakar, I. R., Maniruzzaman, K. M., Dano, U. L., AlShihri, F. S., AlShammari, M. S., S. Ahmed, S. M., Ghanem Al-Gehlani, W. A., & Alrawaf, T. I. (2022). Environmental sustainability impacts of solid waste management practices in the Global South. *International Journal of Environmental Research and Public Health*, 19(19), 12717. <http://doi.org/10.3390/ijerph191912717>
- Abusara, M. A., & Sharkh, S. M. (2013). Design and control of a grid-connected interleaved inverter. *IEEE Transactions on Power Electronics*, 28(2), 748-764. doi:10.1109/TPEL.2012.2201505
- Adedeji, K. A. & Adebisin, A. A. (2020). Design and construction of a street sweeping machine. *International Journal of Engineering, Applied Sciences and Technology*, 5(2), 626-630. doi:10.33564/ijeast.2020.v05i02.107
- Adelakun, N. O. & Omolola, S. A. (2023). Development and testing of Arduino timer socket. *WSEAS Transactions on Advances in Engineering Education*, 20, 7-23. doi:10.37394/232010.2023.20.2
- Aguirre, M. & Ibikunle, G. (2014). Determinants of renewable energy growth: A global sample analysis. *Energy Policy*, 69, 374-384. <https://doi.org/10.1016/j.enpol.2014.02.036>
- Akash, Y. (2016). Effect of Temperature on electric current, magnets and electromagnet. *Int J Adv Technol*, 7(4), 1000167. doi:10.4172//0976-4860.1000167

- Alauddin, T., Islam, M. T., & Zaman, H. U. (2016). Efficient design of metal detector equipped remote-controlled robotic vehicle. *2016 International Conference on Microelectronics, Computing and Communications (MicroCom)*, 1-5. <https://doi.org/10.1109/MicroCom.2016.7522508>
- Aleem, A., Tehsin, S., Kausar, S., & Jameel, A. (2022). Target classification of marine debris using deep learning. *Intelligent Automation & Soft Computing*, 32(1), 74-85. doi:10.32604/iasc.2022.021583
- Alghanmi, S. I., Al Sulam, F. A., El-Zayat, T. A. Alhogbi, B. G., & Salam, M. A. (2015). Acid leaching of heavy metals from contaminated soil collected from Jeddah, Saudi Arabia: Kinetics and thermodynamics studies. *International Soil and Water Conservation Research*, 3(3), 196-208. <https://doi.org/10.1016/j.iswcr.2015.08.002>
- Ali, M. M., Hossain, D., Al-Imran, Khan, S., Begum, M., & Osman, M. H. (2021). Heavy metals: Their environmental impacts and mitigation. In M. Nazal & H. Zhao (Eds.), *Heavy Metals: Their Environmental Impact and Mitigation* (2nd ed., pp. 1-12). IntechOpen. <https://dx.doi.org/10.5772/intechopen.91574>
- AlMadhoun A. S. & Al-Sdoudy, A. R. (n.d.). *Basics of electronic components*. Retrieved from <https://www.amazon.com/Basics-Electronic-Components-Comprehensive-professionally/dp/1708698388>
- Ameratunga, S, Hajar, M., & Norton, R. (2006). Road-traffic injuries: Confronting disparities to address a global-health problem. *Lancet*, 367(9521), 1533-1540. doi:10.1016/S0140-6736(06)68654-6

- Amoako-Sakyi, R. (2013). *Safety of pedestrians in Ghana with emphasis on Cape Coast Metropolis: An urban transport planning agenda*. Unpublished master's thesis, University of Cape Coast, Cape Coast, Ghana.
- Ampere-Maxwell Law* (2023, June 26). Retrieved from <https://www.electricity-magnetism.org/ampere-maxwell-law/>
- Arthur, A. (2024, January 15). 14,135 road crashes, 2,276 deaths recorded in 2023. *City News Room*. Retrieved from <https://citinewsroom.com/2024/01/14135-road-crashes-2276-deaths-recorded-in-2023/>
- Arthur, V. (2023, September 27). 1433 die, 10367 injured in road crashes this year. *Ghanian Times*. Retrieved from <https://www.ghanaiantimes.com.gh/1433-die-10367-injured-in-road-crashes-this-year/>
- Aslam, J. (2005). *Study and Comparison of On-Chip LC oscillators for energy recovery clocking* (Unpublished). Linköping University, Dept. of Electrical Engineering. Retrieved from <http://www.ep.liu.se/exjobb/isy/2005/3597/>
- Asumadu-Sarkodie, S. & Owusu, A. P. (2016). The potential and economic viability of solar photovoltaic power in Ghana. *Energy Sources, Part A: Recovery, Utilization, and Environmental Effects*, 38(5), 709-716. <https://doi.org/10.1080/15567036.2015.1122682>
- Attachie, J. C. & Amuzuvi, C. K. (2013). Renewable energy technology in Ghana: Opportunities and threats. *Research Journal of Applied Sciences, Engineering and Technology*, 6(5), 776-782

- Balchandani, C., Hatwar, R. K., Makkar, P., Shah, Y., Yelure, P., & Eirinaki, M. (2017). A deep learning framework for smart street cleaning. *2017 IEEE Third International Conference on Big Data Computing Service and Applications (BigDataService)* (pp. 112-117). Redwood City, CA, USA: IEEE. doi: 10.1109/BigDataService.2017.49
- Bécherrawy, T. (2013). *Electromagnetism: Maxwell equations, wave propagation, and emission* [e-book]. Retrieved from <https://onlinelibrary.wiley.com/doi/epdf/10.1002/9781118562215.ch8>
- Bendak, S. (2008). Inappropriate tyre characteristics and high ambient temperature: A recipe for traffic accidents. *Advances in Transport Studies, 16*(16), 61-72.
- Bernzweig, M. (2023, June 30). Understanding multi frequency metal detectors [Blog post]. Retrieved from https://www.metaldetector.com/blogs/new_blog/understanding-multi-frequency-metal-detectors.
- Bhat, A. (n.d.). Experimental Research: What it is + types of designs [Blog post]. Retrieved from <https://www.questionpro.com/blog/experimental-research/>
- Bhatia, A. B. (2020). *Electrical Fundamentals – Introduction to inductance: A PDH online course for engineers*. Retrieved from https://pdhonline.com/courses/e237/e237_new.htm
- Bies, L. (n.d.). *Pulse induction metal detector with DSP*. Retrieved from <https://www.lammertbies.nl/electronics/pi-metal-detector>

- Biomedical Engineering Department (2023). Biomedical instrumentation design [Lecture note]. Al-Mustaqbal University College. Retrieved from https://uomus.edu.iq/img/lectures21/MUCLecture_2023_123183.pdf
- Blankson, P. & Larrey, M. (2020). Injuries and their related household costs in a tertiary hospital in Ghana. *African Journal of Emergency Medicine*, 54(3), 544-549. <http://dx.doi.org/10.4314/gmj.v54i3.1>
- Boadu, S. K. (2022, August 26). *Car Accidents: Causes of Car Accidents and how to avoid them*. Retrieved from <https://priorityinsuranceghana.net/2022/08/26/car-accident-causes-of-car-accidents-and-how-to-avoid-them/>
- Bolanio, W. & Busuyi, O. (2015). The nature and challenges of street sweeping and Addo-Ekiti. *African J. Psychol Study Soc*, 17(3), 145-167.
- Borens & Boyd PLC (2023, September 19). How can debris cause an accident on the road? Retrieved from <https://www.borenandboyd.com/blog/2023/09/how-can-debris-cause-an-accident-on-the-road/>
- Boxall, J., Purvis, S., Madge, G., & Banerjee, T. (2005). *A pulse induction metal detector analogue electronic*. The Australian National University, Department of Engineering. Retrieved from <https://www.scribd.com/doc/93744520/Pulse-Induction>
- Brunelli, B., Breda, S., Scanferl, P., Calgaro, L., Marcomini, A., & Badetti, E. (2023). A methodology to assess a mobile urban street cleaning activity. *Atmospheric Pollution Research*, 14(3), 101680. <https://doi.org/10.1016/j.apr.2023.101680>

- Bruschini, C. (2002). A multidisciplinary analysis of frequency domain metal detectors for humanitarian demining (Doctoral dissertation, Vrije Universiteit Brussel). *Global CWD Repository*, 1295. Retrieved from <https://commons.lib.jmu.edu/cisr-globalcwd/1295>
- Bryakin, I., Bochkarev, I., Khramshin, V. R., & Khramshina, E. A. (2021). Developing a combined method for metal detection of buried metal objects. *Machines*, 9(5), 92. <http://doi.org/10.3390/machines9050092>
- Candy, B. (n.d.). Metal detectors basics and theory. *Minelab*. Retrieved from https://www.minelab.com/__files/f/11043/KBA_METAL_DETECTOR_BASICS_&_THEORY.pdf
- Capacitance*. (n.d.). Retrieved from <https://electricalwave.com/capacitance/>
- Caravaca, M., Abad, J. & Catalá, J. D. (2015). Biot-Savart law as a tool to calculate the matrix of inductances and the coupling coefficient of two coaxial solenoids with arbitrary cross sections. *International Journal of Electrical Engineering and Education*, 52(3), 237-247. doi:10.1177/0020720915583862
- Chand, A., Jayesh, S., & Bhasi, A. (2021). Road traffic accidents: An overview of data sources, analysis techniques and contributing factors. *Materials Today: Proceedings*, 47, 5135-5141. <https://doi.org/10.1016/j.matpr.2021.05.415>
- Charitat, T. & Graner, F. (2003). About the magnetic field of a finite wire. *European Journal of Physics*, 24, 267-270. Retrieved from <https://stacks.iop.org/EJP/24/267>

- Chen, K. & Yeh, C. (2018). Preventing tire blowout accidents: A perspective on factors affecting drivers' intention to adopt tire pressure monitoring system. *Safety*, 4(2), 16. <https://doi.org/10.3390/safety4020016>
- Choe, T. E., Wu, J., Lin, X., Kwon, K., & Park, M. (2023). HazardNet: Road debris detection by augmentation of synthetic models. *Proceedings of the IEEE/CVF Conference on Computer Vision and Pattern Recognition (CVPR) Workshops*, (pp. 161-171).
- Chukwu, V. N., Anoliefo, G. O. & Ikhajiagbe, B. (2019). Environmental impact of scrap metal industries: Examination of vertical seepage of scrap metal Effluents (heavy metals) into the aquifer A. *J. Sci. Technol. Res*, 1(2), 118-127. Retrieved from <https://www.researchgate.net/publication/343278454>
- Chukwugozi, R. P. (2016). An analysis of vehicle tyres usage and failures on the highways: Towards safe driving in Ondo, Nigeria. *Civil and Environmental Research*, 8(10), 1-6.
- Citak, H. (2020). Pulse induction metal detector: A performance application. *IEEE Transactions on Plasma Science*, 48(6), 2210-2223. doi:10.1109/TPS.2020.2996182
- Cochran, J. F. & Heinrich, B.,. (2020). *Applications of Maxwell's equations* [e-book]. Retrieved from https://www.researchgate.net/profile/Giovanni-Naldi-3/publication/2863761_Applications_of_Maxwell_Equations/links/5463a3a60cf2837efdb34300/Applications-of-Maxwell-Equations.pdf
- Coey, J. M. (2010). *Magnetism and magnetic materials*. New York, USA: Cambridge University Press.

- Coleman, A. (2014). Road Traffic Accidents in Ghana: A Public Health Concern, and a Call for Action in Ghana and the Sub-Region. *Open Journal of Preventive Medicine*, 4, 822-828.
- Conway J. T. (2001). Exact solutions for the magnetic fields of axisymmetric solenoids and current distributions. *IEEE Trans Magnet*; 37, 2977–2988.
- Corso, I. & Elettrica, I. (2012). *Tesi di Laurea Arduino programming using Matlab and Simulink*. (Università degli Studi di Udine, Italy). Retrieved from <https://www.scribd.com/document/328355985/2012-09-Tese-Mestrado-WMiani-pdf>
- Cross, G. (2008). *Soil electromagnetic properties and metal detector performance: Theory and measurement* (Contract Report No. DRDC Suffield CR 2009-062). British Columbia, Canada: Terrascan Geophysics, Canadian Centre for Mines and Technologies Defence Research & Development.
- Cuncic, A. (2024, June 24). Internal validity vs. external validity in research: What they tell us about the meaningfulness and trustworthiness of research [Blog post]. Retrieved from <https://www.verywellmind.com/internal-and-external-validity-4584479>
- D.zero² electric sweeper. (n.d.). Retrieved from <https://www.flashbattery.tech/en/portfolio/electric-street-sweeper-dulevo/>
- Dada, E. G., Hamidu, A. A., & Stephe, J. (2019). Design and implementation of underground cable fault detector. *International Journal of Science and Engineering Investigations*, 8(87), 46-52.

- Dailymag. (2023, September 14). What Is Gauss – Learn the basics and importance of Gauss in magnetism [Blog poas]. Retrieved from <https://bemagnet.com/what-is-gauss/>
- Dargin, J. (2020). Method and apparatus for removing orbital space debris from near earth orbit using the solar wind: Platform for redirecting and removing inert space material (PRRISM). *Journal of Space Safety Engineering*, 7(3), 369-375. doi:10.1016/j.jsse.2020.07.029
- David, V. E., John, Y., & Hussain, S. (2020). Rethinking sustainability: A review of Liberia's municipal solid waste management systems, status, and challenges. *Journal of Material Cycles and Waste Management*, 22, 1299–1317. <https://doi.org/10.1007/s10163>
- Davis, A. M. (2019). Energy, Forces, Fields and the Lorentz Force Formula. Retrieved from <https://arxiv.org/abs/1901.01664>
- Dehghani, S., Moore, F., Keshavarzi, B., & Hale, B. A. (2017). Health risk implications of potentially toxic metals in street dust and surface soil of Tehran, Iran. *Ecotoxicology and Environmental Safety*, 136, 92-103. doi:10.1016/j.ecoenv.2016.10.037
- Deme, D. (2019). Review on factors that cause road traffic accidents in Africa. *Journal of Architecture and Construction*, 2(3), 41-49.
- Diener, G., Weissbarth, J., Grossmann, F., & Schmidt, R. (2013). Obtaining Maxwell's equations heuristically. *American Journal of Physics*, 81(2), 129-123.

- Department of EECS. (2007). *Diodes and transistors*. (University of California, California). Retrieved from <https://inst.eecs.berkeley.edu/~ee100/su07/handouts/DiodeTransistorNotes.pdf>
- Drory, A. (2023). Motivating the Biot-Savart law. *The Physics Teacher*, 61(5), 368-370. <https://doi.org/10.1119/5.0084454>
- Edunyah, I. (2016). Causes of tyre failure on road traffic accident; A case study of Takoradi Township. *International Journal of Scientific and Research Publications*, 6(2), 30-35.
- Eeriez magnetic sweepers. (n.d.). Retrieved from <https://www.eeriez.com/NA/EN/Products/Magnetic-Separation/Magnetic-Sweepers.htm>
- Egner, F. & Trosvik, L. (2018). Electric vehicle adoption in Sweden and the impact of local policy instruments. *Energy Policy*, 121, 584-596. <https://doi.org/10.1016/j.jengpol.2018.06.040>
- Electromagnetic sweepers. (2015). Retrieved from <https://www.storchmagnetics.com/electromagnetic-sweepers/>
- Enu, P. (2014). Road traffic accidents and macroeconomic conditions in Ghana. *Absr*, 2(9), 374-393.
- Errede, S. (2015). *American wire gauge (AWG) and metric gauge wire sizes* (University of Illinois at Urbana-Champaign, Department of Physics, Illinois). Retrieved from https://hep.physics.illinois.edu/home/serrede/p436/lecture_notes/american_wire_gauge.pdf

- EVIE street sweeper*. (n.d.). Retrieved from <https://www.emobility-engineering.com/evie-street-sweeper/>
- Firdaus, A. A. Z., Vernoon, A. W. N., Syahirah, K. N., Hafis, S. M., Nurul, S., Kananfiah, A. M., ... Hidayah, A. Z.N. (2012). *Design and analysis of pulse induction underground mines detecting system*. International Conference on Functional Materials and Metallurgy, Pulau Pinang, September, 2012. Retrieved from <https://www.researchgate.net/publication/281629608>
- Fitzgerald, P. (2023). *AVR programmers I: Arduino ISP Arduino programs Arduino*. Retrieved from <https://www.hackster.io/patrick-fitzgerald2/avr-programmers-i-arduino-isp-arduino-programs-arduino-7b912f>
- FoxyPI. (2019). *FoxyPI - Arduino Nano-based pulse metal detector*. Retrieved from <https://projecthub.arduino.cc/FoxyLab/foxyapi-arduino-nano-based-pulse-metal-detector-d92e7f>
- Frempong, B. B. (2016). *Design and fabrication of voltage stabilizer using 8051 microcontroller*. Unpublished doctoral thesis, Department of, University of Cape Coast, Cape Coast, Ghana. Retrieved from <https://ir.ucc.edu.gh/xmlui/handle/123456789/6462>
- Gaille, L. (2017). *16 Advantages and Disadvantages of Experimental Research* [Blog post]. Retrieved from <https://vittana.org/16-advantages-and-disadvantages-of-experimental-research>

- Garinto, D., Syahriar A., & Budiyanto, S. (2020). A Novel Op-Amp Based LC oscillator for wireless communications. *IECON 2020 The 46th Annual Conference of the IEEE Industrial Electronics Society*, (pp. 2243-2248). Singapore. doi:10.1109/IECON43393.2020.9255128
- Gebremedhn, M. G. & Raman, P. V. (2020). Socio economic and health status of street sweepers of Mekelle city, Ethiopia. *Waste Management*, 13, 251-259. <https://doi.org/10.1016/j.wasman.2019.12.024>
- Gibson, D. (2021, April 22). *Slow punctures: the dangers and should you repair them?* Retrieved from <https://www.autoexpress.co.uk/carnews/102438/slow-punctures-should-you-repair-them-and-what-are-the-dangers>
- Goniewicz, K., Goniewicz, M., & Pawłowski, W. (2016). Road accident rates: Strategies and programmes for improving road traffic. *European Journal of Trauma and Emergency Surgery*, 42(4), 433-438. <https://doi.org/10.1007/s00068-015-0544-6>
- Gunes, S., & Sariciftci, N. S. (2008). Hybrid solar cells. *Inorganica Chimica Acta*, 361(3), 581-588. <https://doi.org/10.1016/j.ica.2007.06.042>
- Gurevich, V. (2018). *Electric relays: principles and applications* (1st ed.). Boca Raton: CRC Press. <https://doi.org/10.1201/9781315221168>
- Grant, I. S. & Phillips, W. R. (2008). *Electromagnetism* (2nd ed.). Manchester Physics, England: John Wiley & Sons Ltd. ISBN:978-0-471-92712-9
- Gyasi, E. (2022, January 25). Multi-talented young engineer creates tricycles to help curb Ghana's sanitation problems. *Ghana Environmental Issues and News*. Retrieved from <https://www.ghanaenvironment.com/sanitation-sweeping-tricycles/>

- Gyimah, N. (2023). Contributing factors to road accidents in Ghana. *Mathews Journal of Emergency Medicine*, 8(1), 48. doi:10.30654/mjem.10048
- Hayat, M. B., Ali, D., Monyake, K. C., Alagha, L., & Ahmed, N. (2019). Solar energy: A look into power generation, challenges and solar-future. *International journal of Energy Research*, 43(3), 1049-1067.
- Huang, J., Zhuo, J., & Yao, D. (2023). A method for road debris detection inside tunnel. In *2023 IEEE International Conference on Imaging Systems and Techniques (IST)* (pp. 1-6), Copenhagen, Denmark, May-October 2023. <https://doi.org/10.1109/IST59124.2023.10355665>
- Jalloul, H., Choi, J., Yesiller, N., Manheim, D., & Derrible, S. (2022). A systematic approach to identify, characterize, and prioritize the data needs for quantitative sustainable disaster debris management. *Resources, Conservation and Recycling*, 180, 106174. <https://doi.org/10.1016/j.resconrec.2022.106174>
- Jamil, S., Muktar, T., Ali, R. H., Qaiser, I., & Ahmed, B. (2022). Design and development of an electric remote-controlled road-sweeper vehicle. *Eng Proc*, 12(1), 89. <https://doi.org/10.3390/engproc2021012089>
- Jeong, H. & Ra, K. (2022). Investigations of metal pollution in road dust of steel industrial area and application of magnetic separation. *14*(2), 919. <https://doi.org/10.3390/su14020919>
- Jiles, D. (1991). *Introduction to magnetism and magnetic materials* (1st ed.). New York: Springer. doi:10.1007/978-1-4615-3868-4

- Kabir, A., Farhana, N., Akter, F., Jesmin, S., & Ali, A. (2017). Sweeping practices, perceptions and knowledge about occupational safety and health hazards of street sweepers in Dhaka city, Bangladesh: a qualitative inquiry. *International Journal Of Community Medicine And Public Health*, 2(3), 237–243. <https://doi.org/10.18203/2394-6040.ijcmph20150476>
- Khan, A., Pannase, A., Sharmagat, A., & Gohane, G. (2017). Study of multipurpose road cleaning machine. *International Research Journal of Engineering and Technology*, 4(2), 1382-1386. Retrieved from <https://irjet.net/archives/V4/IRJRT-V4|2270>
- Khan, J., Bhapkar, U., Bhat, J., Chougule, A., & Sangale, S. (2021). Design and development of smart solar powered street sweeping machine. *Mater. Today Proc.*, 46, 8663–8667. <https://doi.org/10.1016/j.matpr.2021.03.662>
- Kim, B., Han, S., & Kim, K. (2014). Planar spiral coil design for a pulse induction metal detector to improve the sensitivities. *IEEE Antennas and Wireless Propagation Letters*, 13, 1501-1504. doi:10.1109/LAWP.2014.2341591
- Klangmuang, S., Obma, J., Prathepha, K., Uthathip, N., Chaiduangri, N., & Sangiamvibool, W. (2023). The LC Oscillator circuit using capripo techniques. *Przeglad Elektrotechniczny*, 99(2), 152-155. doi:10.15199/48.2023.02.26
- Knight, R. D. (2008). *Physics for scientists and engineers: A strategic approach* (3rd ed., pp. 1096-1097). New York, NY: Pearson Education.

- Koteswaramma, N., Navya, A., Singh, P., Rajeshwari, T., & Mounika, B. (2022). Automatic street light controlling Arduino system using LDR. *International Research Journal of Modernization in Engineering Technology and Science*, 4(8), 2282-2287. doi:<https://www.doi.org/10.56726/IRJMETS29579>
- Krishnan, K. M. (2016). *Fundamentals and applications of magnetic materials* (1st ed.). New York, NY: Oxford University Press.
- Kumar, R. & Khalkho, A. N. (2016). Design and implementation of metal detector using DTMF technology. In 2016 *International Conference on Signal Processing, Communication, Power and Embedded Systems (SCOPE5)* (pp. 368-371). <https://doi.org/10.1109/SCOPE5.2016.7955853>
- Kuphaldt, T. R. (2006). *Lessons in electric circuits, volume I – DC* (5th ed.). Open Book Project Collection. Retrieved from <http://103.203.175.90:81/fdScript/RootOfEBooks/E%20BOOKS%20COLLECTION%202020%20%20DATA%202/EEE/Lessons%20In%20Electric%20Circuits%20Volume%20I%20DC%20By%20Tony%20R%20Kuphaldt.pdf>
- Liffran, F. (2008). A procedure to optimize the inductor design in boost PFC applications. *2008 13th International Power Electronics and Motion Control Conference* (pp. 409-416). Poznan, Poland. doi:10.1109/EPEPMC.2008.4635300
- Lim, M. X. & Greenside, H. (2016). The external magnetic field created by the superposition of identical parallel finite solenoids. *American Journal of Physics*, 84(8), 606–615. <https://doi.org/10.1119/1.4948603>

- Lissah, S. Y., Ayanore, M. A., Krugu, J. K., Aberese-Ako, M., & Ruitter, R. A. C. (2021). Managing urban solid waste in Ghana: Perspectives and experiences of municipal waste company managers and supervisors in an urban municipality. *Plos One*, *16*(3). doi:<https://doi.org/10.1371/journal>
- List, J. (2017, January 18). *Understanding the quartz crystal resonator*. Retrieved from Hockaday: <https://hackaday.com/2017/01/17/understanding-the-quartz-crystal-resonator/>
- Liu, B., Zhang, F., Li, D., & Yang, Y. (2014). Research on the detection of metal debris with micro inductive sensor embedded in lubricant. *Journal of Chemical and Pharmaceutical Research*, *7*(6), 2249-2254.
- Liu, B., Zhang, F., Li, D., & Yang, Y. (2014). Research on the influence of excitation frequency on the sensitivity in metal debris detection with inductor sensor. *Advances in Mechanical Engineering*, *2014*, 1-9. doi:[10.1155/2014/790615](https://doi.org/10.1155/2014/790615)
- Lupangu, C. & Bansal, R. C. (2018). A review of technical issues on the development of solar photovoltaic systems. *Renewable and Sustainable Energy Review*, *98*, 518. <https://doi.org/10.1016/j.rser.2018.09.042>
- M3EV electric 100% plug-in*. (n.d.). Retrieved from <https://globalsweeper.com/electric-street-sweepers#green-sweepers>
- Maka, A. O. M., Salem, S., & Mehmood, M. (2021). Solar photovoltaic (PV) applications in Libya: Challenges, potential, opportunities and future perspective. *Cleaner Engineering and Technology*, *5*, 100267. <https://doi.org/10.1016/j.clet.2021.100267>

- Martin, R. D., Neary, E., Renaldo, J., & Woodman, O. (n.d.). 22.3: *Ampere's law*. Retrieved from <https://phys.libretexts.org/@go/page/19535>
- Maurek, P. A., Wdowiak, A., & Anusiewicz, A. (2017). Electromagnetic interaction of metal detectors. *European Journal of Medical Technologies, 1*(14), 33-40.
- Meaney, D. (n.d.). *Oscillator design basics*. Retrieved from ECS Inc. International: <https://ecsxtal.com/store/pdf/oscillator-circuit-design-baiscs.pdf>
- Mellis, D. A. (2008, October 23). *Building an Arduino on a breadboard*. (R. Nugent, Ed.). Retrieved from <https://docs.arduino.cc/retired/hacking/hardware/building-an-arduino-on-a-breadboard/>
- Mistri, R. K., Asheer, S., Kumari, P., Toppo, M., & Singh, A. K. (2017). Cheap and efficient metal detector. *IJSART, 3*(5), 2395-1052.
- Mistry, G., Popat, K., Patel, J., Panchal, K., Ngo, H. H., Bilal, M., & Varjani, S. (2023). New outlook on hazardous pollutants in the wastewater environment: Occurrence, risk assessment and elimination by electrodeionization technologies. *Environmental research, 219*, 115112. <https://doi.org/10.1016/j.envres.2022.115112>
- Mitra, S., Chakraborty, A. J., Tareq, A. M., Emran, T. B., Nainu, F., Khusro, A., Idris, A. M., Khandaker, M. U., Osman, H., Alhumaydhi, F. A., & Simal-Ganara, J. (2022). Impact of heavy metals on the environment and human health: Novel therapeutic insights to counter the toxicity. *Journal of King Saud Univ. - Sci., 34*(3), 101865. <https://doi.org/10.1016/j.jksus.2022.101865>

- Mor, K. R. (2019). E-waste generation and management practices in Chandigarh, India and economic evaluation for sustainable recycling. *J. Clean. Prod.*, 221, 286-294. <http://doi.org/10.1016/j.jclepro.2019.02.158>
- Morgan, W. H. (1984). Forensic science assistance in investigating road accidents. *Medicine and Law*, 3(3), 297-303.
- Mousavi, S., Hosseinzadeh, A., & Golzary, A. (2023). Challenges, recent development, and opportunities of smart waste collection: A review. *Science of The Total Environment*, 866, 163925. <https://doi.org/10.1016/j.scitotenv.2023.163925>
- Mukesh, V., Manda, V., Chaitanya, M., & Mechanical, H. (2016). Design and development of simplified road cleaning machine with modified technology suitable to Indian environment. *International Journal of Engineering and Scientific Research*, 4(2), 97-124.
- Naeem, M., Shamim, S., Shahzad, H., & Khan, S. (2017). Trend analysis for enhanced road safety in Pakistan. 0-6. <http://doi.org/10.13140/RG.2.2.14777.16481>
- Nagpal, M. S. (2023, July 3). *Magnetic field due to a current through circular loop*. Retrieved from <https://classnotes.org.in/class-10/magnetic-effects-of-electric-current/magnetic-field-due-to-a-current-through-a-circular-loop/>

- Nandi, P.K., Ema, R.R., Islam, T., Jahan, S. (2020). An Automated Wireless Irrigation System by Using Moisture Sensor and DTMF Technology. In: Uddin, M.S., Bansal, J.C. (Eds) *Proceedings of International Joint Conference on Computational Intelligence. Algorithms for Intelligent Systems*. Springer, Singapore. https://doi.org/10.1007/978-981-15-3607-6_16
- Nelson, C. V. (2004). Metal detection and classification technologies. *John Hopkins Apl Technial Digest*, 25(1), 62-67.
- Nikam, S., Bhosale, D., Nigad, P., Khamkar, S., Mohite, S., & Dhumal, N.U. (2022). Magnetic roller sweeper. *Intertional Research Journal of Mordernization in Engineering, Technology and Science*, 04(06), 3443-3446.
- Olajuyigbe, A. E., Ogan, V., Adegboyega, S. A., & Fabiyi, O. (2014). Spacio-temporal analysis of road accidents in Abuja, Federal Capital Territory (FCT), Nigerial using geographical information system (GIS) techniques. *Journal of Scientific Research and Reports*, 3(12), 1665-1688. doi:10.9734/jsrr/2014/6325
- Olhoeft, G. R. (2003). Electromagnetic field and material properties in ground penetrating radar . *2nd International Workshop on Advanced GPR, 14-15 May, 2003* (pp. 144-147). Delft, The Netherlands: IEEE.
- Oliveira, M. H. & Miranda, J. A. (2000). Biot-Savart-like law in electrostatics. *European Journal of Physics*, 22(1), 31. doi: 10.1088/0143-0807/22/1/304

- OpenStax (August 22, 2016). *College Physics*. OpenStax CNX. Retrieved from https://cnx.org/contents/Ax2o07U1@9.73:HR_VN3f7@3/Introduction-to-Science-and-th
- Oppong, R. A. (2012). Statistical analysis of road accidents fatality in Ghana using Poisson regression. Unpublish master's thesis, Kwame Nkrumah University of Science and Technology, Kumasi, Ghana. Retrieved from <https://ir.knust.edu.gh/handle/123456789/4544>
- Oppong, S., Mate-Kole, C. C., Nyarko, K. & Asumeng, M. (2022). Analysis of road traffic accidents and implications for road safety: Evidence from a public transportation system in a non-Western Setting. *Ghana Social Science Journal*, 19 (1), 74–94.
- Osei-Kyei, R. & Chan, A. (2017). Implementing constraints in public-private partnership. *Journal of Facilities management*, 15(1), 90 - 106. doi: 10.1108/JFM-07-2016-0032
- Owusu, C. K. (2018). Identification of road traffic hotspots in the Cape coast Metropolis, Southern Ghana using geographical information system (GIS). *International Journal of Science and Engineering Research*, 9(10), 2106.
- Pan, T. & Zhu, Y. (2017). Getting Started with Arduino. In T. & Pan, *Designing Embedded Systems with Arduino* (pp. 3–16). Springer, Singapore. doi:10.1007/978-981-10-4418-2_1

- Patel, I. K., & Aslanov, V. S. (2020). Active debris removal using electromagnetic induction. In *Information Technologies and Nanotechnology (ITNT-2020). Proceedings of the VI International Conference and Youth School* (No. 4, pp. 42-52), Samara, Russia: Samara national research university.
- Patil, P. V., & Kambel, R. K.,. (2017). Occupational health hazards in street sweepers of Chandrapur City, Central India. *Int. J. Environ.*, 6(2), 9-18. <https://doi.org/10.3126/ije.v6i2.17358>
- Paul, C. R. (2010). *Inductance: loop and partial*. Hoboken, New Jersey, USA: John Wiley & Sons, Inc.
- Pawlak, A. M. (2017). *Sensors and actuators in mechatronics: design and applications* (1st ed.). Boca Raton, Florida, USA: CRC Press. <https://doi.org/10.1201/9781315221632>
- Pendem, S., Suresh, K., Chilakala, S., Mubeen, S., & Shabana, N. (2023). Smart shoe based on piezoelectric sensors for low power applications. In *AIP Conference Proceedings* (Vol. 2477, No. 1, pp. 030005-1 - 030005-6). AIP Publishing. <https://doi.org/10.1063/5.0125157>
- Pearson, B. J., Chen, J., & Beeson, R. C. (2018). Evaluation of storm water surface runoff and road debris as sources of water pollution. *Water, Air, & Soil Pollution*, 229, 194. <https://doi.org/10.1007/s11270-018-3793-2>
- Pickover, C. A. (2008). *Laws of Science and the great minds behind them: Archimedes to Hawkin*. New Yrok, USA: Oxford University Press, Inco.

- Pikuła, D. & Stępień, W. (2021). Effect of the degree of soil contamination with heavy metals on their mobility in the soil profile in a microplot experiment. *Agronomy*, *11*(5), 878. <https://doi.org/10.3390/agronomy11050878>
- Pine, J., King, J., Morrison, P., Morrison, P., & Mcneil, J.A. (2004). The Metal Detector and Faraday's Law. *The Physics Teacher*, *42*, 369-373. Plonus, M. A. (2020). The digital computer. *Elsevier eBooks*. doi:<https://doi.org/10.1016/b978-0-12817008-3.00008-5>
- Raja, D. (2015, May 14). *Simple metal detector circuit*. Retrieved from Circuit Digest: <https://circuitdigest.com/electronic-circuits/simple-metal-detector-circuit>
- Ravi teja, B. . Jayakrishna, G., & Bahamani, A. K. (2018). Hybrid inverter with solar battery charging. *Journal of Emerging Technologies and Innovative Research* , *5*(7), 1075-1082.
- Rerkratn, A., Petchmaneelumka, W., Kongkauropham, J., Kraisoda, K., & Kaewpoonsuk, A. (2011). FoxyPI-Arduino Nano metal detector: Pulse induction metal detector using sample and hold method. In *Proceedings of the 2011 11th International Conference on Control, Automation and Systems* (pp. 45-48).
- Sagr, M. (2020). Urban soils and road dust—civilization effects and metal pollution—a review. *Environments - MDPI*, *7*(11), 1-65. doi:[10.3390/environments7110098](https://doi.org/10.3390/environments7110098)
- Sarker, S. (2023). *Design of a differential cross-coupled power LC oscillator with ASK modulation*. Unpublish Master's thesis, Department of Electrical Engineering, Linköping University, Linköping, Sweden.

- Shahjahan, S. (2022, April 8). *Simple metal detector circuit*. Retrieved from <https://www.circuits-diy.com/simple-metal-detector-circuit/>
- Sharma, S., Jain, K. K., & Sharma, A. (2015). Solar cells: In research and applications. *Material Science and Applications*, 6(12), 1145-1155. <https://doi.org/10.4236/mas.2015.612113>
- Shojaei, A. M. (n.d.). *Use Arduino as ISP to Burn Bootloader on AVR Microcontrollers*. Retrieved from <https://electropeak.com/learn/use-arduino-as-isp-to-burn-bootloader-on-avr-microcontrollers/>
- Siddhardha, N (2024, June 6). *Understanding the fundamentals: How resistors, inductors, and capacitors work in electronic circuits*. Retrieved from <https://nandisiddhardha.medium.com/understanding-the-fundamentals-how-resistors-inductor-and-capacitors-work-in-electronic-ed0df7e0ea66>
- Shrestha, A., Karki, N., Yonjan, R., Subedi, M., & Phuyal, S. (2020). Automatic object detection and separation for industrial process automation. In *Proceedings of the 2020 IEEE International Students' Conference on Electrical, Electronics and Computer Science (SCEECS)* (pp. 1-5). IEEE. <https://doi.org/10.1109/SCEECS48394.2020.195>
- Singh, J., Sahni, M. K., Bilquees, S., Khan, S. M. S., & Haq, I. (2016). Reasons for road traffic accidents—Victims' perspective. *International Journal of Medical Science and Public Health*, 5, 814-818.
- Sommers, S. L. (2016). *Rearranging algebraic equations using electrical circuit applications: A unit plan aligned to the New York State common core learning standards* (Master's thesis, Brockport State University). Retrieved from https://digitalcommons.brockport.edu/ehd_theses/672

- Smart magnetic sweepers.* (n.d.). Retrieved from <https://www.acgair.cz/index.php/products/smart-magnetic-sweepers/>
- Street Sense Org (n.d.). *Annual Statistics : The full statistics by police MTTD.* Retrieved from <https://streetsensegh.org/index.php/publications/annual-statistics.html#>
- Strong, K. C. & Vasques, R. V. (2014). *CDOT rapid debris removal research project.* (Report CDOT-2014-9). Fort Collins, CO, USA: Colorado State University. Retrieved from <https://rosap.nsl.bts.gov/view/dot/27731>
- Stupakov, I. M., Royak, M. E., & Kondratyeva, N. S. (2016). The method for calculating magnetic field induced by current coils. *Proceedings of the 13th International Scientific-Technical Conference on Actual Problems of Electronic Instrument Engineering (APEIE)*, 2(6), 347–350. <https://doi.org/10.1109/APEIE.2016.7806485>
- Sudhan, R. H., Kumar, M. G., Prakash, A. U., Devi, S. A. R., & Sathiya, P. (2015). Arduino ATmega-328 microcontroller. *International Journal of Innovative Research in Electrical, Electronics, Instrumentation and Control Engineering*, 3(4), 27-29. doi:10.17148/IJIREEICE.2015.3406
- Sujadi, H., Bastian, A., & Tira. (2018). Design prototype detection tools of porous tree using microcontroller Arduino Uno R3 and piezoelectric sensor. *Journal of Physics: Conference Series*, 1013(1), 012163. <https://doi.org/10.1088/1742-6596/1013/1/012163>
- Suyabodha, A. (2017). A relationship between tyre pressure and rolling resistance force under different vehicle speed. *2017 International Conference on Mechanical, Aeronautical and Automotive Engineering (ICMAA 2017)*. 108, 12004. doi:10.1051/mateconf/201710812004

- Taherdoost, H. (2022). Data collection methods and tools for research: A step-by-step guide to choose data collection technique for academic and business research projects. *International Journal of Academic Research in Management*, 10 (1), 10-38.
- Tanel, Z. & Erol, M. (2008). Student's difficulties in understanding the concept of magnetic field strength, magnetic flux density and magnetization. *Lat. Am. J. Phys. Educ.* 2(3), 184-191.
- Tefft, B. C. (2016). The prevalence of motor vehicle crashes involving road debris, United States, 2011–2014. *AAA Found. Traffic Saf*, 20(5), 1-16.
- Teja, R. (2024, March 24). *Metal detector circuit*. Retrieved from <https://www.electronicshub.org/metal-detector-circuit/>
- Tetteh, E. (2020, August 11). Ghanaian innovator invents sweeping bicycle. *The Ghana Report*. Retrieved from <https://www.theghanareport.com/ghanaian-innovator-invents-sweeping-bicycle/>
- Underhill, C. A. (2016). *Solenoids, electromagnets and electromagnetic windings*. New York, USA: D. Van Nostrand Company.
- Village, B. E. (2022, February 1). *How magnetic sweepers protect your tires*. Retrieved from <https://buymagnets.com/how-magnetic-sweepers-protect-your-tires>
- Voronin, A. (2019, September 20). Homebrew pulse induction metal detector on Arduino Nano [Blog post]. Retrieved from <https://hackaday.io/project/167704-foxyypi-arduino-nano-metal-detector/details>

- Wang, Z., Lim, E. G., Wang, W., Leach, M., & Man, K. L. (2015). Design of an Arduino-based smart car. In *ISOCC 2014 - International SoC Design Conference* (pp. 175-176). Article 7087683 (ISOCC 2014 - International SoC Design Conference). Institute of Electrical and Electronics Engineers Inc.
<https://doi.org/10.1109/ISOCC.2014.7087683>
- Wunizoya, A. A. (2023, December 30). Road accidents in Ghana: Why all must be concerned. *Modern Ghana*. Retrieved from <https://www.modernghana.com/news/1282810/road-accidents-in-ghana-why-all-must-be-concerned.html>
- Xu, L., Blaauw, D., & Sylvester, D. (2021). Ultra-low power 32kHz crystal oscillators: Fundamentals and design techniques. *IEEE Open Journal of the Solid-State Circuits Society*, *1*, 79-93. doi: <https://doi.org/10.1109/OJSSCS.2021.3113889>
- Yamada, R., Shibao, M., & Kajiwara, A. (2021). Radar cross section measurement of road debris in 79 GHz-band. *IEICE Communications Express*, *10*(2), 81-86. doi:10.1587/comex.2020XBL0163
- Yang CH, Kim HK, Kim JG, & Kim S. (2020). Impact of an automated road debris removal system on traffic flow using VISSIM. *Imulation*, *96*(9), 725-735. doi:10.1177/0037549720931159
- Yim, S. & Kim, W. (2021). Rollover prevention control for autonomous electric road sweeper. *Electronics*, *10*(22), 2790. <https://doi.org/10.3390/electronics222790>

- Yousif, M. (2018). The unified force of nature: 1-The electric & magnetic forces. *IOSR Journal of Applied Physics (IOSR-JAP)*, 10(5), 57-63.
doi:10.9790/4861-1005015774
- Yousif, E. Y. (2021). Design and simulation of metal detection system. *Humanitarian and Natural Sciences Journal*, 2(8), 159-166.
doi:10.53796/hnsj2812
- Zait, A. (2018). *An introduction to Arduino UNO pinout*. Retrieved from Circuito: <https://www.circuito.io/blog/arduino-uno-pinout/>
- Zoomlion Ghana Limited. (2020). *Rise and Shine!*. Retrieved from <https://www.facebook.com/ZoomlionLtd/posts/rise-and-shine-its-going-to-be-a-good-day-weve-come-far-as-a-nation-and-we-stron/3022373434477472/>
- Zoomlion Ghana limited. (2024). *Championing Sustainability through Waste Management*. Retrieved from <https://zoomlionghana.com/>

APPENDICES

APPENDIX A

GENERAL THEORETICAL FORMULATION OF
ELECTROMAGNETICS

The underlying concepts for devices that operate on the principle of electromagnetism, such as electromagnets and metal detectors, are inductance (L) and magnetic fields (\vec{B} and \vec{M}) of various current distributions. All the sources of \vec{B} are moving charges, but \vec{B} itself interact with charges only when they move. The fundamental relationship between the fields and the force exerted on a charged particle Yousif, (2018) is the Lorentz expression Jiles, (1991). The theory of electromagnetism, based on the research of Michael Faraday and James Clerk Maxwell, is essential to contemporary technology and provides profound insights into reality. Maxwell's equations of electricity and magnetism unify various principles and laws in electromagnetism into a coherent mathematical framework, enabling the analysis and prediction of a wide range of EM phenomena.

Lorentz Force

The Lorentz force law (EM force law) is expressed as

$$\vec{F}_L = q\vec{E} + q\vec{v}\vec{B} \quad (\text{A1})$$

Where the first and second terms on the right-hand side of equation (A1) are respectively the electric force and the magnetic force. \vec{F}_L is the Lorentz force, q is the charge, \vec{E} is the electric field, \vec{v} is the velocity of the moving charge and \vec{B} is the magnetic field (Knight, 2008; Davis, 2019). Therefore, the “presence

of an electric field from the existence of one charge causes a second charge to experience a force, resulting in motion of the charge, called current, and creates a magnetic field” (Olhoeft, 2003).

Maxwell's Equations

Maxwell's equations are a set of four fundamental equations that describe how electric and magnetic fields interact and how they are generated by charges and currents (Grant & Phillips, 1990; Diener, Grossmann, & Schmidt, 2013). They are:

$$\nabla \cdot \vec{E} = \frac{\rho}{\epsilon_0} \quad (\text{A2})$$

$$\nabla \cdot \vec{B} = 0 \quad (\text{A3})$$

$$\nabla \times \vec{E} = -\frac{\partial \vec{B}}{\partial t} \quad (\text{A4})$$

$$\nabla \times \vec{B} = \mu_0 \left(\vec{J} + \epsilon_0 \frac{\partial \vec{E}}{\partial t} \right) \quad (\text{A5})$$

These four equations, along with the Lorentz force law, form the basis of classical electromagnetism.

The Laws of Electromagnetism

Gauss's Law for Electricity

The Gauss's law of electricity (first law) is represented by the divergence of the electric field

$$\oint_S \vec{D} \cdot d\vec{S} = \frac{Q_{enc}}{\epsilon_0} \quad (\text{A6})$$

Where \vec{D} is the electric flux density measures in units of C/m^2 and defined by $\vec{D} = \epsilon \vec{E}$. \vec{E} is the electric field intensity and $\epsilon = \epsilon_0 \epsilon_r$ is the permittivity and ϵ_r is the relative permittivity of the surrounding medium (Paul, 2010). Where $\oint_s \vec{D} \cdot d\vec{S}$ is the total electric flux through a closed surface, Q_{enc} is the total charge enclosed by the surface. Equations (A2) and (A6) have the same form. From (A2), the divergence of the electric field (\vec{E}) at any point in space is equal to the electric charge density (ρ) at that point divided by the permittivity of free space (ϵ_0). This law allows us to determine the electric field produced by a charge distribution by analysing its symmetry and the enclosing surfaces (Pickover, 2008).

Gauss's Law for Magnetism

This law (Gauss's second law) allows us determine the total magnetic field that passes through a given closed surface. It states that the magnetic flux through a closed surface is zero. That is,

$$\Phi_B = \oint_s \vec{B} \cdot d\vec{S} = 0 \quad (A7)$$

This law is consistent with (A3). That is, the divergence of the magnetic field (\vec{B}) at any point in space is zero, indicating that there are no magnetic monopoles. By analysing the surface integral of the components of the fields (\vec{B}) passing through a particular area of a surface (\vec{S}), the magnetic flux is defined (Pickover, 2008; Caravaca, Abad, & Catalá, 2015). The magnetic flux simply provides the measurement of the total magnetic field that passes through a given closed surface. This law implies that there are no isolated magnetic charges, and magnetic field lines are always closed loops. Gauss's second law

is often used in conjunction with Stoke's theorem and other laws such as Biot-Savart's law and Ampère's law to analyse and predict the behaviour of magnetic fields (Paul, 2010).

Stoke's theorem

Stoke's theorem allows the interchange of a line integral and surface integral. It provides that the surface integral of the curl of a vector field $\vec{\nabla} \times \vec{F}$ over an open surface area \vec{S} will give the same result as performing the line integral of \vec{F} around the contour C that encloses that open area. That is,

$$\oint_C \vec{F} \cdot d\vec{r} = \iint_S (\vec{\nabla} \times \vec{F}) \cdot d\vec{S} \quad (\text{A8})$$

where:

\oint_C is the line integral around the closed contour C and $d\vec{r}$ is an infinitesimal vector displacement along C ,

\iint_S is the surface integral over the surface S and $d\vec{S}$ is an infinitesimal vector area element of the surface S .

Faraday's and Lenz's Laws of electromagnetic induction

Faraday's law states that the voltage induced in an electrical circuit depends on the rate of change of magnetic flux linking the circuit while Lenz's law states that the direction of the induced voltage is opposite to the flux change that caused it. The two laws together form Neumann's induction law (Bécherrawy, 2013, pp 233-245). This law describes how a changing magnetic field induces EMF in a circuit, it is consistent with Maxwell's equation (A4) expressed in integral form as:

$$\oint \vec{E} \cdot d\vec{l} = -\frac{d}{dt} \iint \vec{B} \cdot d\vec{A} \quad (\text{A9})$$

This equation quantifies how a changing magnetic flux through a surface induces a curling electric field around that surface.

Ampère's Law

This law describes the relationship between magnetic fields and electric currents (Drory, 2023; Caravaca *et al.*, 2015; Pickover, 2008). Christian Ørsted discovered in 1819, leading to the formation of Oersted's law in 1820, that a magnetic field can be created around a wire when constant electric current flows through it. Reading about Oersted's discovery of the effect of an electric current on a compass needle, Ampere deduced that a magnetic field is produced by electrical charge in motion and in an electrical circuit the field depends on the shape of the circuit (i.e. the conduction path) and the current carried. By assuming that each circuit is made up of an infinite number of current elements each contributing to the field, and by summing or integrating these contributions at a point to determine the field \vec{B} .

The original Ampère's Law is modified by the addition of the displacement current term to become the Ampère-Maxwell Law which is as:

$$\oint_C \vec{B} \cdot d\vec{l} = \mu_0 \iint_S \vec{J} \cdot d\vec{A} + \mu_0 \epsilon_0 \frac{d}{dt} \iint_S \vec{E} \cdot d\vec{A} \quad (\text{A10})$$

\vec{J} is the current density and $\mu_0 \epsilon_0 \frac{d}{dt} \iint_S \vec{E} \cdot d\vec{A}$ is the displacement current added to make it consistent with the continuity equation for the electric charge (Ampere-Maxwell Law, 2023).

Biot-Savart law

The Biot-Savart Law (BSL) is fundamental law of electromagnetism that allows us to calculate the \vec{H} created by an electrical current. The BSL, built upon the fact that a changing electric field and electric current create a magnetic field and vice versa (Tanel & Erol, 2008), is based on experimental observation rather than a theoretical prediction. Based on an experiment in 1820 by Jean-Baptiste Biot and Felix Savart, the quantitative relationship between the magnetic field and the constant current producing it was discovered. This relationship is consistent with both Ampere's circuit law and Gauss's law of magnetism (Martin *et al.*, n.d.).

$$\vec{B}(r) = \frac{\mu_0}{4\pi} \oint_C \frac{Id\vec{l} \times (r - r')}{|r - r'|^3} \quad (\text{A11})$$

It gives us the field contribution generated by a current flowing in an elementary length of the conductor in its usual form (Oliveira, M. H. & Miranda, J. A. 2000; Jiles, 1991). According to OpenStax (2016), the Ampere's and BSL provide equivalent description of the magnetic field. Both laws apply when the current distribution is steady. The Ampere's law often simplifies the calculation of magnetic field by exploiting the symmetry of current distributions for systems with high degree of symmetry (Martin, R. D., Neary, E., Renaldo, J., & Woodman, O., n.d.). (such as straight wires, solenoids or toroid) while BSL provides more general approach for arbitrary current distributions.

Magnetic fields

A magnetic field is created when there is an energy shift in a certain volume of space, along with an energy gradient. This creates a force that can be measured by observing the acceleration of an electric charge travelling through

the field. Magnetic force field, a region within which a magnet's force can be experienced (Underhill, 2016), is usually visualised by closed loops of field lines originating from the conventional north pole (N) and ending at the conventional south pole (S). Magnetic fields possess both magnitude and direction. The magnetic field's relative intensity is shown by the proximity of field lines; closer lines indicate a stronger magnetic field, and vice versa. The field pattern of a bar magnet is shown in Figure A1 below.

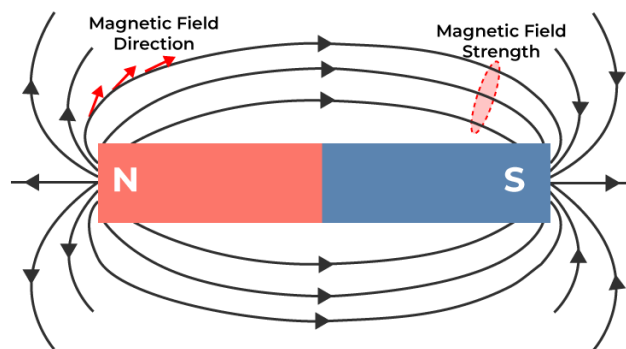


Figure A1: Magnetic field lines pattern of a permanent bar magnet

(Dailymag, 2023)

Ørsted's Law and Fleming's right-hand rule

Ørsted opined that the right-hand rule may be used to identify the direction, as in the figure below and the Hall's probe can be used to measure the magnitude Yousif (2018). Fleming's investigation leading to the development of the Right-Hand Rule (RHR) holds true for any current segment: point the thumb in the direction of the current, and the fingers will curl in the direction of the magnetic field loops it creates. Oersted discovered that the field forms circular loops around a long, straight wire Yousif (2018).

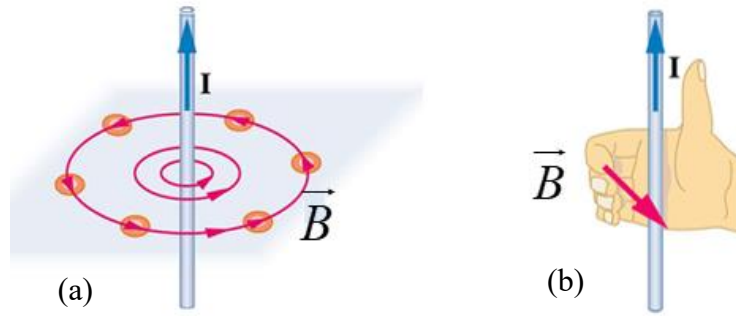


Figure A2: Magnetic field configuration of a current-carrying straight conductor
 (a) Field lines pattern; (b) field direction determined using the RHR
 (OpenStax, 2016).

The magnetic field vectors

The fundamental magnetic field vectors are the magnetic field intensity \vec{H} , and the magnetic flux density \vec{B} . Magnetic field intensity, also referred to as magnetic field strength, is the measure of the magnetising force of a magnet in units of A/m. Magnetic flux density is the amount of flux passing an area per unit area in units of Wb/m². Ampere theorem and BSL are common tools for quantifying magnetic fields created by currents (Charitat, T. & Graner, F., 2003). According to Ampere's law, a medium's magnetic induction (magnetic flux density), \vec{B} , is the medium's reaction when a current generates a magnetic field \vec{H} in it.

The concepts of \vec{H} , \vec{B} , and magnetisation (\vec{M}) are considered to be essential within the fundamental concepts of magnetism (Tanel & Erol, 2008).

These field vectors are related by

$$\vec{B} = \mu_0(\vec{H} + \vec{M}) \quad (\text{A12})$$

Where μ_0 is the permeability of free space and \vec{M} is the magnetisation produced by the external field nearby. μ_0 has a value of $4\pi \times 10^{-7} \text{ H / m}$ and \vec{M} is defined as

$$\vec{M} = \varepsilon_0 \frac{d\Phi_E}{dt} \quad (\text{A13})$$

In equation (3), $\varepsilon_0 = \frac{1}{\mu_0 c^2}$ is the permittivity of free space and Φ_E is the electric flux through a surface \vec{S} at any time, t . $c = 3 \times 10^8 \text{ m / s}$ is the speed of light Hence the magnetic field is defined as

$$\vec{B} = \mu_0 (\vec{H} + \varepsilon_0 \frac{d\Phi_E}{dt}) \quad (\text{A14})$$

For solenoids and coils, there is no changing electric field inside, thus, the second term of equation (4) is zero (Ampere-Maxwell Law, 2023). That is; for a simple, linear, homogeneous and isotropic medium; the electric flux is constant; thus, $\frac{d\Phi_E}{dt} = 0$. The fundamental magnetic field vectors are \vec{H} and \vec{B} (Dargin, 2020) which relate to each other by

$$\vec{B} = \mu \vec{H} \quad (\text{A15})$$

Where μ is the permeability of the medium. μ relates with the relative permeability of the materials of the medium μ_r and the permeability of free space, μ_0 (essentially air) as $\mu = \mu_r \mu_0$.

Electromagnetic properties of materials

The Ampere-Maxwell's law describes how a changing electric field can generate a magnetic field, which is fundamental for the principle of EM

induction (Tanel & Erol, 2008) and other magnetic properties of magnetic materials and circuits (Cochran & Heinrich, 2020). According to (Olhoeft, 2003), magnetic (and electrical) properties of materials is their ability to transport charge and store energy. “Electrical and magnetic properties are described by complex quantities, in which the real part describes storage and the imaginary part describes loss; the imaginary part is zero only in free space” (Olhoeft, 2003).

Magnetism permeability

All media will respond to the change in magnetic flux with some unique induction. The permeability of the medium (μ) is a property that relate the magnetic induction and the magnetic field. Dielectrics and metals that are not magnetisable (iron, steel and nickel) have $\mu_r = 1$ and are said to be linear and isotropic while magnetisable materials (copper, aluminium and brass) are nonlinear and have $\mu_r > 1$. Ferromagnetic materials undergo spontaneous magnetisation, which is usually associated with hysteresis, according to a study by James Ewing (Coey, 2010). The field vectors \vec{B} and \vec{H} for materials that are not linear with magnetic fields are related by the hysteresis loop (Dargin, 2020) shown in figure A3 below.

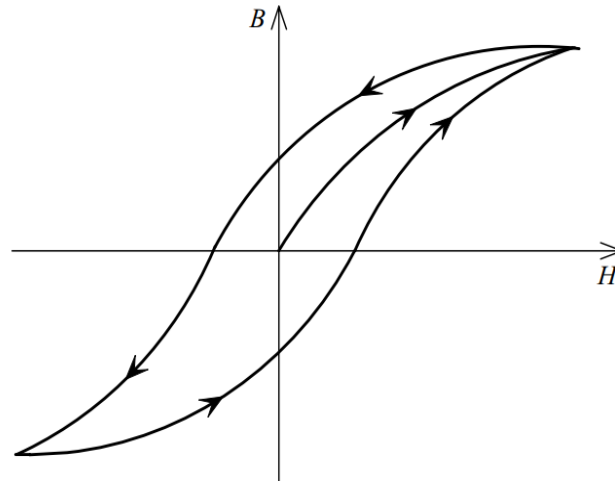


Figure A3: Hysteresis curve for non-linear magnetic media (Paul, 2010)

The slope of the curve $\frac{\Delta \vec{B}}{\Delta \vec{H}} = \Delta \mu$ gives an instantaneous change in magnetic permeability. A useful information from the loop is an irreversible nonlinear response of magnetisation to an imposed magnetic field \vec{H} . The hysteresis loop is central to technical magnetism as it combines information on an intrinsic magnetic property, the spontaneous magnetisation, and two extrinsic properties (the remanence and coercivity). This information depends on a host of factors including sample shape, surface roughness, microscopic defects, thermal history, and the rate at which the field is swept (Coey, 2010).

Inductance and magnetic induction

Inductance is the characteristic of an electrical circuit that opposes the starting, stopping, or a change in value of current (Bhatia, 2020). The Faraday's can be stated as

$$V_L = -L \frac{d\Phi_B}{dt} \quad (\text{A16})$$

Where V_L is the induced voltage in volts, $\frac{d\Phi_B}{dt}$ is the rate of change of Φ_B ,

and L is the inductance of the coil, measured in Henry (H) (Pickover, 2008). A

henry is the inductance needed in an inductor to produce one volt when there is a one ampere per second change in current. Since the magnetic induction relates to the flux as

$$\Phi_B = \vec{B}A \quad (\text{A17})$$

the inductance equation can be written as

$$V_L = -LA \frac{d\vec{B}}{dt} \quad (\text{A18})$$

According to Dargin (2020), inductance is intimately related to a closed loop of DC which produces magnetic flux through the surface surrounded by the current loop. Thus, the self-inductance of a loop is the ratio of the total flux penetrating the loop and the current that produces it (Paul, 2010).

$$L = N \cdot \frac{\Phi_B}{I} \quad (\text{A19})$$

APPENDIX B

MAGNETIC FIELD OF CURRENT ELEMENTS

The term “current element” a vector quantity that describes a current carrying segment. The BSL describes the field density while the Ampere’s law describes the field intensity.

The magnetic flux density

For an electrical conductor carrying a constant current I ampere, according to the Biot–Savart law (BSL), the current flowing through the conductor is what creates the magnetic field that is created nearby (Stupakov *et al.*, 2016; Caravaca *et al.*, 2015; Pickover, 2008). Considering the current carrying wire I in a specific direction as shown in figure B1 below.

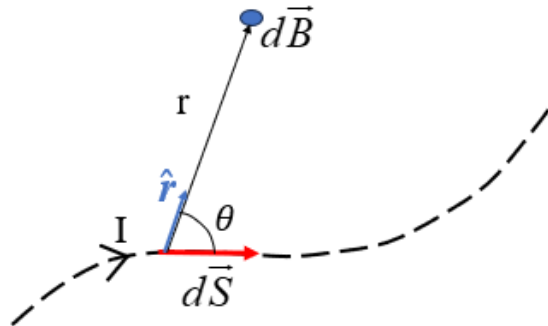


Figure B1: Magnetic field produced at a vector distance r by a current element $I d\vec{S}$

The direction of the element is along that of the current so that it forms a vector $d\vec{S}$. That is, $I \times \vec{S} = I d\vec{S} \sin \beta = I d\vec{S}$, only when β (the angle between I and $d\vec{S}$) is zero.

$$|d\vec{B}| = \frac{\mu_0}{4\pi} \cdot \frac{I d\vec{S} \times \hat{r}}{r^2} \quad (\text{B1})$$

Where r is the vector distance of the position vector \hat{r} of the point drawn from the current element ($d\vec{S}$). In reality, current element is part of a complete circuit, and only the total field due to the entire circuit can be observed. The total field is, thus, obtained by integrating along the wire as in equation (B2) below. Evaluating the integral gives the total field as

$$\begin{aligned}\vec{B} &= \frac{\mu_0 I}{4\pi} \int \frac{d\vec{S} \times \hat{r}}{r^2} \\ &= \mu_0 \frac{I}{2\pi r}\end{aligned}\quad (\text{B2})$$

The magnetic field intensity

Ampere's law allows the direct solution of the magnetic field of current without evaluating the integral (Paul, 2010). Consider the closed contour in Figure B3 below, in which \vec{H} is tangent to the C at every point on it and is constant at all points along the contour.

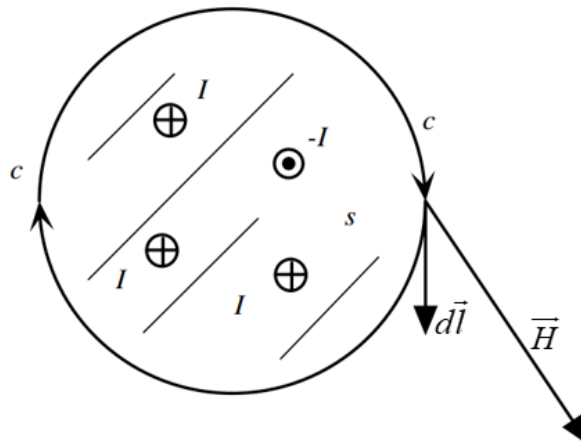


Figure B2: Diagram used to establish Ampere's Law (Paul, 2010)

If $\oint_C d\vec{l}$ is the total length of the contour then according to Ampere's law,

$$\vec{H} \oint_C d\vec{l} = I_{enc} \quad (\text{B3})$$

Consider an infinite line of current as in figure B3, where the \vec{H} vector is in the circumferential direction (in a cylindrical coordinate system) about the wire axis. \vec{H} is also constant around the contour because the current is spread uniformly throughout the wire cross-section and symmetrically about the wire axis.

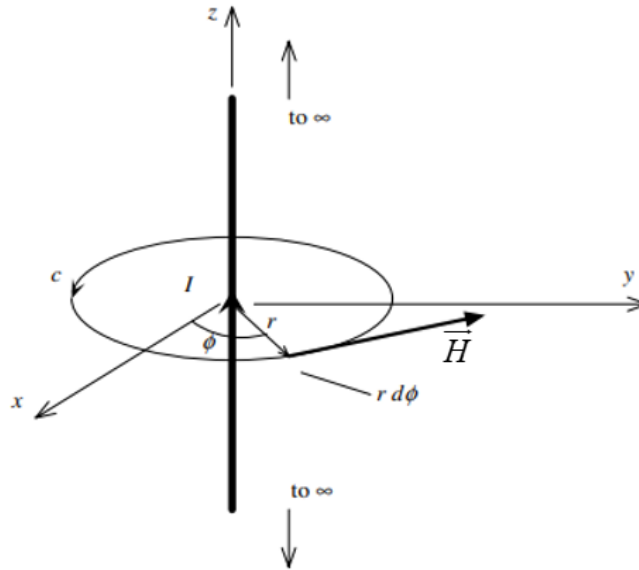


Figure B3: \vec{H} field configuration of an indefinitely long line of current

(Paul, 2010)

Provided that \vec{H} is tangent at all points on C and its magnitude is constant at all points on C that are a distance r from the current, the \vec{H} field is given as (Paul, 2010)

$$\vec{H} = \frac{I}{2\pi r} a_\phi \quad (\text{B4})$$

for the radius of the wire less than the radius of the loop. Since is constant everywhere on C , the field intensity vector becomes

$$\vec{H} = \frac{I}{2\pi r} \quad (\text{B5})$$

APPENDIX C

MAGNETIC FIELDS OF COILS

Magnetic field vectors of a current loop

When a wire is formed into a loop, the property of the magnetic induction increases (Bhatia, 2020) since each small section of current-carrying wire contributes to the magnetic field lines Nagpal, (2023). These fields' strengths are directly proportional to the amount of current passing through the wire and the number of loops but are inversely related to the wire's distance from the observer Conway, (2001). The magnetic field strength inside the loop is relatively uniform, with the highest strength at the centre of the loop and decreasing as you move away from the centre. Planar loops have magnetic field lines perpendicular to the loop's surface (OpenStax, 2016) as in Figure C1.

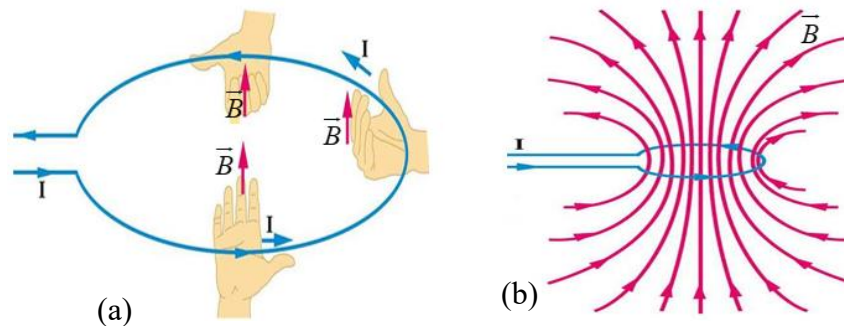


Figure C1: Configuration of \vec{B} of a current-carrying circular-loop
 (a) Direction of \vec{B} using the RHR; (b) field lines pattern
 (OpenStax, 2016)

As in Figure C2, the concentric circles denoting the magnetic field at each location along a current-carrying circular loop would enlarge as we move away from the wire, and the arcs of these huge circles would appear as straight lines at the loop's centre (OpenStax, 2016; Shaalam, n.d.).

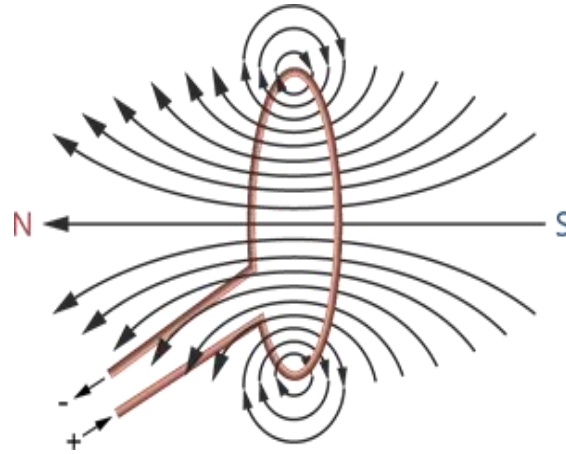


Figure C2: Magnetic field pattern of a coil (Nagpal, 2023)

Choosing a circular path of radius r centred at the centre of the coil to which the magnetic field is tangential. Thus, the dot product $\vec{B} \cdot d\vec{l}$ in Ampere's law simplifies to $\Phi_B \cdot dl$, where dl is the infinitesimal element of length along the circular path. The integral of dl along a circle of radius r is simply the circumference of the circle, $2\pi r$. Since the flux, Φ_B , is uniform along the circular path we can write

$$\frac{\Phi_B}{\mu_0} \int_0^{2\pi r} dl = I_{enc} \quad (C1)$$

$$\Phi_B (2\pi r) = \mu_0 I_{enc} \quad (C2)$$

Which, for our chosen circular path is the circumference of the coil of radius R , $r = R$. Equation (C2) then becomes

$$\Phi_B \cdot (2\pi R) = \mu_0 I_{enc} \quad (C3)$$

For a flat coil of radius R and of N turns carrying current I . The total charge enclosed I_{enc} by the circular path is given by

$$I_{enc} = N \cdot I \quad (C4)$$

Then substituting equation (C4) into (C3) and expressing it in terms of Φ_B^{coil} , we get

$$\Phi_B^{coil} = \frac{\mu_0}{2\pi R} \cdot N \cdot I \quad (C5)$$

Where Φ_B^{coil} is the magnetic flux of a plana, flat, circular coil, N being the number of turns of the wire and I , the current producing the flux.

For a coil of N loops, effective self-inductance is given as

$$L = N \frac{\vec{B}}{I} \quad (C6)$$

Now, we make the substitutions $\Phi_B^{coil} = \vec{B} \cdot A$ and $A = \pi R^2$ into equation (C6) to obtain

$$\begin{aligned} L &= \frac{N}{I} \cdot \left[\frac{\mu_0}{2\pi R} \cdot N \cdot I \right] \cdot [\pi R^2] \\ &= \mu_0 \frac{N^2 R}{2} \end{aligned} \quad (C7)$$

Equation (C7) is thus the formula for calculating the self-inductance of a flat circular coil of radius R and N turns of coil.

APPENDIX D

MAGNETIC FIELDS OF SOLENOIDS

Solenoids typically have a stronger and more uniform magnetic field along their axis compared to planar loops, making them more suitable for applications requiring a strong and consistent magnetic field (Lim & Greenside, 2016). Solenoids are used in various applications such as electromagnets, where the controlled magnetic field is utilised for tasks like picking up metallic objects and actuators in devices like valves and relays (Pawlak, 2017). A solenoid is typically a tightly wound coil of, often cylindrical in shape, with the axis of the coil defining its orientation. The magnetic field strength inside the solenoid is relatively uniform along its axis and stronger inside the coil than outside (Krishnan, 2016). Outside the solenoid, the field lines resemble those of a bar magnet (OpenStax, 2016).

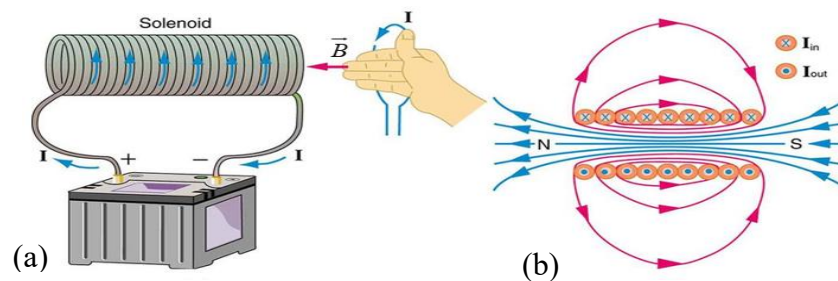


Figure D1: Magnetic field configuration for a solenoid. (a) \vec{B} direction with the RHR; (b) \vec{B} pattern of a solenoid (OpenStax, 2016)

$$\oint \vec{B} \cdot d\vec{l} = \mu_0 \cdot I_{enc} \quad (D1)$$

Since the magnetic field inside a solenoid is approximately uniform and parallel to the axis of the solenoid, the dot product simplifies to $\vec{B} \cdot d\vec{l}$ and the integration is along the solenoid length l as

$$\vec{B} \int_l dl = \mu_0 \cdot I_{enc} \quad (D2)$$

$$\vec{B} \cdot l = \mu_0 \cdot I_{enc} \quad (D3)$$

Consider the solenoid, in figure D2; with l being the length of the solenoid (length of flux path) and N being the number of loops, the total current enclosed is given by equation (D4) and the magnetic field by equation (D5).

$$I_{enc} = N \cdot I \quad (D4)$$

$$\vec{B} = \frac{\mu_0 \cdot N \cdot I}{l} \quad (D5)$$

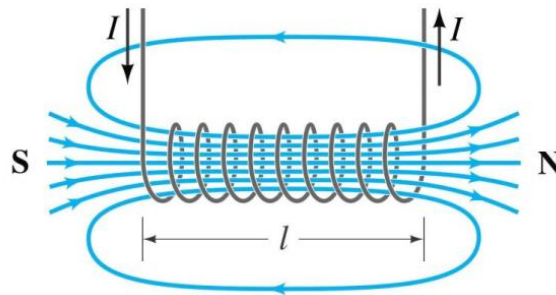


Figure D2: A diagram used to derive B of a solenoid (AlMadhoun & Al-Sdoudy, n.d.)

But

$$\Phi_B^{solenoid} = \vec{B}_{solenoid} \cdot A \quad (D6)$$

Where $\Phi_B^{solenoid}$ is the magnetic flux and A is the cross-sectional area of the solenoid. The inductance thus becomes

$$\begin{aligned} L_{solenoid} &= \mu_r N \frac{\Phi_B^{solenoid}}{I} \\ &= \frac{\mu_r N}{I} \cdot \left[\mu_0 \cdot \frac{N \cdot I}{l} \right] \cdot A \\ &= \mu_r \mu_0 \cdot \frac{N^2 A}{l} \end{aligned} \quad (D7)$$

APPENDIX E

EXPERIMENT 1

EXPERIMENTAL VALIDATION OF THE INDUCTANCE OF A SEARCH
COIL EQUATION

The determination of Inductance of a Search Coil using the Cobra3.

The inductance is given by $L = \mu_0 \frac{N^2 R}{2}$, where L is the inductance (in H), μ_0 is the permeability of free space (with value $4\pi \times 10^{-7}$ T.m/A), N is the number of turns of the wire of the coil, and R is the radius of the circular coil.

$$\mu_0 = 4 * \pi * 10^{(-7)}; R = 10 * 10^{-2}; N = 600;$$

$$L = \mu_0 * (N^2 * R) / 2$$

$L =$

$$0.022619467105847$$

Experiment Cobra3

$$\phi = \frac{\Delta t / s}{T / s} \times 360^\circ \quad (\text{E1})$$

$$T = \frac{1}{f} / s \quad (\text{E2})$$

Regression analysis

$$\tan \phi = \frac{2\pi L}{R} f + c \quad (\text{E3})$$

$$\tan \phi = mf + c \quad (\text{E4})$$

Comparing equations (E3) and (E4), equation (E5) can be obtained and then rearranging equation (E5) we have (E6).

$$m = \frac{2\pi L}{R} \quad (\text{E5})$$

$$L = \frac{mR}{2\pi} \quad (\text{E6})$$

```

% Independent variables

%.....

f = [1000,1500,2000,2500,3000,3500,4000,4500,5000]; %frequency in hertz

format long

T = 1./f; %period in seconds

d_t=[0.036,0.036,0.034,0.034,0.034,0.034,0.034,0.032,0.032]; % phase sift
in milliseconds

d_t=d_t.*10^(-3); phi=(d_t./T).*360; % phase angle in degrees

tan_phi=tand(phi);

% Table of results

Results=table(f,tan_phi)

```

Results = 9×2 table

	Var1	Var2
1	1000	0.230132967301454
2	1500	0.352940492884013
3	2000	0.455304760479049
4	2500	0.591398351399471
5	3000	0.745920171791799
6	3500	0.927307768331003
7	4000	1.148747706034449
8	4500	1.272600466963455
9	5000	1.575747859968651

```

%Plotting of data

```

```

%.....

scatter(f,tan_phi,'r*')

title('Scater Plot of Tangent of Phase Angle Against Frequency')

```

```
xlabel('Frequency /Hz'), ylabel('tan(Phase)'), grid on
hold on
%%%%%% Linear Regression %%%%%
plotregression(f,tan_phi,'Regression'), hold on
hold off
mdl=fitlm(f,tan_phi),
```

mdl =

Linear regression model:

$$y \sim 1 + x1$$

Estimated Coefficients:

	Estimate	SE	tStat	pValue
(Intercept)	-0.175301197300129			0.055205930709982
	3.17540516110582	0.0155900471056597		
x1	0.000328807826698315			1.69032951268627e-05
	19.4522916526361	2.3670552873584e-07		

Number of observations: 9, Error degrees of freedom: 7

Root Mean Squared Error: 0.0655

R-squared: 0.982, Adjusted R-Squared: 0.979

F-statistic vs. constant model: 378, p-value = 2.37e-07

```
plot(mdl),
title('Linear Regression of Tangent of Phase Angle on Frequency')
xlabel('Frequency /Hz'), ylabel('tan(phi)'), grid on
intercept=mdl.Coefficients.Estimate(1)
slope=mdl.Coefficients.Estimate(2)
```

```
% Calculation of Inductance
L=(slope*47)/2*pi
```

L =
0.024275035940759

CONTROL EXPERIMENT FOR DETERMINING THE INDUCTANCE OF A COIL

Inductance of coil = 16 mH, Coil length = 6 cm, Number of turns = 600

```
% Independent variables
%.....

f = [1000,2000,3000,4000,5000]; %frequency in herts
format long
T = 1./f; %period in seconds
%----- Control Experiment (L=15mH) -----%
d_tc=[0.010,0.095,0.064,0.054,0.047]; % phase sift in milliseconds
d_tc=d_tc.*10e-3;
phic=(d_tc./T).*360; % phase angle in degrees
tan_phic=tand(phic); %phi in degrees

% Table of results
%.....

Results=table(f, T,tan_phic')
```

Results = 5×3 table

	Var1	Var2	Var3
1	1000	1.0000000000000000e-03	0.726542528005361
2	2000	5.0000000000000000e-04	-0.726542528005361
3	3000	3.3333333333333333e-04	-0.549754652192769

	Var1	Var2	Var3
4	4000	2.5000000000000000e-04	1.575747859968653
5	5000	2.0000000000000000e-04	-1.376381920471179

```

%Plotting of data

%.....

scatter(f,tan_phic,'r+')

title('Scater Plot of Tangent of Phase Angle Against Frequency')

xlabel('Frequency /Hz'), ylabel('tan(Phase)'), grid on

hold on

%%%%%% Linear Regression %%%%%

plotregression(f,tan_phic,'Regression'), grid on

hold off

mdl=fitlm(f,tan_phic),
    
```

mdl =

Linear regression model:

$$y \sim 1 + x1$$

Estimated Coefficients:

Estimate	SE	tStat	pValue
(Intercept)	0.500989810154661		1.4003933625719
0.357749346394048	0.744220138570269		

```

x1          -0.000190355850897907    0.000422234485686829    -
0.450829710387733    0.682703677428686

```

Number of observations: 5, Error degrees of freedom: 3

Root Mean Squared Error: 1.34

R-squared: 0.0635, Adjusted R-Squared: -0.249

F-statistic vs. constant model: 0.203, p-value = 0.683

```

plot mdl,
title('Linear Regression of Tangent of Phase Angle on Frequency')
xlabel('Frequency /Hz'), ylabel('tan(phi)'), grid on
intercept=mdl.Coefficients.Estimate(1)
slope=mdl.Coefficients.Estimate(2)
% Calculation of Inductance
L=(abs(slope)*47.02)/2*pi % Inductance in henries (H)

```

L =

```
0.014059462960022
```

```
L_mH = L*1000 % inductance in millihenries (mH)
```

L_mH =

```
14.059462960021888
```

APPENDIX F

ANALYSIS OF THE VARIATION OF INDUCTANCE WITH NUMBER
OF TURNS AND RADIUS OF COIL IN MATLAB

```

% MATLAB Script for the Analysis of th Inductance (L) with Varying Radii
(R) and Number of Turns (N)

clc; clear; figure;

mu_0 = 4*pi*10^-7; % permeability of free space

r1=3.25*10^-2; r2=4*10^-2; r3=4*10^-2; r4=7*10^-2; r5=12*10^-2;

N1=80;    N2=75;    N3=130;    N4=130;    N5=45;

R=[r1, r2, r3, r4, r5];    N=[N1, N2, N3, N4, N5];

L=mu_0*N.^2.*R./2;

%.....

L1=mu_0*N1^2*r1/2; L2=mu_0*N2^2*r2/2; L3=mu_0*N3^2*r3/2;
L4=mu_0*N4^2*r4/2; L5=mu_0*N5^2*r5/2; Ls = [L1, L2, L3, L4, L5];

table(R',N',Ls');

%.....

figure,

tiledlayout(1,2)

nexttile

scatter(R,L)

set(gca, 'Box','off','FontName','Times New Roman','FontSize',12);

xlabel('Radius (R) / m'),

ylabel('Inductance (L) / H'), grid

nexttile

plot(R,L,'-b','linewidth',2),

```

```

set(gca, 'Box','off','FontName','Times New Roman','FontSize',12);
ylabel('Inductance (L)/H'), xlabel('Radius (R)/ m'), grid on,
%.....

figure,
tiledlayout(1,2)
nexttile
scatter(N,L)
%title('A plot of N againts L'),
set(gca, 'Box','off','FontName','Times New Roman','FontSize',12);
xlabel('Number of turns (N)'), ylabel('Inductance (L)/H'), grid
nexttile
plot(N,L,'-r','linewidth',2),
set(gca, 'Box','off','FontName','Times New Roman','FontSize',12);
ylabel('Inductance (L)/H'), xlabel('Number of turns (N)'), grid
figure
Ls = [L1, L2, L3, L4, L5];
daspect([1 1 1]);
scatter3(N,R,L)
set(gca, 'Box','off','FontName','Times New Roman','FontSize',12);
xlabel('Number of turns'), ylabel('Radius / m'), zlabel('Inductance / H')
figure
plot3(N,R,L,'b','linewidth',2)
set(gca,'Box','off','FontName','Times New Roman','FontSize',12);
xlabel('Number of turns'), ylabel('Radius / m'), zlabel('Inductance / H')

```

APPENDIX G

MAGNETIC SPECIFICATIONS OF S1 AND S2

Fill factor of magnetic winding: $FF = \frac{A_{magnetic}}{A_{total}}$, Effective area of magnetic

winding: $A_{eff} = FF \cdot A_{total}$, Inductance of a solenoid: $L = \mu_0 \mu_r \frac{N^2 A}{l}$.

```

mu_0 = 4*pi*10^-7; % permeability of free space
mu_r= 6000;      % relative permeability of iron
mu=mu_0*mu_r;   % permeability of core
%%%%%%%%%%%% Specifications for S1 %%%%%%%%%%%%%
l = 2*10^-2;     % length of S1
N = 160;        % number of turn of S1
d_c = 1*10^-2;  % diameter of core
d_s=2.7*10^-2;  % diameter of core plus solenoid
A_c = pi*(d_c/2)^2; % area of cross-section of core
A_total = pi*(d_s/2)^2; % total area of cross-section of magnet
A_magnetic = A_total-A_c; % area occupied by wire
FF=A_magnetic/A_total; % fill factor
A_effective = FF*A_total % effective cross-sectional of magnetic winding
%.....
L=mu*(N^2*A_total/l); % Inductance of S1
%%%%%%%%%%%% Specifications for S1 %%%%%%%%%%%%%
%.....

l2 = 3.5*10^-2;
N2 = 60;
d_c2 = 1*10^-2;
    
```

```
d_s2=2.7*10^-2;
A_c2 = pi*(d_c2/2)^2;
A_total2 = pi*(d_s2/2)^2;
A_magnetic2 = A_total2-A_c2;
FF2=A_magnetic2/A_total2;
A_effective2 = FF2*A_total2;
%.....
L2=mu*(N2^2*A_total2/l2); %Inductance of S2
%%%%%%%%%%%%%%
% NB: all the parameters define for S1 apply to S2.
% For instance, Inductance of S1 is (L)
% and Inductance of S2 is (L2)
```

APPENDIX H

EXPERIMENT 3

Experimental analysis to validate the functionality and conformance of using the electromagnet prototype.

The apparatus includes a voltage source, solenoids (S1 and S2), weights W1 and W2, and connecting wires. The solenoids (as shown in figure H1) were connected to a varying D.C. voltage source and were made to attract some weights (W1 and W2) at varying distances (d) from the electromagnet. The voltage supplied in the magnetic circuit was increased by 2 V from 2 V to 12 V. The distance from where weights W1 and W2 were attracted was determined for each voltage supplied. The results were tabulated and analysed in MATLAB.

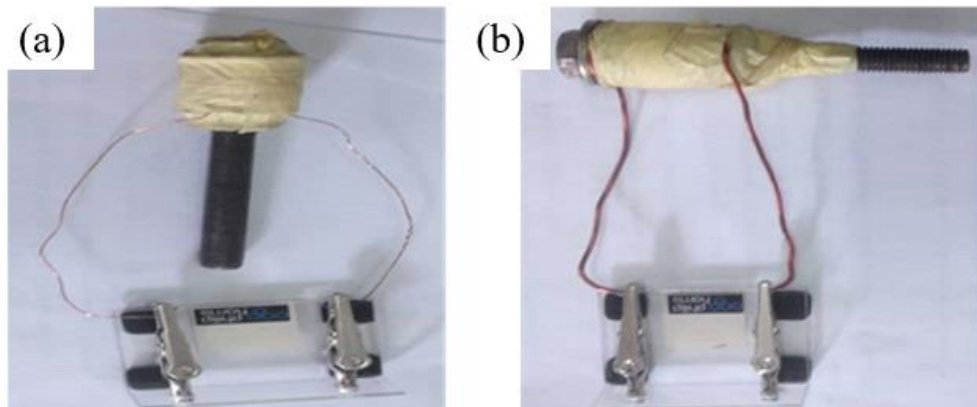


Figure H1: Pictures of the constructed solenoids used for the analysis of the MMF and the attraction distance. (a) Solenoid S₁; (b) Solenoid S₂

Table H1: Masses of the metals used for Experiment 3

Metal	Average Mass / g
M1	87.00
M2	81.00

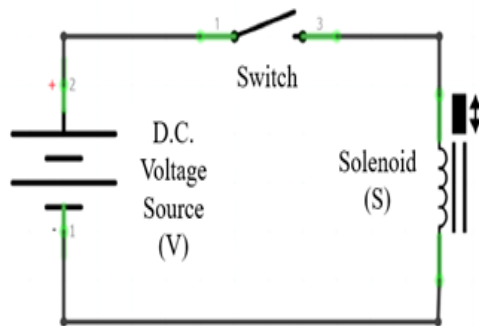
Source: Researcher, 2024



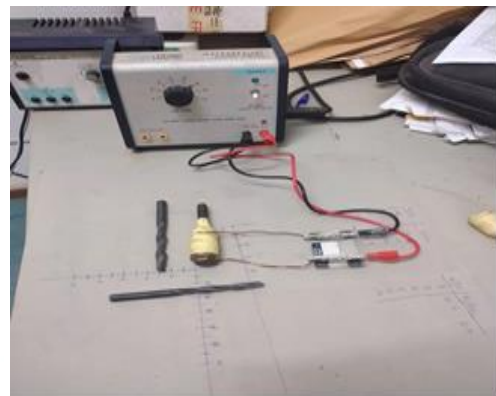
Figure H2: Pictures of the masses being measured

Diagram of Experimental setup

The experiment was set up following the magnetic circuit design in Figure H3 (a) below while the experimental setup is in Figure H3 (b).



(a)



(b)

Figure H3: Experimental setup to determine the relation between M.M.F and distance of the magnetic attraction of the electromagnets S1 and S2.

(a) Magnetic circuit diagram; (b) Diagram of experimental setup

```

% THIS PROGRAM ANALYSES THE DISTANCE OF ATTRACTION OF
% SOME OBJECTIVE WITH GIVEN MAGNETOMOTIVE FORCES
% Magnetomotivs forc: MMF in ampere-turns (A-T)
% Number of turns of coil: N, Current: I in ampers (A)
% Voltage supplied: V in volts (V), Resistance: R in ohms
% M.M.F = N.I,
% PROGEAM CODES
%.....
R1 = 2.5; R2 = 2.0; % radius of: S1(R1), S2(N2) in cm
N1 = 160; N2 = 60; % number of turns of: S1(N1) and S2(N2)
V1 = 2.0:2.0:12.0; V2 = 2.0:2.0:6.0; % voltage for: S1(v1), S2(V2)
MMF1 = N1*(V1/R1); MMF2 = N2*(V2/R2); % MMF for S1 and S2
%.....
%..... For M1 (81 g) .....%
d11 = [1.75, 2.25, 3.25, 3.25, 3.25, 3.75]; d21 = [2.00, 3.50, 4.50];
figure;
plot(MMF1, d11, '-r', MMF2, d21, '-b', 'LineWidth', 2);
set(gca, 'Box','off','FontName','Times New Roman','FontSize',12);
legend('S1-81 g', 'S2- 81 g');
xlabel('MMF / A-T'); ylabel('Distance of attraction (d) /cm');
%..... For M2 = 87 g .....%
d12 = [0.50, 1.00, 2.00, 2.00, 3.00, 3.50]; d22 = [1.50, 2.50, 3.50];
figure;
plot(MMF1, d12, '-r', MMF2, d22, '-b', 'LineWidth', 2);
set(gca, 'Box','off','FontName','Times New Roman','FontSize',12);

```

```
legend('S1-87 g', 'S2-87 g');  
xlabel('MMF / A-T'); ylabel('Distance of attraction (d) /cm');  
%..... Combined m and M .....%  
figure;  
plot(MMF1, d11, '-r', MMF2, d21, '-b',MMF1, d12, '-g', MMF2, d22, '-k',  
'LineWidth', 2);  
legend('S1-81 g', 'S2-81 g','S1-87 g', 'S2-87 g');  
set(gca, 'Box','off','FontName','Times New Roman','FontSize',12);  
xlabel('MMF / A-T'); ylabel('Distance of attraction (d) /cm');
```

APPENDIX I**MDet CODE**

```
// Define the pin connections

const int metalDetectorPin = A0; // Analog pin for metal detector

const int relayPin = 9; // Digital pin for electromagnet control

// Define threshold for metal detection

const int metalThreshold = 500; // This value should be adjusted based on the
sensor sensitivity

void setup() {

  Serial.begin(9600); // Initialize serial communication

  pinMode(relayPin, OUTPUT); // Set electromagnet pin as output
}

void loop() {

  // Read analog value from metal detector sensor

  int metalValue = analogRead(metalDetectorPin);

  Serial.println(metalValue); // Print the raw sensor value

  // Check if metal is detected

  if (metalValue > metalThreshold) {

    digitalWrite(relayPin, HIGH); // if yes, actuate the electromagnet

    Serial.println("Metal Detected! Relay Activated.");

  } else {

    digitalWrite(relayPin, LOW); // If no turn off the electromagnet

  }

  delay(30000); // The delay time can be adjusted as needed
}
```

APPENDIX J

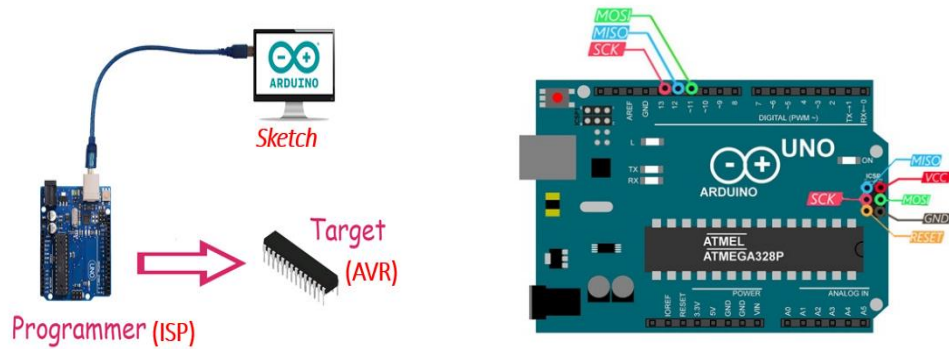
PROCEDURE FOR BURNING THE BOOTLOADER ON THE
MICROCONTROLLER

Figure J1: Arduino board as ISP and pinout (Shojaei, n.d.)

Components

Atmel ATmega238P microcontroller (1), 16 MHz clock crystal (1), 7805 Voltage regulators (1), 10 μ F capacitor (1), 22 pF capacitor (2), 10 k Ω resistor (1), Breadboard (1), AWG wires (16).

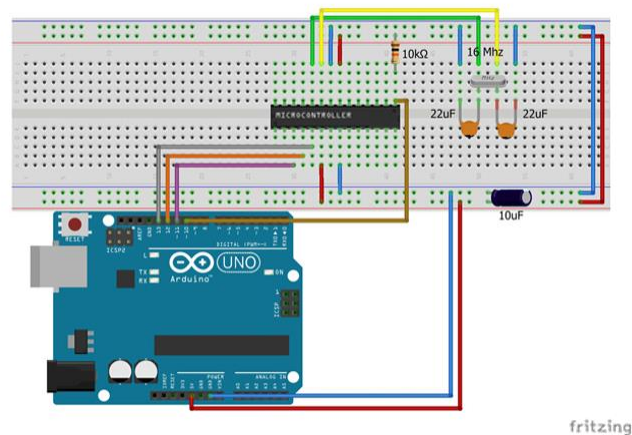


Figure J2: Simulated figure for the DIY Arduino

AVR programmer: Arduino as In-System Programming (ISP) was used as the AVR programmer to write the bootloader code onto the microcontroller chip.

The set-up connection: The AVR programmer (Arduino UNO) was connected to the appropriate pins following the table below:

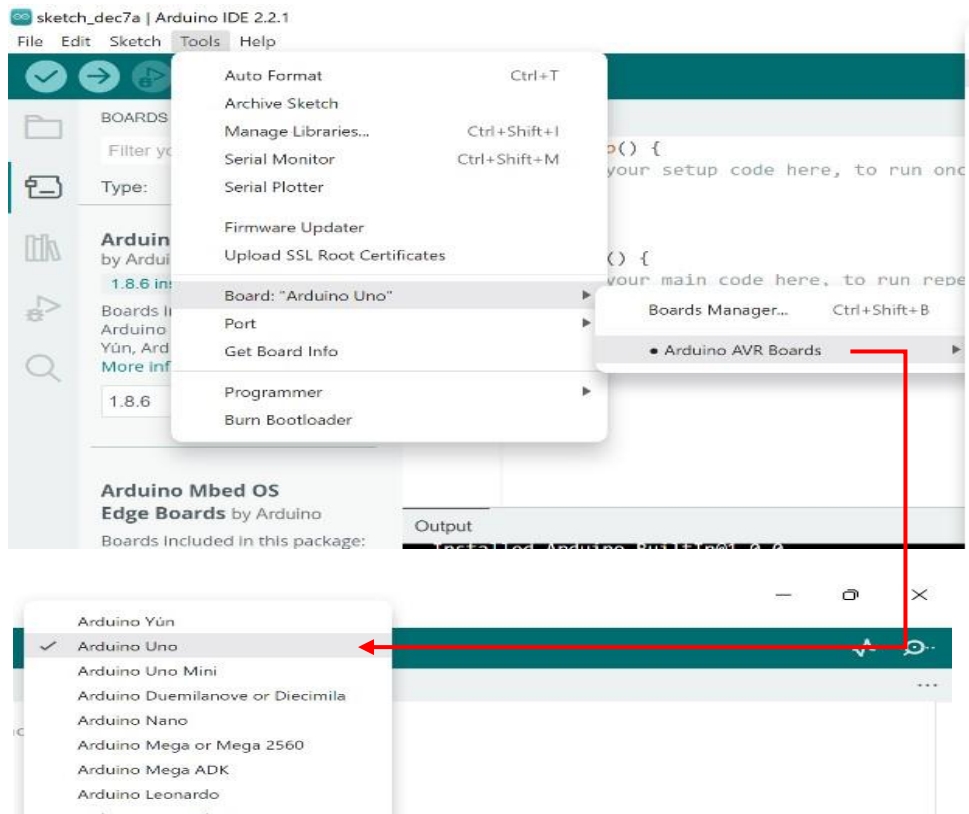
Table J1: Arduino as ISP pin – Atmega328P Pin Mapping

Arduino as ISP PIN	Atmega328P PIN	Description
5 V	2	5 V
GND	6	GND
D10	5 (1)	Reset
D11	4 (17)	MOSI
D12	1 (18)	MISO
D13	3 (19)	SCK

Source: Researcher, 2024

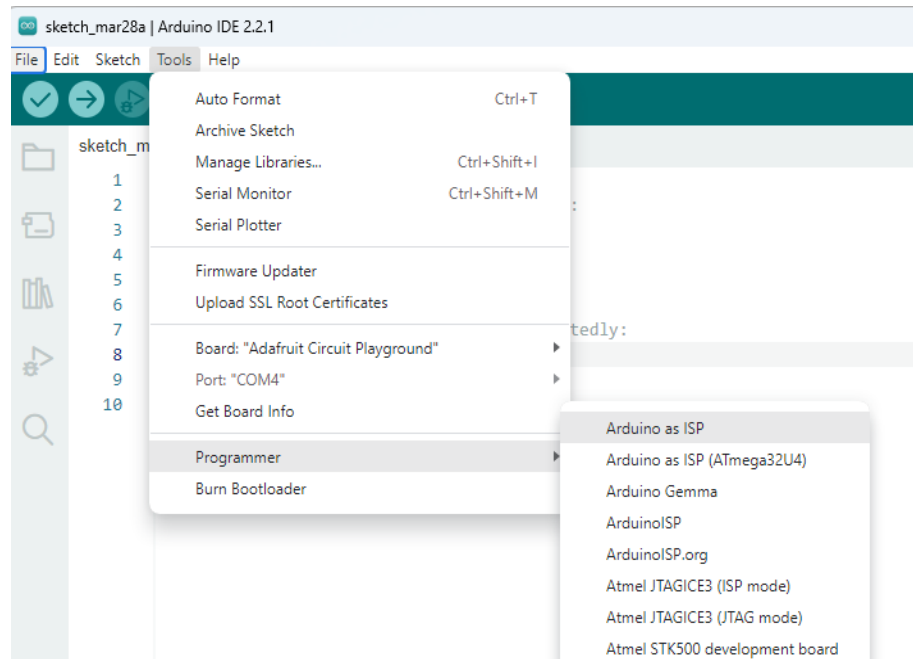
1. The Arduino IDE on the computer was opened
2. In selecting the Board and processor stepped below were followed
 “Tools” > “Boards” > “Arduino Uno” with the appropriate COM port.

The figure below outlines the various processes that appeared on the computer.

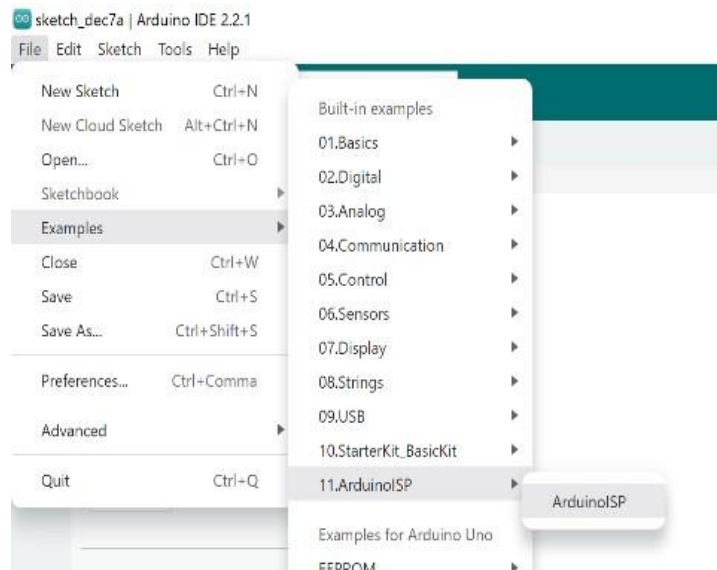


3. The programmer was selected following the following steps:
 “Tools” > “Board” > “Arduino AVR Boards” > “Arduino Uno”, the
 “Tool” > Programmer > Arduino as ISP

The figure below shows the various processes that appeared on the computer screen.



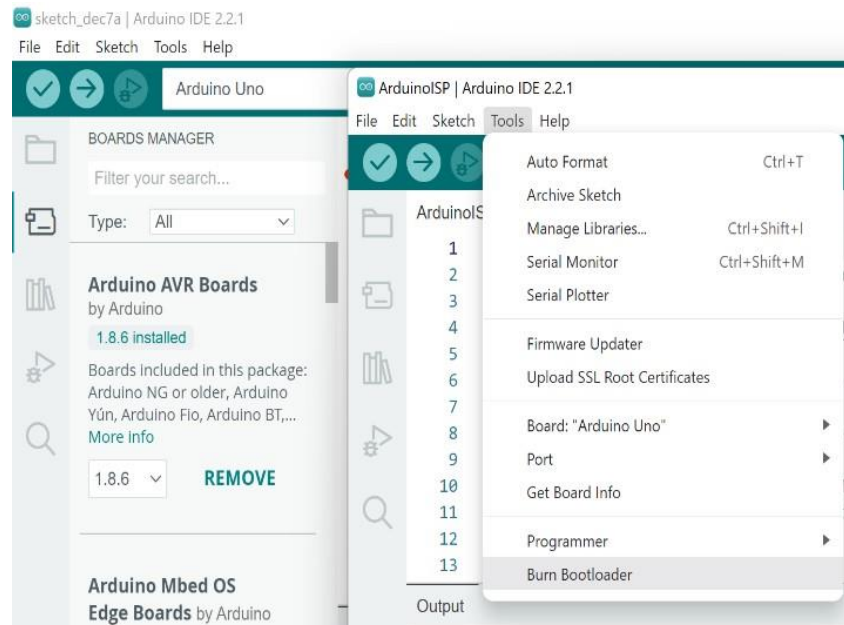
4. The bootloader file was chosen as follows: “File” > “Examples” > “ArduinoISP”. This opened the ArduinoISP sketch.



The sketch was uploaded onto the Arduino Uno board to turn it into the AVR programmer.

5. The Bootloader was then burnt following these steps

“Tools” > Burn Bootloader



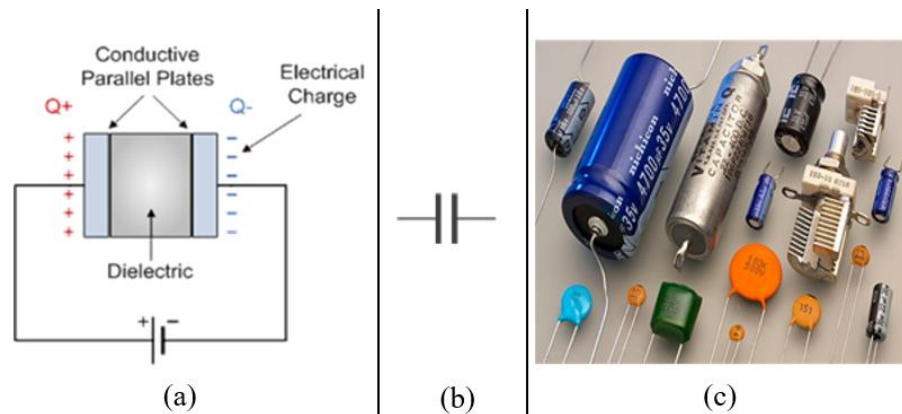
The success of the burning process was verified in two ways: (1) the microcontroller was fixed on the Arduino Uno board and the reset button pressed. The blinks of the LEDs confirmed the success. (2) A simple LED blink sketch was uploaded onto the microcontroller which was able to blink an LED. With this done, any code can be uploaded onto the Atmega328P microcontroller and run straight from the Arduino IDE for standalone applications.

APPENDIX K

DESCRIPTION OF COMPONENTS

Capacitors

A capacitor is a two terminal electronic component that builds up electric charges on two conductive plates separated by a dielectric material, allowing the capacitor to store charges of opposite polarity. Capacitors act as a load and store electrical charge on their plates when they are connected to a voltage source (VE). However, they act as a source to supply voltage (VC) when the external voltage source is disconnected. The figure below shows a capacitor in a circuit (a), the circuit symbol of a capacitor (Capacitance, n.d.) (b), and some practical capacitors used in electronic devices (c) (Siddhardha, 2024).

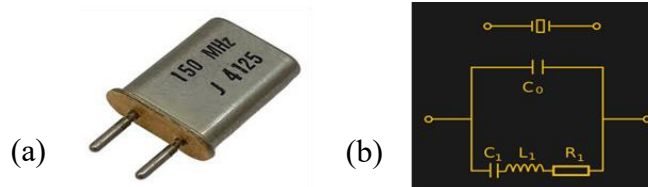


Crystal oscillator

A crystal oscillator is an electronic oscillator circuit that uses the mechanical resonance of a vibrating crystal of piezoelectric material to create a repetitive electrical signal (Meaney, n.d.) with a very precise frequency. It typically consists of three main components: a crystal resonator, an amplifier, and a feedback circuit which work together to create a stable and consistent output signal (Xu, Blaauw, & Sylvester, 2021). The performance of a crystal oscillator

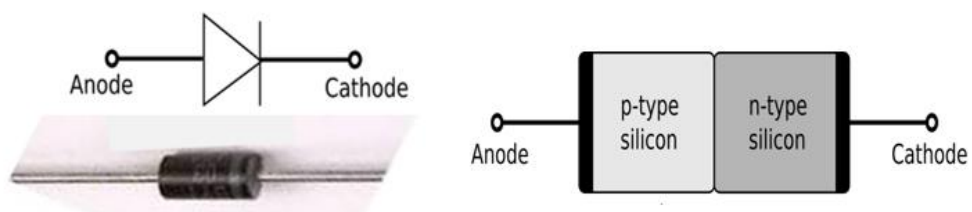
is influenced by a variety of factors, including external factors such as temperature and humidity, and the quality and precision of its components.

The quartz crystal oscillators are by far the most common time and frequency standard (Plonus, 2020). Its electrical equivalent model is that of a series circuit in parallel with a capacitor, giving it some of the properties of both a parallel and a series circuit (List, 2017). The figure below shows a practical crystal oscillator (a) and the equivalent circuit of the quartz oscillator (b) (List, 2017).



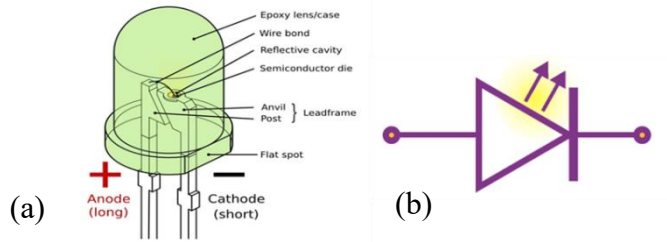
Diodes

Diodes are electrical components that have the rectifying attribute of being able to pass electricity in one direction with greater ease while halting it in the other (Kuphaldt, 2006). They are referred to as PN junction diodes with two terminals: a positive terminal (cathode) and a negative terminal (anode). Most diodes operate only in the forward bias mode; that is, the cathode is connected to the positive terminal and the anode is connected to the negative terminal of the external voltage source, making them suitable for use as rectifiers and switches. In the figure below is a diagram of a diode with pin configuration (Ravi Teja *et al.*, 2018; Department of EECS [DEECS] 2007).



Light emitting diode (LED) is a class of diodes that gives off light as current flows through it, that is when it is forward biased. The figure below shows the part of an LED (a) and the circuit symbol used to denote an LED (Koteswaramma, Navya, Singh, Rajeshwari, & Mounika, 2022)

(b).



Arduino microcontrollers

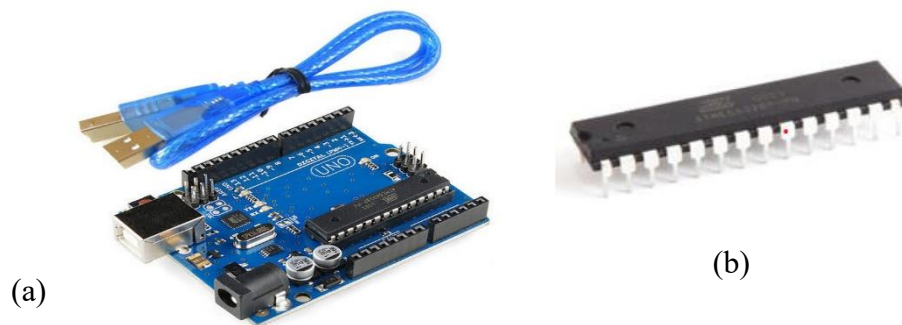
Arduino is a popular open-source hardware cross-platform (Sujadi, *et al.*, 2018) based on easy-to-use software (Corso & Elettrica, 2012). It uses microcontroller units (MCUs) from various manufacturers like Atmel, Microchip, etc. Its support for embedded systems and embedded computing enables the automation of devices, saving energy and other resources (Wang, Z., Lim, E. G., Wang, W., Leach, M., & Man, K. L. (2015). The voltage range required to operate most Arduino boards ranges from 3.7 V to 5 V, with the Arduino UNO Rev3 operating at 5 V but being driven by a DC voltage between 7 V and 12 V. It supports 14 digital I/O PICs, with the output pins typically outputting about 20 mA, 6 analogue input pins, and 6 Pulse Wave Modulation (PWM) pins

The Arduino UNO Rev3 microcontroller uses the ATmega328P microcontroller. The Atmel ATmega line of microcontrollers uses internal RC oscillators or external clock generators, such as quartz crystal oscillators or ceramic resonators, depending on the frequency and precision. They have input

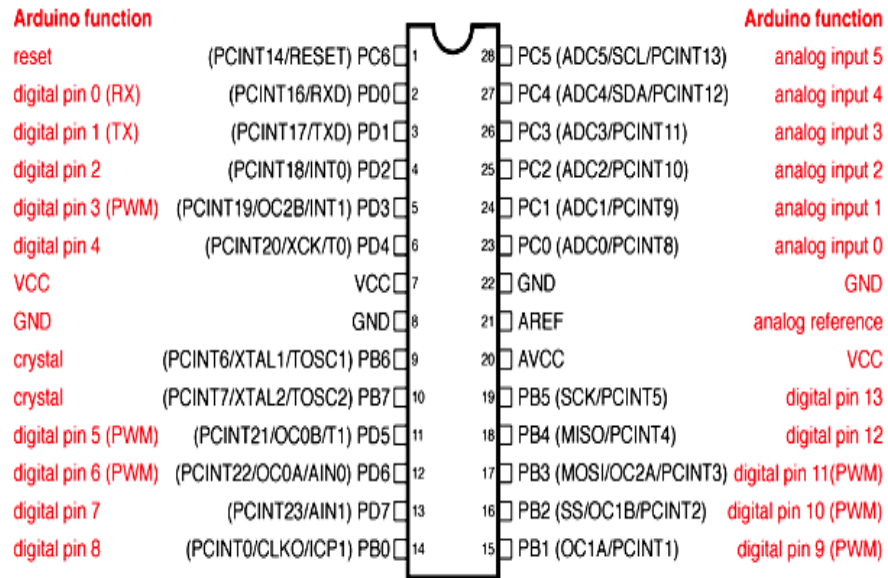
and output (I/O) pins for interfacing transducers, designed with Analog to Digital Convertors (ADC) and Digital to Analog Convertors (ADC) (Frempong, 2016) to suit both analog and digital transducers.

The ATmega is a low-power Complementary Metal-Oxide-Semiconductor (CMOS) 8-bit microcontroller based on the AVR RISC Processor (AVR) enhanced Reduced Instruction Set Computing (RISC) architecture (Pan, & Zhu, 2017; Sudhan, R. H., Kumar, M. G., Prakash, A. U., Devi, S. A. R., & Sathiya, P, 2015). It operates at a clock speed of 8/16 MHz and provides 32K bytes of in-system programmable flash with read-while-write capabilities, 1K bytes EEPROM, 2K bytes SRAM, 23 general-purpose I/O lines, 32 general-purpose working registers Dada, E. G., Hamidu, A. A., & Stephe, J. 2019), three flexible Timer/Counters with compare modes, internal and external interrupts, a serial programmable Universal Synchronous/Asynchronous Receiver/Transmitter (USART), a byte-oriented 2-wire serial interface, an SPI serial port, a 6-channel 10-bit ADC (8 channels in TQFP and QFN/MLF packages), a programmable watchdog timer with internal oscillator, and five software-selectable power-saving modes.

The figure below shows the Arduino Uno rev3 with the USB cable (a) and Atmel ATmega328P microcontroller IC (b) (Sudhan *et al.*, 2015).



The Pin diagram of the ATmega microcontroller is shown below (Zait, 2018).



Digital Pins 11, 12 & 13 are used by the ICSP header for MOSI, MISO, SCK connections (Atmega168 pins 17, 18 & 19). Avoid low-impedance loads on these pins when using the ICSP header.

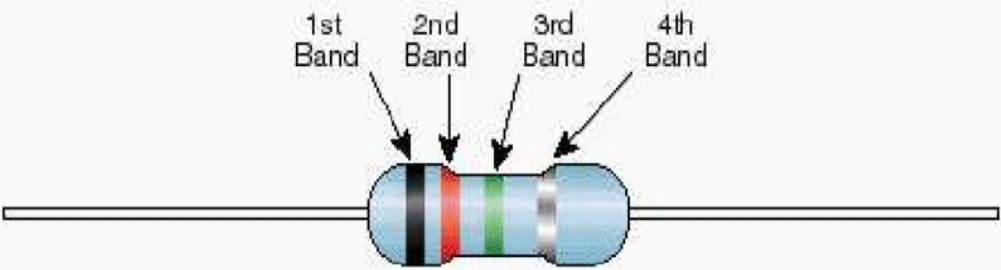
Resistors

A resistor is a passive electrical component that obstructs the flow of electricity (Adelakun & Omolola, 2023). The unit of measurement for resistance is ohms (Ω). The figure below shows some type of practical resistors used in mechatronics (Biomedical Engineering Department, 2023).



The voltage across the terminal ends determines the current in a proportionate manner, as stated in ohms law ($V = IR$).

A resistor with a known resistance is termed as standard resistor. The commonest standard resistors used in electronics are colour code resistors (CCRs). CCRs have multiple-coloured bands surrounding the body that give information about the resistance value and tolerance. Resistors limit the flow of current through a loop. Resistance of colour code resistors can be determined by measuring with an RLC meter or multimeter and by calculation using the colour code guide in the figure below (Sommers, 2016).



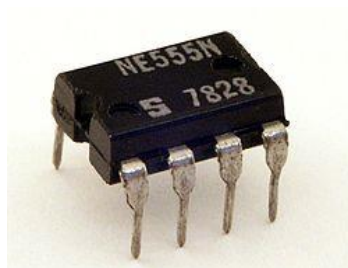
Color	1st Band (1st figure)	2nd Band (2nd figure)	3rd Band (multiplier)	4th Band (tolerance)
Black	0	0	10^0	
Brown	1	1	10^1	
Red	2	2	10^2	$\pm 2\%$
Orange	3	3	10^3	
Yellow	4	4	10^4	
Green	5	5	10^5	
Blue	6	6	10^6	
Violet	7	7	10^7	
Gray	8	8	10^8	
White	9	9	10^9	
Gold			10^{-1}	$\pm 5\%$
Silver			10^{-2}	$\pm 10\%$

The 555 timer IC

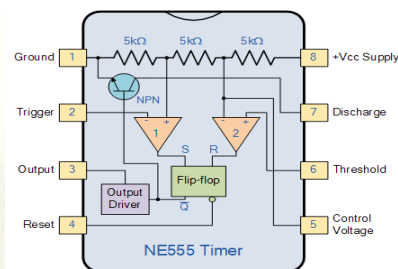
The 555-timer IC is a highly accurate timing device that generates two comparator reference voltages using three internal $5\text{ k}\Omega$ resistors. It can be used as a relaxation oscillator to produce stable waveforms or as a simple timer to generate pulses. The 8-pin chip can operate as a monostable, bistable, or astable multivibrator, making it suitable for a variety of applications, including time control circuits, LED flashers, alarms, one-shot or delay timers, and pulse generators. It may be conveniently run with 200mA of power and a voltage range of 5v to 15v.

Pin 1 connects the 555 timer IC to the negative supply rail. Pin 2 sets the internal flip-flop when voltage drops below $1/3V_{CC}$. Pin 3 can supply/sink up to 200mA and is ideal for small speakers, LEDs, or motors. Pin 4 prevents unintentional output resets and is typically connected to a logic "1" level. Pin 5 controls the timing of the 555 and allows for independent output signal width modification. A 10nF capacitor reduces noise. Pin 6 resets the flip-flop when voltage goes above $2/3V_{CC}$. The discharge pin discharges the timing capacitor to the ground. Pin 8's voltage range is 4.5 to 15 volts for TTL 555 timers.

The 555 timer IC (a) and the Block diagram of the 555 timer IC (b) as adopted from (AlMadhoun A. S. & Al-Sdoudy, n.d.) are shown in the figure below.



(a)

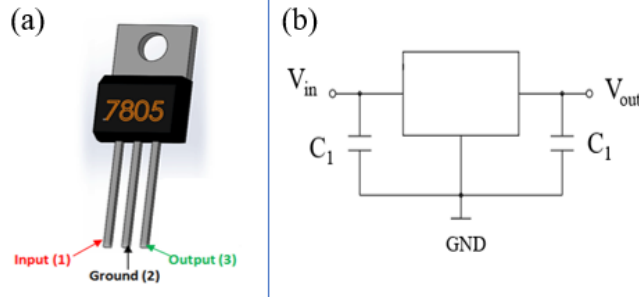


(b)

The voltage regulator IC

A voltage regulator IC is an electronic component used to keep the output voltage steady (Frempong, 2016). It has an internal short-circuit protection which limits the maximum current the circuit can handle. The regulator also has output transistor safe-area compensation that reduces the output short-circuit current as the voltage across the pass transistor increases. Additionally, thermal overload protection is included to prevent the circuit from experiencing an excessive power overload condition, which could be dangerous.

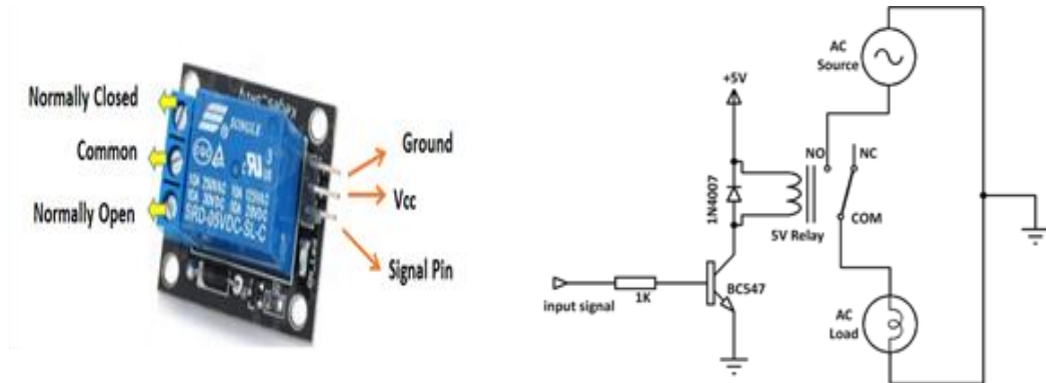
The LM and the TO series are a complete 5V regulators manufactured on a single silicon chip to ensure local regulation on digital logic cards without any distribution issues associated with single-point regulation. They are three-terminal regulators with pin configurations and function presented in table 2.1 that can deliver over 1.5 A current. In a circuit; tow capacitors, called bypass capacitors, are connected with the voltage regular to short AC noise from the voltage signal and allow only DC voltage into the regulator. The bypass capacitors are particularly necessary if the voltage regulator is situated more than 25cm (10 inches) from the power supply. A typical voltage regulator pin configuration (a) and the circuit connection diagram of voltage regulators (b) as adopted from (Mubeen, 2023; Dada *et al.*, 2019) are shown in the figure below.



Relays

Relays are electrical switches (Adelakun & Omolola, 2023) that control one electrical circuit by opening and closing contacts in another circuit. Solid-state relays (SSRs) and electromechanical (EMR) relays are the two types of relays.

. A labelled diagram of a relay (a) and relay model circuit diagram (b) as adopted from Nandi, P. K., Ema, R. R., Islam, T., & Jahan, S. (2020) are shown in the figure below:

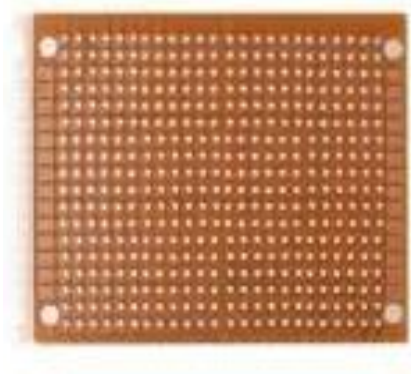
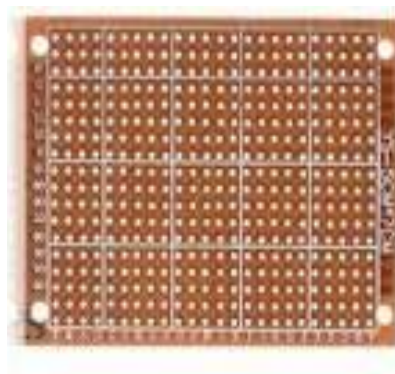


To open or close contact, EMR uses magnetic forces, but SSRs do away with contacts and all electronic switching. The decision between these options is influenced by application life expectancy, budget, and electrical requirements. SSRs are becoming more and more common, but electromechanical relays are still commonly employed for heavy equipment duties. Relays can also be categorised into single pole single throw (SPST) and double pole double throw (DPDT). SPSTs relays control one secondary circuit while DPDTs control two

"secondary" circuits – in this case a motor, for instance, can rotate in a clockwise then counterclockwise direction and vice versa (Gurevich, 2018).

The general-purpose PCB

The term "general-purpose PCB (Printed Circuit Board)" describes a kind of circuit board that may hold different electronic parts and circuits for different uses. Soldering components onto these PCBs to construct unique electrical circuits is made possible by their standard layout of copper traces, pads, and holes. They can support surface mount components, which are soldered directly onto pads on the PCB's surface, or through-hole components, where leads go through holes in the PCB and are connected to pads on the other side. The picture below shows a general-purpose PCB (Dada, *et al.*, 2019; Koteswaramma *et al.*, 2022).



APPENDIX L

WIRE SPECIFICATIONS FOR ELECTROMAGNETIC
TECHNOLOGY

American Wire Gauge (AWG) Sizes and Properties

AWG	Diameter /mm	Resistance / Ωkm^{-1}	Max Current /A	Max Frequency for 100% skin depth /kHz
23	0.57404	66.7808	0.729	53
24	0.51054	84.1976	0.577	68
25	0.45466	106.1736	0.457	85
26	0.40386	133.8564	0.31	107
27	0.36068	168.8216	0.288	130
28	0.32004	212.8720	0.226	170

Source: Errede, 2015

APPENDIX M

EXPENDITURE ON THE COMPONENTS

Item	Unit Price (GHC)	Quantity	Cost (GHC)
Atmel Atmega328P	60.00	2	120.00
28-Pin DIP IC Socket	5.00	2	10.00
Resistors pack	50.00	1	50.00
Ceramic Capacitors	1.00	10	10.00
Electrolytic Capacitor	1.00	10	10.00
Single channel Relay	20.00	2	40.00
5 V Voltage regulator	10.00	2	20.00
555 timer IC	10	4	40.00
8-Pin DIP IC Socket	3.00	4	12.00
Potentiometers	10.00	2	20.00
LED	0.20	10	2.00
16MHZ Crystal	4.00	2	8.00
1N4001 Silicon Diode	1.00	5	5.00
Push Button with a Cap	3.00	2	6.00
Piezo Buzzer	4	2	8.00
Perforated Circuit Board	20	2	40.00
Jumper wires	20.00	3	60.00
24-gauge Copper wire	200.00	1	200.00
27-gauge Copper wire	200.00	1	200.00
PCB Mount Screw Terminals	70	1 (20 PCS)	70.00
Total			1400.00